Petrogenetic links between rare metal-bearing pegmatites and TTG gneisses in the West African Craton: The Mangodara district of SW Burkina Faso

Wilédio Marc-Emile Bonzi, Olivier Vanderhaeghe, Marieke van Lichtervelde, Urbain Wenmenga, Anne-Sylvie André-Mayer, Stefano Salvi, Marc Poujol

Petrogenetic links between rare metal-bearing pegmatites and TTG gneisses in the West African Craton: the Mangodara district of SW Burkina Faso

Authors

*Wilédio Marc-Emile Bonzi[1,2], Olivier Vanderhaeghe[2], Marieke Van Lichtervelde[2], Urbain Wenmenga[1], Anne-Sylvie André-Mayer[3], Stefano Salvi[2], and Marc Poujol[4]

[1] Département des Sciences de la Terre, Université Joseph Ki-Zerbo, 03 BP 7021 Ouagadougou, Burkina Faso

[2] Laboratoire Géosciences Environnement Toulouse, CNRS-IRD, Université Toulouse 3 Paul Sabatier, 14 Avenue Edouard-Belin, 31400 Toulouse, France

[3] Laboratoire GeoRessources, Université de Lorraine, CNRS, F-54000, Nancy, France

[4] Geosciences Rennes - UMR 6118, Université de Rennes, CNRS, F-35000, Rennes, France

*Corresponding author: bonzime@gmail.com

Abstract

We describe the geological context of rare metal-bearing pegmatites from the Mangodara district (South-West Burkina Faso, Paleoproterozoic West African Craton) and discuss their petrogenesis and links with the host rocks. The Mangodara district exposes a gneiss-granitoid complex structured in a regional-scale dome, mantled by granodioritic gneiss enclosing rafts of amphibolite, micaschist and paragneiss, and cored by tonalitic to trondhjemitic gneisses. These gneisses enclose granitoid plutons, and four populations of rare metal-bearing pegmatites: titanite-allanite-, apatite-zircon-, garnet-columbite (Li, Nb) and garnet-REE (Ti, Y, HREE)-bearing varieties.

Rafts of migmatitic amphibolite, micaschist and paragneiss are chemically equivalent to nearby Birimian greenstone belts. An origin of the gneiss-granitoid complex by partial melting is suggested by diffuse contacts of rafts with the gneisses as well as the presence of garnet-bearing or hornblende-bearing leucosome in paragneiss and in amphibolites, respectively. Textural continuity between pegmatites and granitic veins concordant to the foliation of the gneisses point to syntectonic segregation of the pegmatite-forming magmas.

The compositions of gneisses and plutonic rocks spread between a Na-rich pole and a K-rich pole. Granodioritic gneiss, hornblende-biotite granodiorite and potassic biotite granitoids define a K-rich series attributed to relatively low-pressure high-degree partial melting of dominantly paragneiss, which accounts for low to absent LILE and HFSE fractionation compared to the paragneiss. Tonalitic-trondhjemitic gneiss, a trondhjemite and a peraluminous two-mica tonalite belong to a Na-rich series characterized by low K content and strong depletion in REE and HFSE, which might reflect plagioclase clustering after partial melting at a relatively high pressure of amphibolite, and fractionation of HFSE-REE-bearing minerals.

U-Pb dating of zircon from a titanite-allanite-bearing pegmatite at 2094.3 ± 8.8 Ma and of apatite from tonalitic-trondhjemitic gneiss, apatite-zircon-bearing pegmatite and granodioritic gneiss at 2094 ± 21 Ma, 2055 ± 20 Ma, and 2041 ± 33 Ma respectively, confirm that partial melting, melt segregation and crystallization-cooling occurred during the Eburnean orogeny.

Based on these data, we propose that (i) titanite-allanite- and apatite-zircon-bearing pegmatites result from syntectonic segregation of residual melt during crystallization of the tonalitic-trondhjemitic gneiss, (ii) garnet-columbite-bearing pegmatites originate from syntectonic melt segregation from the migmatitic paragneiss, and (iii) garnet-REE-bearing pegmatites derive from segregation of a residual melt within the granodioritic gneiss.

Keywords: Rare metal-bearing pegmatite, TTG gneiss, Eburnean orogeny, West Africa Craton, partial melting, melt segregation.

1. Introduction

This paper presents the geological context of the rare metal-bearing pegmatites exposed in the Mangodara district (South west Burkina Faso, West African Craton, Fig. 1), in the Baoulé-Mossi domain of the Eburnean orogenic belt (Baratoux et al., 2011 and references therein). Its goal is to discuss the petrogenesis of these pegmatites and their potential links with their host rocks. The formation of rare metal pegmatites requires a high degree of differentiation, which has classically been related either to segregation of a silicate melt issued from low-degrees of partial melting of an enriched source (Müller et al., 2017; Roda-Robles et al., 2007; Shaw et al., 2016) or from extreme fractional crystallization of a fertile magma (Černý, 1991a, 1991b; Černý and Ercit, 2005; London, 2008; Martin and De Vito, 2005). In the Paleoproterozoic portion of the West African Craton (Fig. 1) known for its huge gold reserves (Masurel et al., 2021), rare metal-bearing pegmatites mineralized in spodumene and columbite-tantalite (Ta > Nb) are reported at Akim-Oda, Egyaa and Winneba in Ghana (Adams, 2013; Anum et al., 2015; Chalokwu et al., 1997; Nude et al., 2011), at Issia in Ivory Coast (Allou, 2005) and Saraya in eastern Senegal (Goujou et al., 2010; Ndiaye et al., 1997). These pegmatites form dykes intruding peraluminous granitic plutons and metasedimentary units, and are interpreted to derive from the differentiation of these sedimentary-derived granitic bodies. The Mangodara district (Fig. 2) potentially represents a deeper section of the Birimian crust, with pegmatites hosted in a gneiss-granitoid complex that includes large rafts of migmatitic amphibolites and paragneiss, all structured into a regional-scale dome. In such context, deciphering the relationships of the pegmatites with their gneissic host rocks is essential in order to assess their petrogenesis. Early investigators considered these gneiss-granitoid complexes to represent the Archean basement of Paleoproterozoic Birimian greenstones, essentially based on their positioning at the lowest exposed structural level (Arnould, 1961; Ducellier, 1963; Hottin and Ouedraogo, 1975; Tagini, 1971). However, U-Pb geochronology on zircon from granitoid and gneisses from these complexes did not yield any Archean age, but ranges from 2300 to 2050 Ma (Anum et al., 2015; Castaing et al., 2003; De Kock et al., 2011; Doumbia et al., 1998; Gasquet et al., 2003; Grenholm et al., 2019a; Hirdes et al., 1996; Ilboudo et al., 2021; Parra-Avila et al., 2017; Petersson et al., 2016; Sakyi et al., 2014; Soumaila et al., 2008; Tapsoba et al., 2013; Tshibubudze et al., 2015, 2013; Wane et al., 2018). These ages span the entire Birimian cycle, from the Eoeburnean or Pre-Eburnean phase (2260–2150 Ma) to the Eburnean orogeny (2150–2050 Ma), which is constrained by U-Pb in zircon from Birimian metavolcanites and plutonic rocks intrusive in greenstone belts across the Baoule-Mossi domain (Grenholm et al., 2019a; Lambert-Smith et al., 2016; Parra-Avila et al., 2017 and references therein). The absence of Archean ages, together with the presence of Early Proterozoic ages up to 2300 Ma, served to invoke a pre-Birimian crustal growth event, referred to as Burkinian or Dabakalian, forming the Birimian volcanic and sedimentary basement, or at least the basement of its upper series (Lemoine, 1988; Lemoine et al., 1990; Vidal et al., 1996).

In this context, gneisses and granitoids exposed in the Eburnean orogenic belt have been interpreted as syntectonic to late tectonic plutons, mainly based on their pervasive ductile fabric consistent with structures observed in the surrounding greenstones (Gasquet et al., 2003; Hirdes et al., 1996; Vidal et al., 2009). Moreover, gneiss-granitoids and Birimian greenstones share a similar Paleoproterozoic juvenile isotopic signature, which was attributed to a common mantle source for these magmas emplaced at different structural levels (Abouchami et al., 1990; Boher et al., 1992; Doumbia et al., 1998; Gasquet et al., 2003; Pawlig et al., 2006; Sakyi et al., 2020; Tapsoba et al., 2013). However, these structural features and the similarity in isotopic are equally consistent with an origin of gneiss and granitoids by partial melting of the Birimian series (Doumbia et al., 1998).

In order to contribute to this debate, in this paper, we present new field observations, petrological-microstructural and geochemical data from gneisses, plutonic rocks and swarms of rare metal-bearing pegmatites of the Mangodara district. Based on these data, which highlight the significance of metamorphic and magmatic units that compose the Mangodara district, we propose a petrogenetic model relating the rare metal-bearing pegmatites to the gneiss-granitoids.

2. Methodology

Field work was conducted throughout the Mangodara district to document the mineralogy, texture, and structure of each lithological facies and their mutual structural relationships. Regional directions of lithofabrics were inferred from field measurement, from distribution and morphology of outcrops in aerial photography (Google Earth), and from lineaments and other structures detected from LANDSAT-8 and Sentinel-2 imagery. Shear zones were remotely identified by interpretation of magnetic lineaments in aeromagnetic data (acquired during the SYSMIN project System for Mineral production, 1998–1999, see Metelka et al., 2011), using the methodology proposed by Chardon et al., (2020).

Pegmatites and surrounding rocks of the Mangodara district were sampled for thin section preparation and for whole-rock analysis. The latter were performed by the Service d'Analyses des Roches et des Minéraux (SARM, Centre de Recherches Pétrographiques et Géochimiques de Nancy, France) using inductively coupled plasma optical emission spectrometry (ICP-OES) with a Thermo Fischer iCap6500 for major elements and inductively coupled plasma mass spectrometry (ICP-MS) with a Thermo iCapQ for trace elements, and in Central Analytical facilities of University of Stellenbosch (South Africa) using XRF spectrometry with a PANalytical Axios Wavelength Dispersive spectrometer for major elements and using laser ablation inductively coupled plasma mass spectrometry (LA-ICP-MS) with a Agilent 7700 for trace elements. Concentrations in major elements of minerals were measured using a Cameca SXFive at Center Raimond Castaing (Toulouse, France). Standards were albite (Na), wollastonite (Si, Ca), Al_2O_3 (Al), sanidine (K), $MnTiO_3$ (Mn, Ti), Fe_2O_3 (Fe), topaz (F), MgO (Mg), tugtupite (Cl), Cr_2O_3. Detection limits for major element oxides were under 0.2 wt%. The structural formula of hornblende was calculated based on 23 oxygen atoms. Fe^{2+} and Fe^{3+} were estimated by charge balance, and the formula was normalized with the minimum ferric amount allowing complete site occupancy, using the method of Schumacher (1997).

Pressure-temperature pseudosections were calculated for a paragneiss and an amphibolite samples using Theriak/Domino v 11/03/2020 (de Capitani and Brown, 1987; de Capitani and Petrakakis, 2010), with the internally consistent thermodynamic dataset of Holland and Powell (1998), in its version 5.5 updated in November 2003. Bulk composition of the paragneiss and the amphibolite are estimated respectively from the whole rock composition of the samples BMS114B and BMN109. Calculations are done in the chemical system Na_2O-CaO-K_2O-FeO-MgO-Al_2O_3-SiO_2-H_2O-TiO_2-O (NCKFMASHTO) for the paragneiss, and Na_2O-CaO-FeO-MgO-Al_2O_3-SiO_2-H_2O-TiO_2-O (NCFMASHTO) for the amphibolite. Manganese content was ignored from calculation because of its low concentration in the two samples (< 0.1 mol%), but this should not significantly affect the equilibrium phase transitions. Hydrogen content is adjusted to reach a minimum of H_2O saturation at solidus at 7 kbar. A supplementary tiny content of O is added to stoichiometric O content, to permit stability of Fe^{3+}-bearing phase. The used activity-composition models are biotite, garnet, ilmenite-hematite, spinel and silicate melt (White et al., 2007), cordierite, staurolite and chlorite (Holland and Powell, 1998), white mica (muscovite, Fe-celadonite), (Coggon and Holland, 2002), clinopyroxene (Green et al., 2007), orthopyroxene (White et al., 2002), amphibole (Diener et al., 2007) and feldspars (Baldwin et al., 2005; Holland and Powell, 2003). Andalusite, kyanite, sillimanite, quartz and H_2O are treated as pure phases.

Zircon and apatite were dated by in situ laser ablation on polished thin section. Prior selection of targets and imaging of minerals were carried out by back-scattered electron imaging with a scanning electron microscope (SEM) Jeol JSM 6360LV (GET, Toulouse, France) and by cathodoluminescence imaging with the TESCAN Vega 3 (GeoRessources, Nancy, France). Laser ablation was operated using a quadripole Agilent 7700 coupled with an ESI NWR193UC excimer laser (Géosciences Rennes, Rennes, France). U-Pb ages are calculated from isotopic data with the software Isoplot/Ex v3.76 (Ludwig, 2003). Technical details of the analysis are supplied in appendix.

3. Geological context of the Mangodara district within the West African Craton

The West African Craton (WAC) consists of the Kenema-Man Archean nucleus surrounded along its northern and eastern borders by the Baoule-Mossi domain composed of Paleoproterozoic terranes of the Birimian series tectonically accreted during the multicyclic Eburnean orogeny (Baratoux et al., 2011; Block et al., 2016b, 2016a; Feybesse et al., 2006; Kouamelan, 1996; Perrouty et al., 2012; Tshibubudze and Hein, 2013; Vidal and Alric, 1994). The Baoule-Mossi domain corresponds to a succession of greenstone belts of the Birimian series juxtaposed along strike-slip shear zones to gneiss-granitoids coring large dome structures (Baratoux et al., 2011; Fabre et al., 1990; Metelka et al., 2011; Milési, 1989; Vidal et al., 2009). It is a lateral equivalent to the Transamazonian belt in the South America (Caen-Vachette, 1988; Chardon et al., 2020; Delor et al., 2003; Grenholm, 2019; Grenholm et al., 2019a; Ledru et al., 1991; Tassinari and Macambira, 1999; Vanderhaeghe et al., 1998)

The Mangodara district (SW Burkina Faso) is situated in the Sidéradougou gneiss-granitoid complex (SGGC) of the Baoule-Mossi domain, between the Banfora greenstone belt to the west, and the Hounde greenstone belt to the east delimited by the sinistral Ouango-Fitini shear zone (OFSZ) (Fig. 1). The Birimian in south-west Burkina Faso is composed of series of metamorphosed and deformed subvertical interlayered tholeiitic to calc-alkaline basalts, andesites and rhyolites, alternating with volcanic-sedimentary rocks and silicic sedimentary rocks. In this region, U-Pb dating on zircon from rocks of the Birimian series indicate an early volcanic activity from 2220 Ma to 2160 Ma (Baratoux et al., 2011; Giovenazzo et al., 2018; Hirdes et al., 1996; Hirdes and Davis, 1998; Lüdtke et al., 1998) and later emplacement/deposition of volcanic-sedimentary series from 2165 to 2080 Ma (Castaing et al., 2003; Grenholm et al., 2019b; Hirdes et al., 1996; Lüdtke et al., 1998).

Aside from volcanic rocks of the Birimian series, plutonic rocks, with compositions ranging from intermediate to felsic, are intrusive in the greenstone belts of Banfora, Houndé and Boromo. They also constitute the gneiss-granitoids of the Sideradougou, Diebougou, and Koudougou-Tumu complexes (Fig. 1). Ages of these plutons can be separated in four periods, with two peaks designated as Magmatic Event 1 (ME1) and 2 (ME2), coeval with major deformation phases (Baratoux et al., 2011; Grenholm et al., 2019a; Hirdes et al., 1996; Parra-Avila et al., 2017). Pre-ME1 magmatism is represented in SGGC by a poorly constrained U-Pb zircon age of 2243 ± 30 Ma in a hornblende and biotite gneiss in the north of the SGGC (Giovenazzo et al., 2018) and of 2312 ± 17 Ma on an inherited core from the Dabakala tonalite, south of the SGGC (Gasquet et al., 2003). The first magmatic peak

(ME1) is represented by layered tonalite, trondhjemite and granodiorite dated between 2160 and 2130 Ma. South of the studied area, ME1 plutons in Ivory Coast, correspond to “Comoé type” granodioritic biotite gneiss dated by U-Pb on zircon at 2152 ± 3 Ma, and to the “Bavé type” granitoid intrusion dated at 2137 +9/-7 Ma (U-Pb dating with Thermal Ionization Mass Spectrometry by zircon dissolution, Hirdes et al., 1996). The second magmatic peak (ME2) is characterized by granodiorite and amphibole-biotite granite forming plutons emplaced between 2120 Ma and 2100 Ma. The ME2 period is also characterized by emplacement of volcanic rocks (basalt, andesite, dacite, rhyolite, épiclastite) defined as the Bandamian cycle only described to the west of the OFSZ (Fig. 1) and dated between 2120 and 2080 Ma (Gasquet et al., 2003; Grenholm et al., 2019b; Hirdes et al., 1996; Mériaud et al., 2020). The post-ME2 magmatic period is represented by undeformed plutons of potassic and biotite granites that crystallized between 2110 Ma and 2070 Ma (Baratoux et al., 2011; Metelka et al., 2011; Parra-Avila et al., 2017, 2019).

Magmatic rocks of the ME1 and ME2 periods are characterized by a ductile fabric in continuity with the one of the Birimian series and the gneiss-granitoids, which have been variously interpreted. Some authors emphasize the impact of far-field forces derived from plate tectonics and either invoke the succession of D1 and D2 deformation phases reflecting early tangential tectonics followed by strike-slip dominated transpression (Baratoux et al., 2011; Metelka et al., 2011) or a progressive lateral flow of a weak lithosphere (Chardon et al., 2020). Others highlight the role of buoyancy forces and propose that the shallow-to moderately dipping foliation of the gneiss-granitoids records diapiric ascent of the TTG massifs in the Birimian series (Lompo, 2009, 2010; Vidal et al., 2009).

The Birimian series is affected by sub-greenschist to amphibolite facies metamorphic grade (Doumbia et al., 1998; Feybesse et al., 2006; Liégeois et al., 1991; Vidal and Alric, 1994). Metamorphic isogrades depict a greenschist to amphibolite facies metamorphic gradient that defines a contact aureole around granitoids plutons (Debat et al., 2003; Fontaine et al., 2017; Gueye et al., 2008; Pons et al., 1995) and delineates regional-scale domes cored by gneiss-granitoids (Block et al., 2015, 2016b; Vidal et al., 2009).

4. Results

4.1. Geology of the Mangodara district

4.1.1. Regional structure

The Mangodara district is characterized by a dome structure mantled by granodioritic gneiss that contains a variety of rafts and enclaves of amphibolite, micaschist and paragneiss ranging in size from the kilometer to the centimeter, and cored by tonalitic-trondhjemitic gneiss (Fig. 2). The contact between the granodioritic and tonalitic-trondhjemitic gneiss is marked by a crescent-shaped layer of two-mica tonalite along the southern boundary of the dome and by discontinuous lenses of trondhjemite along its north-eastern margin (station BMN33, Fig. 2). To the east and south of the dome, the granodioritic gneiss is intruded by monzogranitic to granitic plutons that we designate as Ganso-Gountiedougou granitoids (GG-granitoids), and by hornblende granodiorite, respectively. Amphibolite, micaschist and paragneiss rafts, as well as gneisses and granitoids contain pegmatites that are concordant to discordant relative to the structure of their hosts.

The preferred orientation of the rafts is parallel to the main foliation of the granodioritic gneiss and of the hornblende-biotite granodiorite. This foliation is marked by the preferred orientation of biotite, hornblende and mica-rich enclaves, but also by alternations of layers with different proportions of biotite, hornblende, quartz and feldspar. At the scale of the Mangodara district, foliation trajectories are roughly concentric and delineate the dome structure. In the granodioritic gneiss, foliation planes display a moderate to steep dips (between 20° and 60°) away from the core of the dome. Stretching and mineral lineation in the granodioritic gneiss have been identified only in the north-east of the district and are dominantly down dip. The foliation of the tonalitic-trondhjemitic core is typically concordant to the contact with the granodioritic gneiss but this contact is slightly discordant relative to the fabric of the mantling units. Within the tonalitic-trondhjemitic core, foliations planes also define two second order domes.

Magnetic lineaments (Chardon et al., 2020; Metelka et al., 2011) suggest the presence of shear zones flanking the northern and southern margins of the tonalitic-trondhjemitic core of the Mangodara dome. The asymmetric shape of the tonalitic-trondhjemitic core of the dome is consistent with an apparent anticlockwise rotation associated with a dextral sense of shear. These shear zones might connect to the Ouango Fitini Shear Zone (OFSZ, Chardon et al., 2020), which is interpreted as a D2 structure (Baratoux et al., 2011; Hirdes et al., 1996; Metelka et al., 2011). The northern shear zone has not been identified in the field but the southern one is marked, near Massadeyirikoro, by a subvertical NE-SW trending foliation in the paragneiss and in the hornblende-biotite granodiorite. A NW-SE-trending shear zone, designated as the Gountiédougou shear zone, cross-cuts the Mangodara district along the contact between the granodioritic gneiss and the GG-granitoids. This shear zone is marked by steep mylonitic zones with thickness between 1 and 30 cm affecting the granodioritic gneiss and the eastern-most pegmatites. These subvertical shear zones are connected with dispersed thin subhorizontal ones and are associated with retrogression of biotite and hornblende in chlorite and epidote. Doleritic and microgranitic dykes with sharp contacts cross-cut the different lithological units, and are attributed to post-Eburnean events.

4.1.2. Mantling units

Granodioritic gneiss, which dominates the mantling units of the Mangodara dome, is characterized by a composition and texture that is heterogeneous at the meter and centimeter scales but can be considered homogeneous at the kilometer scale (Fig. 3c to d). The average facies of the granodioritic gneiss consists of a groundmass of intermingled subhedral biotite, hornblende, plagioclase and rare K-feldspar with convoluted intergranular patches of anhedral quartz (Fig. 4). Locally, quartz and/or feldspar films are coating phenocrysts (Fig. 4b). A layering is locally marked by alternating centimeter-thick granitic veins with plagioclase phenocrysts (Fig. 3b) and hornblende-biotite-rich layers with microgranular texture (Fig. 3c) as well as by the preferred orientation of biotite and hornblende. Plagioclase and hornblende phenocrysts are surrounded by subhedral biotite and hornblende (Fig. 4a and 4b). Euhedral titanite and allanite are common, the latter being partially retrogressed to epidote, and subhedral apatite. Epidote occurs as subhedral to anhedral magmatic crystals cored by allanite, as inclusion in plagioclase and amphibole, or as secondary minerals within the groundmass surrounding micas and hornblende. Zircon is present as micro-inclusions in biotite, surrounded by black aureoles typical of radiation damage. Apatite forms subhedral to euhedral crystals (size < 200 µm) within plagioclase, quartz, and biotite. Opaque minerals (size < 500 µm) are associated with biotite and hornblende aggregates. Rare microgranular mesocratic enclaves, composed of hornblende, biotite, plagioclase and quartz, form ovoid meter-scale bodies reaching 10 cm in thickness, elongated in foliation planes of the granodioritic gneiss. East of the dome, near Gountiedougou, the granodioritic gneiss grades into granite collected in dilatant sites accommodated by heterogeneous deformation (Fig. 3d). In this area, the contact with the granodioritic gneiss is marked by leucocratic veins concordant to the foliation, which are locally folded (Fig. 3e).

Amphibolite and micaschist rafts are characterized at the outcrop scale by a composite foliation attributed to transposition of a primary magmatic-sedimentary layering into a schistosity (S_n) associated with rootless isoclinal folds, boudins and shear bands (Fig. 5a and b). Amphibolites consist of hornblendite and hornblende gabbro. Hornblendite is fine-grained with poikilitic hornblende and plagioclase that contain lobate quartz. Yellowish sub-circular epidote locally occurs as an alteration product of hornblende. Hornblendite hosts networks of 1 to 10 cm thick veins dominantly composed of plagioclase with some hornblende. These veins can be either concordant or discordant to the foliation and are locally isoclinally folded. Their margins are characterized by accumulation of hornblende crystals (Fig. 5c), which suggests segregation of a melt from the plagioclase-hornblende matrix. Elongated enclaves of amphibolite, dispersed in the granodioritic gneiss, grade into layers with a gabbroic to monzogabbroic composition made of plagioclase and hornblende, locally megacrystic (euhedral, up to centimeter sized, in a medium-grained matrix). Micaschists include mafic schists hosting porphyroblastic hornblende, biotite schist, muscovite-biotite schist, and sericite-schist (Fig. 5b, 5d). Micaschists are intruded by centimeter-thick concordant granitic dykelets and contain quartz veins.

Paragneiss rafts are common south of the Mangodara dome and the largest one is pinched between the two-mica tonalite and the hornblende-biotite granodiorite. They are characterized by alternations of 20 to 30 cm thick quartz-feldspar-rich and mica-rich layers interpreted as former beds of graywacke and pelite (Fig. 6a and b) transposed in a composite foliation. The metamorphic mineral assemblage of coarser mica-rich layers includes sillimanite as well as staurolite and garnet porphyroblasts, which are symptomatic of amphibolite facies metamorphism (Fig. 6a, c and d). In addition to the inherited transposed sedimentary bedding, the presence of quartz-feldspar veins including some biotite with a coarse-grain texture devoid of any solid-state fabric and with diffuse contacts are indicative of segregation of partial melts (Fig. 6b). A first schistosity, designated as S_n, is delineated by the preferred orientation of sillimanite and biotite (Fig. 6a, c and d). It is affected by crenulation folds associated with an axial planar schistosity S_{n+1} marked by euhedral biotite associated with sillimanite and white mica. In zones of weak transposition, staurolite and garnet porphyroblasts are wrapped into the S_n schistosity but contain inclusions that point to synkinematic crystallization. In particular, inclusions in staurolite delineate an internal schistosity in continuity with the S_n schistosity of the matrix. This internal schistosity is crenulated with an axial planar S_{n+1}, which is not in continuity with the S_{n+1} schistosity of the matrix. This is consistent with an anticlockwise rotation of staurolite porphyroblasts after the development of S_{n+1} (Fig. 6d). Staurolite-sillimanite-garnet paragneiss grades into migmatitic paragneiss with leucosome veins preferentially developed in metapelitic layers. Migmatitic paragneiss with more than 20 % of leucosome displays a continuous network of concordant and discordant veins. Migmatitic paragneiss grades into the granodioritic gneiss by alternations of mesocratic layers hosting garnet-columbite pegmatites, next to mica-rich and leucosome-bearing layers (Fig. 7a to d). Alternations of leucosome veins with mesosome layers define a synmigmatitic foliation, which is parallel to the S_{n+1} schistosity delineated by a sillimanite-biotite-chlorite-staurolite-garnet assemblage (Fig. 7e). Garnet occurs as inclusion-rich porphyroblasts but also as crystals devoid of inclusions within or along the boundaries of leucosome veins, suggesting garnet growth during incongruent melting (Fig. 7e and f). Concordant leucosome veins are locally in textural continuity with pegmatite dykes with diffuse contacts marked by biotite selvages.

4.1.3. Core units

The tonalitic-trondhjemitic gneiss, dominating the core of the Mangodara dome, is significantly more leucocratic than the granodioritic gneiss. It is characterized by a hypidiomorphic texture with abundant oligoclase (up to 60%), quartz, rare microcline, biotite, and up to centimetric euhedral magnetite (Fig. 8a, Fig. 9). Green hornblende is rare, and appears as anhedral crystals associated with biotite. Accessory minerals are allanite-epidote, titanite, and apatite. Quartz forms intergranular patches that are locally affected by undulatory extinction and recrystallization into equant neoblasts. A foliation is depicted by the preferred orientation of euhedral biotite and hornblende, locally forming thin layers.

The foliated tonalitic gneiss typically displays a network of texturally continuous hornblende tonalite veins and pegmatite veins, which are concordant to discordant to the foliation and localized in zones of heterogeneous deformation such as shear zones (Fig. 8b, c and d). This tonalitic gneiss locally forms rafts in a leucotonalite with a homogeneous composition and magmatic texture (Fig. 8c). Hornblende tonalite veins contain mafic clots with hexagonal, diamond- or square-shaped sections, composed of a poikilitic assemblage of hornblende and biotite enclosing lobate quartz, which are interpreted as pseudomorphs after hornblende (Fig. 8e).

The tonalitic-trondhjemitic gneiss also contains a few layers of granodioritic gneiss, of epidotized migmatitic amphibolite with folded concordant leucosome layers (up to 5cm wide) alternating with biotite-rich layers and pegmatite veins (Fig. 3f).

4.1.4. Plutonic rocks

Plutonic rocks of the Mangodara dome are usually in diffuse contact with the host gneisses and mostly concordant to the regional structure, but they locally show sharper intrusive contacts. They are characterized by a magmatic fabric with a preferred orientation of euhedral minerals, only locally slightly overprinted by solid-state deformation.

GG-granitoids exposed in the eastern part of the Mangodara dome, in gradual contact with the granodioritic gneiss, have a composition varying between monzogranite and biotite granite with megacrystic K-feldspar, quartz, plagioclase, biotite and hornblende (Fig. 10a, b and c). Their magmatic fabric is also delineated by disseminated biotite aggregates. GG-granitoids contain decimeter to meter-scale angular enclaves of gabbro, diorite, granodiorite and monzogranite with sharp boundaries. In contrast, some enclaves of gabbro are clustered and aligned in diffuse and mingled contact with the host granitoid (Fig. 10b). Rafts of granodioritic gneiss are abundant in the GG-granitoids east of Gountiedougou. In this part of the district, the youngest magmatic rock is a biotite porphyritic granite, intrusive in other GG-granitoid, mostly composed of megacrystic orthoclase, quartz, plagioclase, biotite and hornblende (Fig. 10c). Commonly, GG-granitoids contain titanite forming euhedral lozenges of up to 1 cm in size, and epidote anhedral or granular crystals, locally showing a concentric zonation. Other accessory minerals are zoned allanite, zircon, and opaques.

The trondhjemite lens along the north-eastern margin of the core of the Mangodara dome is composed of plagioclase, biotite, rare quartz and magnetite. The preferred orientation of biotite delineates a foliation and a network of anastomosed ductile shear zones. The trondhjemite hosts thin quartz-felspar veins concordant to the foliation.

The hornblende-biotite granodiorite, forming a pluton within the granodioritic gneiss to the south of the Mangodara dome close to the contact with the tonalitic-trondhjemitic core, is typified by abundance of mica-rich enclaves (Fig. 10d). It is composed of plagioclase, quartz, hornblende, biotite, magnetite, and accessory apatite and allanite-epidote. Locally, plagioclase is megacrystic and concentrically zoned, reaching 3 cm in size. The centimeter to decimeter-scale mica-rich enclaves (< 5% of the rock volume) are ovoid to elongated and composed of aggregates of biotite and rare hornblende. Some enclaves of hornblende-biotite granodiorite found in garnet-columbite pegmatite contain a network of texturally continuous concordant and discordant granitic veins that are folded with the foliation.

The two-mica tonalite that delineates the contact between the mantling and core units of the Mangodara dome, is composed of quartz, plagioclase, minor K-felspar, biotite and muscovite. Rare subhedral to anhedral K-feldspar crystals are encompassed in a matrix dominated by quartz featuring evidence of high-T recrystallization (subgrains with irregular interpenetrating boundaries). Accessory minerals are euhedral apatite, allanite with epidote corona, and subhedral to anhedral epidote associated with biotite, and magnetite. The texture of the two-mica tonalite is globally fine-grained and hypidiomorphic but a magmatic fabric is locally delineated by the preferred orientation of decimeter-scale enclaves of tonalitic-trondhjemitic gneiss (Fig. 10e) and the preferred orientation of biotite-rich layers. The two-mica tonalite contains also rare feldspar-tourmaline pegmatites that form decimeter-scale pockets or meter-wide veins with diffuse contacts.

4.1.5. Pegmatites

The gneisses and granitoids of the Mangodara district comprise swarms of pegmatite dykes that are subdivided into (i) titanite-allanite-bearing pegmatite, (ii) apatite-zircon-bearing pegmatites, (iii) garnet-columbite-bearing pegmatites, and (iv) garnet-REE-bearing pegmatites.

Titanite-allanite pegmatites form a network of patches and veins both concordant and discordant to the fabric of the tonalitic-trondhjemitic gneiss (Fig. 11a). Concordant titanite-allanite pegmatitic veins are coarse-grained and display diffuse and progressive contacts. They are in textural continuity with discordant dykes that are regularly distributed in dilatant sites. Titanite-allanite pegmatites are mainly composed of oligoclase, quartz, rare K-feldspar, biotite and magnetite, an assemblage identical to that of the host gneiss. The modal content of biotite is $< 5\%$, and this mica occurs as isolated flakes or clusters. Accessory minerals include apatite, titanite, ilmenite, allanite, epidote, and zircon.

Apatite-zircon pegmatites are less common, with only four dykes identified so far. They are hosted in the granodioritic gneiss where they form veins that are never thicker than 1 meter, discordant to the foliation of the granodioritic gneiss but having a diffuse contact with it. Some of these veins are folded in the granodioritic gneiss. Mineralogically, the apatite-zircon pegmatites are similar to the titanite-allanite variety, but they lack titanite and contain higher amounts of apatite (up to 5 wt% in some dikes) and zircon (widespread as inclusions in biotite).

Garnet-columbite pegmatites (Li, Nb enriched) are found in amphibolite, paragneiss, granodioritic gneiss, hornblende-biotite granodiorite, and two-mica tonalite. They form a swarm of veins and dykes with a width that can reach 300 m, and are mostly discordant to the fabric of their hosts. They display an aplitic to graphic texture with local megacrystic alkali feldspars, plagioclase, biotite, muscovite, spessartine-almandine garnet, cleavelandite, magnetite, and accessory apatite, tourmaline intergrown with quartz, monazite, xenotime, zircon and columbite-tantalite. Some pegmatite veins are in textural continuity with concordant leucosome veins of migmatitic paragneiss but others are transposed, folded or boudinaged with cuspate shapes into the foliation of the paragneiss and granodioritic gneiss (Fig. 6a, Fig. 11c, d and e). Some of these deformed pegmatites are zoned, with a margin marked by polycrystalline feldspar crystals with a stockscheider texture and a core dominated by centimetric quartz crystals (Fig. 11d). Garnet-columbite pegmatite dykes contain blocky meter-scale enclaves of paragneiss, micaschist, and hornblende-biotite granodiorite. South of Massadeyirikoro, garnet-columbite pegmatite dykes cross-cut apatite-zircon pegmatite dykes (Fig. 11b). At the grain scale, the boundary between the two pegmatite types is rather irregular and follows the shape of the bordering crystals (Fig. 12), suggesting that a part of the apatite-zircon pegmatite (quartz-plagioclase-biotite assemblage) has been replaced by a subsequent pulse of magma, which crystallized into a quartz-feldspar-muscovite-garnet assemblage.

Garnet-REE pegmatites (enriched in Ti, Y and heavy rare earth elements, the latter abbreviated as HREE) are restricted to the eastern side of the Mangodara district (more than thirty dykes over a surface of about 10 km^2). They are hosted in granodioritic gneiss (Fig. 11f and g) and GG-granitoids. They are metric to plurimetric in size with an average strike of N160 and a dip that ranges from horizontal to subvertical. They are characterized by the predominance of biotite over muscovite, presence of Ti-oxide (ilmenite-pyrophanite), epidote, rare tourmaline, REE-rich metamict accessory minerals (similar in composition with euxenite or aeschynite) and absence of phosphate minerals. Some dykes of garnet-REE pegmatites, which contain epidote, rare micas and rare garnet, are exposed in textural continuity with granitic veins concordant to the foliation of the granodioritic gneiss (Fig. 3e, Fig. 11f).

4.2. Metamorphism

Metamorphic rocks of the Mangodara district display a variety of mineral paragenesis indicative of pervasive greenschist facies metamorphism, as illustrated by rafts of sericite-muscovite-biotite schist in the northeast of the district, to amphibolite facies metamorphism marked by hornblendite and paragneiss in the central part of the district (Fig. 13). Northeast of the dome, amphibolite and micaschist contain porphyroblastic hornblende, indicating pervasive amphibolite facies was reached with T > 450–500 °C (Liou et al., 1974; Maruyama et al., 1983; Moody et al., 1983). Furthermore, the presence of tonalitic leucosome veins in these rocks suggests partial melting of amphibolites, which requires a temperature of about 750 °C under fluid-absent condition (Rapp et al., 1991; Rushmer, 1991; Wolf and Wyllie, 1994; Wyllie and Wolf, 1993) or 650 °C in hydrated conditions (Green et al., 2016; Palin et al., 2016). Paragneiss rafts in the central and southern parts of the studied area are characterized by a quartz-feldspar-biotite-sillimanite-garnet±staurolite±muscovite±chlorite mineral assemblage (Fig. 6c and d) that is also symptomatic of widespread amphibolite facies metamorphism. The structural-textural position of these minerals indicates a first mineral paragenesis marked by an association of fibrolitic sillimanite with biotite (S_n fabric). Garnet and staurolite, which form porphyroblasts superimposed on the sillimanite-biotite schistosity, are attributed to a second mineral paragenesis (transition to S_{n+1}). In migmatitic paragneiss, garnet-bearing leucosome veins are concordant to a foliation delineated by the preferred orientation of interlayered sillimanite-biotite-chlorite enclosing garnet and staurolite porphyroblasts, suggesting that melt segregation occurred in the presence of these minerals.

The calculated pseudosection of a garnet-staurolite bearing paragneiss (Fig. 14a) is consistent with phase equilibria models of metapelites. Staurolite is stable for T < 670 °C (Pattison and Spear, 2018; Tinkham et al., 2001), about 10 to 50 °C below the solidus. Under a pressure of 7 kbar, staurolite can be expected to be stable with anatectic melt through the disequilibrium reaction garnet = staurolite. That proposition is consistent with synkinematic crystallization of the two minerals, as observed in thin section (Fig. 6c and d). Supersolidus staurolite is consistent with a temperature of about 675–700 °C (García-Casco et al., 2003). Garnet porphyroblasts suggest a pressure above 4.5 kbar in paragneiss, and above 5 kbar in leucosomes (Patiño Douce, 1999; Spear et al., 1999). Subsolidus stability of sillimanite requires a T > 550 °C (Bohlen et al., 1983; Holdaway and Mukhopadhyay, 1993; Pattison, 1992; Whitney, 2002), and a P < 7 kbar. The absence of stable cordierite in paragneiss points to a P > 5kbar. These observations constrain the metamorphic assemblage of the paragneiss to near-solidus conditions: 650–680 °C, 6–7 kbar. It is noticeable that for a temperature exceeding the biotite-breakdown reaction (> 790 °C), the modelled mineral composition of the partially molten paragneiss is close to the one of the granodioritic gneiss (Fig. 14c).

The calculated pseudosection of the amphibolite (Fig. 14b) is in agreement with sub-solidus composition dominated by hornblende and plagioclase, except that clinopyroxene, which should be present in minor content, is unseen in the rock sample. The modelled solidus occurs at higher temperature than in paragneiss (700–750 °C). Partial melting of the amphibolite promotes the breakdown of hornblende and the crystallization of orthopyroxene, whereas plagioclase fraction remains constant.

Magmatic epidote is present in granodioritic gneiss, tonalitic-trondhjemitic gneiss, hornblende-biotite granodiorite with mica-rich enclaves and in GG-granitoids. Experiments of epidote saturation in felsic to intermediate magma show that crystallization of magmatic epidote requires a P higher than 5 kbar in presence of water (Schmidt and Poli, 2004; Schmidt and Thompson, 1996). This value defines a minimum pressure for crystallisation in the epidote-bearing granitoids of the Mangodara district.

Aluminium-in-hornblende is a calibrated barometer valid for intrusive rocks, assuming hornblende in equilibrium with alkali feldspar, plagioclase, biotite, iron titanium oxide and titanite (Hammarstrom and Zen, 1986). The major composition of hornblende from granodioritic gneiss, hornblende and biotite granodiorite with mica-rich enclaves, and hornblende tonalite veins in tonalitic-trondhjemitic gneiss ranges from magnesio-hastingsite to ferro-pargasite. Depth of crystallization of hornblende is estimated using the various published parameters (Hollister et al., 1987; Johnson and Rutherford, 1989; Mutch et al., 2016; Schmidt, 1992; Thomas and Ernst, 1990). Averages of calculated pressure of granodioritic gneiss and hornblende-biotite granodiorite are equivalent and are between 4.4 kbar and 6.6 kbar (*Table 3*). Calculated pressure in hornblende tonalite vein is slightly lower, between 4.0 kbar and 6.1 kbar and provide a constraint on the pressure of melt crystallization. The low diffusion rate of Al in hornblende under submagmatic conditions reduces the possibility of resetting of the Al-in-hornblende barometer by metamorphism. So, the pressure inferred from hornblende of the granodioritic and tonalitic-trondhjemitic gneisses is interpreted to reflect their depth of crystallization.

The prevalence of biotite and hornblende in gneisses and granitoids, and the absence of orthopyroxene imply that the dehydration reactions marking the transition to granulite facies did not occur. The reported presence of kyanite in greenstones in NE of the Mangodara district (Ilboudo et al., 2017b), and the occurrence of sillimanite, garnet and staurolite in paragneiss, reflect a moderate P and high T metamorphic gradient, close of the solidus of paragneiss. The metamorphism recorded in the amphibolite, micaschist and the paragneiss rafts corresponds to a sillimanite MP-HT metamorphic facies. This is consistent with burial of the Birimian series along a geothermal gradient between 20 °C/km and 40 °C/km, which corresponds to the average thermal gradient identified in the greenstone belts of the Baoule-Mossi domain (Ganne et al., 2014).

4.3. Geochronology

4.3.1. U-Pb dating on zircon

Zircon dating was completed in situ on the sample BMN28 of titanite-allanite type pegmatite. Zircon occurs in the pegmatite as subhedral to euhedral crystals with rectangular to prismatic shape, inferior to 400 µm in length, dominantly hosted in biotite. Cathodoluminescence imaging of zircon reveals large cores and a rim marked by oscillatory zoning (Fig. 15a). Irregular patches blurring the oscillatory textures are attributed to metamictization, which may explain the discordant analyses.

All analyses (Table 1) scatter along a Discordia with an upper intercept at 2078 ± 37 Ma, and lower intercept close to present day at 32 ± 27 Ma (Fig. 15b). Most of the concordant analyses are located in zircon cores, but discordant data are located in both cores and rims (Fig. 15c). Zircon age was calculated selecting concordant data and propagating decay constant errors, with uncertainties of 2σ multiplied by the square root of the mean square weighted deviation (MSWD) at 95 % of confidence level. The obtained age is 2094.3 ± 8.8 Ma (MSWD = 1.6). In absence of a significant disparity between cores and rim, this age is considered to date the crystallization of the titanite-allanite pegmatite.

4.3.2. U-Pb dating on apatite

U-Pb dating was completed on apatite from the granodioritic gneiss (BMN20B), the tonalitic-trondhjemitic gneiss (BMN11), and the apatite-zircon pegmatite (BMN20).

Apatite in gneisses and apatite-zircon pegmatites occurs as subhedral to euhedral crystals hosted in plagioclase, quartz, biotite and magnetite. Internal zoning of apatite crystals is unseen with SEM, but is visible with cathodoluminescence imaging. Oscillatory to zoned cores are surrounded by homogeneous rims (Fig. 16a, b and c). Average size of analyzed crystals is 200 µm in granodioritic gneiss, 300 µm in tonalitic-trondhjemitic gneiss and 1 mm in apatite-zircon type pegmatite.

Obtained data (Table 2) were plotted on the Tera-Wasserburg diagram (Tera and Wasserburg, 1972) and ages were calculated by determination of the Discordia intercept with 95 % of level confidence. Apatite yields average ages of 2041 ± 33 Ma (MSWD = 3.1) for the granodioritic gneiss, 2094 ± 21 Ma (MSWD = 1.6) for the tonalitic-trondhjemitic gneiss, and 2055 ± 20 Ma (MSWD = 4.9) for apatite-zircon type pegmatite.

4.4. Whole-rock geochemistry

Geochemical data of representative samples of the different lithological facies exposed in the Mangodara district are reported in Table 4. They are subdivided in (i) amphibolite and micaschist, (ii) paragneiss, (iii) gneisses and plutonic rocks comprising granodioritic gneiss, microgranular mesocratic enclave in granodioritic gneiss, tonalitic-trondhjemitic gneiss, trondhjemite, hornblende-biotite granodiorite, two-mica tonalite, biotite porphyritic granite (GG-granitoid), biotite monzogranite (GG-granitoid) and monzogabbro.

4.4.1. Amphibolites and micaschists

Samples of amphibolite and micaschist are characterized by a low K content (0.25–0.49 wt% K_2O), a relative depletion in large-ion lithophile elements (LILE) like Cs, Rb and Ba, and a minor fractionation of light rare earth elements (LREE) vs HREE (La_N/Yb_N = 4.6–8.1). Enrichment in LREE relative to HREE, and negative Nb and Ti anomalies are characteristic of tholeiitic to calc-alkaline basalts and andesites such as the ones exposed in the Houndé and Banfora greenstone belts (Fig. 17a) (Baratoux et al., 2011; Ilboudo et al., 2020), but also in many areas of the Baoule-Mossi domain (Béziat et al., 2000; Ilboudo et al., 2017a; Lompo, 2009; Lüdtke et al., 1998; Pouclet et al., 1996). Amphibolite has low Si (52.3 wt% < SiO_2 < 54.1 wt%), high Ca (9.63 wt% < CaO < 10.15 wt%) and high ferromagnesian content (Fe_2O_3 = 9.15–11.11 wt%, Mg# = 0.55–0.57, Fe_2O_3+MgO+MnO+TiO_2 = 11.6–19.5 wt%). Transition metals are elevated in amphibolite, particularly in the sample BMN109, pointing to a primitive mantellic source (Sun and McDonough, 1989) (high Cr: 87–1129 ppm, Ni: 24–313 ppm and Co: 27–44 ppm). Micaschist is distinguished from the amphibolite by higher Si content (SiO_2~ 61.68 wt%), lower CaO (~6.92 wt%), lower Fe (Fe_2O_3~8.11 wt%) and lower MgO (~2.41 wt%, Mg# = 0.37), which suggest that its protolith corresponds either to a more felsic magmatic rock or a more mature sediment.

4.4.2. Paragneiss

The paragneiss has a metapelitic composition, with SiO_2~61.66%, Al_2O_3~17.95 wt%, K_2O~2.94 wt%, and Na_2O~2.08 wt%. It is rich in Fe and Mg and shares with amphibolite and micaschist a relatively high content in transition metals, such as Cr (217 ppm), V (139 ppm), Ni (71 ppm), and a low Th/Sc ratio (0.17). Its chondrite-normalized REE pattern has a slight negative slope, with no Eu anomaly, and a flat trend in the HREE (Fig. 17a), like the amphibolite and the micaschist.

Nonetheless, the paragneiss is poor in Fe-Mg compared to the amphibolite and the micaschist (Fe_2O_3 = 7.85 wt%, Mg# = 0.42, Fe_2O_3+MgO+MnO+TiO_2 = 11.51 wt%). It is also enriched in LILE (Ba = 608 ppm, Rb = 114 ppm, Cs = 5 ppm) compared to the average continental crust (Rudnick and Gao, 2003), but also to the granodioritic gneiss and K-rich granitoids of the Mangodara district.

4.4.3. Granodioritic-tonalitic-trondhjemitic gneisses and plutonic rocks

In the Nesbitt and Young diagram (Fig. 18a, Nesbitt and Young, 1982, 1984), gneisses and granitoids of the Mangodara district plot just below the feldspar join, which can be attributed to the presence of ferromagnesian minerals and indicates that these rocks were not significantly affected by metasomatism or chemical weathering.

Gneiss and granitoids correspond to calc-alkalic granitoids with metaluminous composition (Fig. 18b), like most Eburnean granitoids (Castaing et al., 2003; Ilboudo et al., 2020). The granodioritic gneiss, the hornblende-biotite granodiorite with mica-rich enclaves and the GG-granitoids have chemical affinities typical of a calc-alkaline K-rich series, whereas the tonalitic-trondhjemitic gneiss, the trondhjemite, and the two-mica tonalite have the chemical affinity of a Na-rich series (Fig. 18c). Their modal composition in the Quartz, Alkali feldspar, Plagioclase (QAP) diagram widely correspond to granodiorite or tonalite, but the trondhjemite lies in domain of diorite (Fig. 18d). Except for the trondhjemite and the monzogabbro (SiO_2 < 52 wt%, Fig. 18c and e), the gneisses and other granitoids match some of the geochemical criteria of TTG *sensu stricto*: high SiO_2 (62–72 wt%, Fig. 18e), significant Na_2O (3.85–5.85 wt%), absent Eu and Sr anomalies, LREE >> HREE (high La/Yb, Fig.

18f), negative Nb-Ta-Ti anomalies (Martin and Moyen, 2002). Moreover, they match subcategories of middle- to high pressure TTG features (Moyen, 2011), namely, moderate to high Sr/Y ratio (26–215, Fig. 18f), high Sr (473–788), low Ce/Sr (< 0.18). Characteristics of the high pressure TTG typically correspond to the ones of tonalitic-trondhjemitic gneiss and of the two-mica tonalite (Fig. 18f).

Granodioritic gneiss and tonalitic-trondhjemitic gneiss have low Mg#, between 0.38 and 0.52, which are lower than the values for the amphibolite (0.55–0.57) but encompass the one for the paragneiss (0.42). Chondrite-normalized REE patterns of both gneiss types have negative slopes like those shown by plutonic rocks (Fig. 17b). The primitive mantle-normalized pattern of the gneisses (Fig. 17d) unveils a higher enrichment in LILE (Cs, Rb, Ba) than in high field-strength elements (HFSE; Hf, Zr, Y, HREE), which is characteristic of the paragneiss, of granitoids in the Mangodara district and also of the bulk continental crust (Rudnick and Gao, 2003). Negative Nb, Ta and Ti anomalies of the granodioritic gneiss are similar to those of the amphibolite, micaschist and paragneiss (Fig. 17c and d).

The granodioritic gneiss and microgranular enclave are characterized by high K content (2.74–3.33 wt% K_2O), whereas the tonalitic-trondhjemitic gneiss has a low K content (0.81–1.2 wt% K_2O) but is richer in Na (4.95–5.85 wt% Na_2O). The high Na content in tonalitic-trondhjemitic gneiss is consistent with the predominance of oligoclase in this rock. The tonalitic-trondhjemitic gneiss presents a higher fractionation of LREE vs HREE (La_N/Yb_N = 20–39) than the granodioritic orthogneiss (La_N/Yb_N = 16–25) and is depleted in REE. The tonalitic-trondhjemitic gneiss is also depleted in transition metals (40–85 ppm Cr, 24–61 ppm Cu, 5–40 ppm Ni, 3–10 ppm Co). These depletions might be induced by fractional crystallization leading to segregation of early crystallizing mafic minerals.

The hornblende-biotite granodiorite, the GG-granitoids and the trondhjemite are mostly metaluminous, whereas the two-mica tonalite is weakly peraluminous (Fig. 18b). They are depleted in HFSE and lie in the domain of unfractionated M-type, I-type and S-type granites according to the criteria of Whalen et al. (1987) used for discrimination of A-type. This indicates that they are poorly differentiated magma, and do not match the signature of anorogenic granitoids. Plutonic rocks are subdivided into

K-rich and Na-rich series, which can be extended to the gneisses (K-rich granodioritic gneiss, and Na-rich tonalitic-trondhjemitic gneiss).

The K-rich series, comprising the hornblende-biotite granodiorite with mica-rich enclaves and the GG-granitoids, is defined by a high K content (2.78–3.56 wt% K_2O, Fig. 18c), low Na content (3.65–4.29 wt% Na_2O) and intermediate Mg# (0.33–0.42). They are also characterized by high content in Sr (473–788 ppm), and Ba (606–1071 ppm). The monzogabbro corresponds to the K-poor mafic end-member of this series (2.28 wt% K_2O, SiO_2 = 51.86 wt%, Mg# = 0.49) and displays a slightly higher content in Na (4.30 wt% Na_2O), relatively high P content (0.45 wt% P_2O_5), weak fractionation of LREE vs HREE (La_N/Yb_N ~9), and higher HREE content. K-rich granitoids lay in the high-K calc-alkaline domain in the SiO_2 vs K_2O diagram (Fig. 18c).

The Na-rich series, composed of the trondhjemite and the two-mica tonalite, is defined by low K, high Na contents (1.39–1.60 wt% K_2O, 5.46–7.12 wt% Na_2O), and by intermediate Mg# (0.37–0.44). Their high Na content is correlated with the abundance of oligoclase. The trondhjemite is singularized by a low silica content (SiO_2~59.23 wt%), which sets it in the compositional domain of medium calc-alkaline series. Na-rich granitoids are globally depleted in REE relative to the K-rich granitoids. The two-mica tonalite presents the highest LREE/HREE fractionation among the plutonic rocks and is strongly depleted in Nb and Ta, like the tonalitic-trondhjemitic gneiss.

4.4.4. Pegmatites

An intrinsic characteristic of pegmatites is to feature variable and commonly coarse grain size and heterogeneous textures. Therefore, despite our efforts during sampling, the major-element composition obtained from whole-rock data should be taken with caution. Nevertheless, some general trends can be identified. In particular, the ratios of elements (e.g. K/Rb, Nb/Ta) that have similar geochemical behaviors can be considered to be relatively independent of the major mineral mode and be used as proxy of the degree of magmatic differentiation with respect to a primitive composition (Ballouard et al., 2016; Bau, 1996; Černý et al., 1985; Shaw, 1968; Taylor, 1965). For instance, pegmatites at

Mangodara have lower K/Rb and Ca/Cs ratios compared to granitoids (Table 4, Fig. 18g), except for titanite-allanite pegmatite, which is characterized by high K/Rb (989) and Ca/Cs (~68900) ratios (Table 4). Also compared to granites, pegmatites are manifestly characterized by low Zr/Hf and Nb/Ta ratios (Nb/Ta < 7, Zr/Hf < 34, Table 4, Fig. 18h).

Titanite-allanite pegmatite has a high Na content (5.17 wt%), whereas P is below the detection limit, although apatite is present in the sampled dyke. Again, this may be due to sampling-induced bias. It is also characterized by lower contents in Cs, Rb, Nb, Ta, and HREE than the other pegmatite types (see Table 4, Fig. 17f), and, specific to this variety, a markedly positive Eu anomaly.

Apatite-zircon pegmatite is also Na-rich (6.32 w%) and has high REE contents (83 ppm), consistent with the abundance of apatite in this sample (Fig. 17e). Its chondrite-normalized REE spider diagram shows a relative depletion in LREE which increase slightly from La to Sm, and a negative Eu anomaly. Another difference with the other varieties is its enrichment in LILE and HFSE (Nb, Ta, Zr, Hf) (Fig. 17f).

The garnet-columbite pegmatite has high K and low Ca contents (K_2O~5.46 wt%; CaO < 0.47 wt%), consistent with the abundance of K-feldspar and the albitic composition of plagioclase. This pegmatite is rich in LILE (Fig. 17e) and possesses the lowest values in K/Rb (180) and Ca/Cs (899) of all pegmatites. Its chondrite-normalized REE pattern show a depletion in HREE, and a strong negative Eu anomaly.

Finally, the garnet-REE pegmatite is Na-rich (Na_2O ~ 6.35 wt%) with low K_2O (0.52 wt%). It is significantly enriched in HREE, as indicated by the positive slope in chondrite-normalized HREE pattern. It has a lower content in LILE than the other pegmatites (particularly in Ba), but is richer in U and Th.

5. Discussion

5.1. Protoliths of amphibolite, micaschist and paragneiss

Amphibolite and micaschist rafts are very heterogeneous in mineralogy (variably rich in muscovite, sericite, biotite or hornblende), likely reflecting the heterogeneity of their protoliths. The REE pattern and negative Nb, Ta and Ti anomalies of amphibolite and micaschist samples show similarities with Birimian calc-alkaline basalt and andesite (Fig. 17b), suggesting that they may represent metamorphic equivalents of these rocks. This interpretation is consistent with the greenschist facies metamorphic gradient observed in alternating sequences of mafic-felsic volcanic rocks (basalts, andesite, dacite and rhyolite) with metapelites-metagreywackes of the Banfora greenstone belt. Indeed, Birimian series evolves to amphibolite facies with the transformation of basalt to amphibolite and occurrence of kyanite+staurolite+garnet in metarhyolites (Ilboudo et al., 2017b) near the border of the SGGC, to the north-west of the Mangodara district (Fig. 19).

The structure and geochemical composition of the paragneiss is typical of a detrital sedimentary protolith made of alternations of pelites and greywackes, which are also sedimentary rocks occurring in Birimian greenstone belts (Asiedu et al., 2004; McFarlane et al., 2011; Roddaz et al., 2007). The low Th/Sc ratio (0.17) and high Fe-Mg and transition metal (Cr, V, Ni) contents of the paragneiss, together with REE pattern being identical with those of amphibolite and micaschist are consistent with a predominant mafic source for their sedimentary protolith, likely derived from erosion of nearby greenstone belts.

5.2. Nature and protoliths of the granodioritic and tonalitic-trondhjemitic gneisses

5.2.1. Diatexite model vs plutonic model

The various gneisses and associated plutonic rocks exposed at the lowest structural level of the Baoulé-Mossi domain, loosely designated as gneiss-granitoid complexes, had been first considered to represent the Archean basement of the Birimian series (Arnould, 1961; Ducellier, 1963; Hottin and Ouedraogo, 1975; Tagini, 1971). This proposition was later discarded when U-Pb geochronology on zircon showed Paleoproterozoic values and no hint of Archean ages (Gasquet et al., 2003; Grenholm et al., 2019a; Parra-Avila et al., 2017; Wane et al., 2018). In the Mangodara district, granodioritic and tonalitic gneisses contain enclaves and rafts of amphibolite, micaschist and paragneiss, attributed to the Birimian series. These occurrences confirm the absence of basement rocks in the Mangodara district, even at the lowest exposed structural level.

Pursuing this line of reasoning, several authors proposed that the gneiss-granitoid complexes correspond to plutonic rocks that intruded the greenstone belts during the Eburnean orogeny (Gasquet et al., 2003; Vidal et al., 2009) based on the presence/absence of layering and the predominance of a magmatic texture or ductile fabric, further distinguished in syntectonic and late-tectonic intrusions (Gasquet et al., 2003; Hirdes et al., 1996). On the other hand, Gasquet et al. (2003) used the similarity in isotopic signatures (εNd, and $^{87}Sr/^{86}Sr$) of these granitoid-gneisses with the ones of the Birimian series (basalt and granite) to infer a common source for all these magmatic rocks.

In the Mangodara district, our structural analysis shows that the granodioritic and tonalitic gneisses occupy a distinct structural position. The granodioritic gneiss is mantling a dome cored by tonalitic gneiss (Fig. 19). If one considers the plutonic model, this relative position would imply that the granodioritic gneiss formed a regional scale laccolith overlying a pluton of tonalitic-trondhjemitic gneiss. Alternatively, this distribution could result from crustal-scale melt/crystal segregation within a partially molten orogenic root (Vanderhaeghe, 2009), whereby these gneisses could correspond to diatexites. In other words, they would represent former partially molten rocks characterized by a heterogeneous groundmass of granitic composition enclosing enclaves of gneisses and schists (Brown, 1973; Brown et al., 1995; Burg and Vanderhaeghe, 1993; Cavalcante et al., 2016; Martini et al., 2019; Mehnert, 1968; Saha-Fouotsa et al., 2019; Sawyer, 1991; Schwindinger and Weinberg, 2017; Vanderhaeghe, 2009, 2001; Vanderhaeghe et al., 1999; Weinberg et al., 2013). The observation of a magmatic fabric overprinted by ductile deformation under sub-magmatic to solid state conditions, indicating a temperature of about 650 °C (Drury and Urai, 1990; Gapais and Barbarin, 1986; Hirth and Tullis, 1992; Law, 2014; Passchier and Trouw, 2005), is in line with a syntectonic emplacement of plutons but also with deformation of partially molten rocks in the course of their crystallization.

Additional evidences in favor of a diatexite include the presence of numerous rafts and enclaves of migmatitic amphibolite, micaschist and paragneiss showing diffuse contacts with the granodioritic gneiss host, as well as occurrence of leucosome veins in textural continuity with its groundmass. This also means that metamorphic conditions reached higher supra solidus temperatures (up to 850 °C, Fig. 14a) than the ones indicated by metamorphic assemblages of paragneiss (650–680 °C), to achieve the voluminous melt production (~30 %) needed to constitute diatexites (Brown, 1994; Diener et al., 2014; Schwindinger et al., 2019; Vielzeuf and Holloway, 1988; White et al., 2003). The heterogeneous microstructure/texture of this groundmass, and in particular quartz and/or feldspar pockets coating phenocrysts (Fig. 4b, Fig. 9), is typical of crystallization of an interstitial melt (Hasalová et al., 2015; Holness et al., 2011; Sawyer, 2010; Schulmann et al., 2009; Závada et al., 2018). The formation of such diatexites implies accumulation of melt in the partial-melting zone, which signifies an inefficient migration of the newly-formed melt away from the source (Sawyer, 1991; Vanderhaeghe, 2009). In this case, the inherited metamorphic structure is susceptible to be blurred or even erased during flow of this mixture of crystals and melt (Burg and Vanderhaeghe, 1993; Schulmann et al., 2009; Závada et al., 2018).

In the neighboring district of Téhini (south continuity of the Mangodara district) a biotite granodioritic gneiss locally migmatitic, designated as "Comoé type gneiss" (Hirdes et al., 1996), is dated at 2152 ± 2 Ma by U-Pb method in zircon, and 2100 ± 3 Ma by U-Pb method in titanite. The latter was interpreted as a resetting by regional metamorphism, on the basis of low Th/U in titanite (~0.2). In agreement with the diatexite model of the granodioritic gneiss, the zircon age concomitant with the ME1 might record changes in the chemical composition of the melt during the diatexite genesis (Kelsey et al., 2008; Kelsey and Powell, 2011; Yakymchuk and Brown, 2014) instead of magmatic crystallization.

The magmatic texture of the tonalitic-trondhjemitic gneiss homogeneous at a regional scale, might either reflect a plutonic origin or a zone of accumulation-aggregation of magmatic and residual minerals within the partially molten zone. The discordance between the tonalitic-trondhjemitic gneiss relative to the foliation of the granodioritic gneiss, though, is in favor of an intrusive contact. As a plagioclase-rich mush, the emplacement of the tonalitic-trondhjemitic cannot be achieved by melt alimentation through channels, but instead by ascent of the buoyant plagioclase-rich mush in the mantling gneiss, provoking deflection of the structure of the granodioritic gneiss. The formation of the dome is attributed to the development of a gravitational instability that predominated over the regional NE-SW deformation pattern. Crystallization of the titanite-allanite pegmatite dated at 2094.3 ± 8.8 Ma by U-Pb on zircon, implies that the tonalitic-trondhjemitic gneiss crystallization occurred approximately at this time, which corresponds to the end of ME2 defined by Baratoux et al. (2011). The Mangodara dome formed also during this period during progressive D1-D2 deformation described by Chardon et al. (2020), by local deflection induced by the ascent of the plagioclase-rich mush.

The occurrence in tonalitic-trondhjemitic gneiss of tonalitic veins hosting poikilitic hornblende-biotite implies that its segregation occurred in the presence of H_2O, which favors a melting reaction with formation of hydrous peritectic phases (Berger et al., 2008; Sawyer, 2010; Tafur and Diener, 2020; Weinberg, 1999; Weinberg and Hasalová, 2015). In the context of the Mangodara district, H_2O-saturation more likely represents late saturation induced by cooling of the tonalitic-trondhjemitic gneiss (Annen and Burgisser, 2020; Clemens and Stevens, 2015; Clemens and Watkins, 2001), rather than dehydrating anatectic reactions (Sawyer, 2010) or dewatering of the lower crust caused by a flux of mantle-derived CO_2-rich fluids (Cuney and Barbey, 2014; Touret and Hartel, 1990; Touret and Huizenga, 2011; Touret and Nijland, 2013).

The pressure of 7 kbar inferred from the thermodynamic modelling of the migmatitic paragneiss is interpreted to record the depth of the onset of partial melting, whereas the pressure of 4 to 6 kbar recorded by the granodioritic and tonalitic gneisses is considered to correspond to the depth of crystallization. The difference of 1 to 3 kbar between partial melting and crystallization is consistent with regional exhumation of about 3 to 9 km between these two processes as well as with upward motion of the tonalitic gneiss relative to the granodioritic gneiss during this period.

Ages of ca. 2094 Ma obtained in rocks from the core of the dome appear to be older than the ages of 2055 and 2041 Ma obtained in the mantling units. The similarity in U-Pb zircon and apatite ages obtained in the core of the dome is consistent with rapid cooling following crystallization of the tonalitic gneiss and enclosing pegmatites. However, younging of apatite U-Pb ages upsection is difficult to reconcile with a simple scenario of crustal cooling after exhumation, which would yield the opposite younging trend, namely downsection. This discrepancy might be tentatively attributed to the difference in the size of the apatite grain (Cherniak et al., 1991; Dodson, 1973) that are significantly larger in samples from the core of the dome (~200 µm) compared to the ones from the mantle of the dome (~300 µm). However, such reasoning, if correct in theory, cannot be demonstrated with the geochronological data as all ages are overlapping within error margins.

5.2.2. Geochemical constraints on the protolith of the gneisses

Paragneiss as sources of the granodioritic gneiss

Generation of a K-rich melt is expected in case of partial melting reactions involving dehydration of K-bearing minerals such as micas (Gardien et al., 1995; Le Breton and Thompson, 1988; Montel and Vielzeuf, 1997; Patiño Douce and Beard, 1995; Rapp and Watson, 1995; Thompson, 1982; Vielzeuf and Holloway, 1988; Vielzeuf and Montel, 1994; Wyllie and Wolf, 1993). In the studied area, the most mica-rich lithology corresponds to the paragneiss, which is thus a good candidate to generate a K-rich melt. Alternatively, a K-rich-melt might reflect the presence of residual plagioclase in the partially molten rock, which increases the K_2O/Na_2O ratio in the anatectic melt comparatively to the source (Laurent et al., 2014). This implies a fractionation of K_2O/Na_2O ratio by residual plagioclase (stable for almost $P < 15$ kbar) with low degree of partial melting to prevent entrainment of plagioclase. The latter hypothesis is unsuited with the high degree of partial melting suggested by the field observations reported in the previous section.

Further exploring the scenario of an origin of the K-rich series by partial melting of paragneiss, it appears that the granodioritic gneiss shows a slight depletion in LILE (Rb, Cs, see Fig. 17b) compared to its alleged protolith. Reaching such a composition requires the contribution of a LILE-poor source, such as the amphibolite and micaschist, to dilute LILE concentration in the granodioritic anatectic melt. On the other hand, the absence of Nb and Ta fractionation between the granodioritic gneiss and the amphibolite, micaschist and paragneiss, suggests that partial melting occurred at a pressure inferior to the stability domain of rutile (< 10–15 kbar, Diener et al., 2007; Foley et al., 2002; Green et al., 2016; Moyen and Stevens, 2006). The slight enrichment in LREE of the granodioritic gneiss relative to the amphibolite, micaschist and paragneiss, signs for an incompatible behavior of LREE that could be highly soluble during partial melting. Further, the depletion in HREE and Y, implies a fractionation by REE-bearing minerals such as garnet or amphibole, which is also consistent with the low Fe, Mg, and Ti content of the granodioritic gneiss compared to amphibolite, micaschist and paragneiss. This proposition is further supported by the presence of peritectic garnet in the migmatitic paragneiss (Fig. 7d, e and f), and of hornblende-bearing leucosomes in the amphibolite (Fig. 5c). Altogether, the weak fractionation of REE, Nb, Ta, and the typical high Cr, Ba and Sr content (e.g., 134–227 Cr ppm in granodioritic gneiss, 32–189 ppm in K-rich plutonic rocks) suggests that the granodioritic gneiss resulted from high degree partial melting of a mixed source that would include amphibolite (1129 ppm Cr), micaschist and paragneiss (217 ppm Cr), whose resisters and/or restites are observed as rafts in the granodioritic diatexite. Peritectic hornblende and garnet fractionated ferromagnesian elements, HREE and Y.

Amphibolites as sources of the tonalitic-trondhjemitic gneiss

In general, tonalitic and trondhjemitic magmas are considered to be generated by partial melting of an hydrated mafic source under pressures higher than 10 kbar, required to destabilize plagioclase (Atherton and Petford, 1993; Barker, 1979; Barker and Arth, 1976; Drummond et al., 1996; Moyen et al., 2009; Patiño Douce and Beard, 1995; Peacock et al., 1994; Petford and Atherton, 1996; Rapp et al., 1991; Rapp and Watson, 1995; Rushmer, 1991; Skjerlie and Patiño Douce, 2002; Winther and Newton, 1991; Wyllie and Wolf, 1993). The tonalitic-trondhjemitic gneiss is characterized by relatively low content in Mg (0.38–0.46 Mg#) and transition metals (Cr, Cu, Ni) that allow to refute an origin by direct partial melting of a mantle source or a mantle contamination. Alternatively, the tonalitic-trondhjemitic assemblage could be generated by partial melting of Birimian amphibolites and mafic schists. The lack of negative Eu anomaly in the gneiss implies that fractional crystallization of plagioclase in equilibrium with a melt is not involved in its genesis. Laurent et al. (2020) proposed that trondhjemitic magmas could be formed by plagioclase accumulation and amphibole fractionation from a tonalitic-granodioritic parental melt (Fig. 18c). However, in Mangodara, the structural position of the tonalitic-trondhjemitic gneiss under the granodioritic gneiss is not consistent with this such a scenario, as a fractionated magma tends to segregate toward the upper part of the partially molten zone or to migrate out of the partially molten zone to intrude the upper crust (Hildreth, 2004; Jackson et al., 2018, 2003; Vanderhaeghe, 2009). A compliant model assimilates the tonalitic-trondhjemitic gneiss to a tonalitic melt coming from a deeper zone of partial melting affecting a predominantly mafic protolith (such as Birimian amphibolites) (Ilboudo et al., 2021), which evolves into a mush composed of clustered residual plagioclase. Partial melting of amphibolite produces a residue dominated in composition by plagioclase and pyroxene (Fig. 14b and d). The absence in tonalitic-trondhjemitic gneiss of products of dehydration melting reactions in the source (e.g. garnet, pyroxene) as well as the scarcity of rafts in textural continuity with the gneiss is consistent with a migration of the tonalitic-trondhjemitic magma away from its source, leaving at least part of its residual solid at a lower structural level.

When compared to the amphibolite and micaschist, the tonalite-trondhjemitic gneiss is enriched in LILE (K, Cs, Rb), and W, but depleted in HFSE such as Nb, Ta, Ti, Y and HREE. Two possible processes can explain these depletions:

(1) Some elements are fractionated by residual minerals in restites of the partially melted amphibolites and schists, or by early magmatic minerals during the rise of the parental melt. Specifically, this implies the segregation of Nb, Ta, Ti and HREE by rutile at $P > 15$ kbar (Drummond et al., 1996; Foley et al., 2002; Hoffmann et al., 2011; Moyen and Stevens, 2006), Y and HREE by garnet at $P > 10$ kbar (Drummond et al., 1996; Hoffmann et al., 2011; Moyen and Stevens, 2006), LREE by early magmatic allanite, titanite and phosphates (Brooks et al., 1981; Green and Pearson, 1987, 1986; Hermann, 2002; Solgadi et al., 2007; Tiepolo et al., 2002). Moreover, amphibole extraction in the

parental melt can enhance depletion in REE and increase of the La/Yb and Sr/Y ratios in the tonalite-trondhjemite (Liou and Guo, 2019; Reichardt and Weinberg, 2012).

(2) Following the model of Laurent et al. (2020), incompatible LILE and HFSE are entrained in the residual liquid during crystallization of the parental melt of the tonalitic-trondhjemitic gneiss. The liquid migrates upward and emplaces at an upper level of the crust to form granitic plutons or silicic volcanic rocks (Laurent et al., 2020).

Whether it results from high pressure melting of amphibolites, or fractional crystallization of a parental tonalitic melt, the source of the tonalitic-trondhjemitic gneiss is located in structural levels below the granodioritic gneiss (Fig. 19), which is in agreement with the pressure-related classification of TTG proposed by Moyen, (2011). As mafic composition of the source is more likely to result in tonalitic magmas, the protolith should be dominated by Birimian amphibolites over metasediments (Fig. 20). Partial melting predominantly of a mafic component is consistent with the affinity of the tonalitic magma with the plagioclase-rich Na-rich series. According to this scenario, REE and HFSE fractionation in the tonalitic-trondhjemitic gneiss would be achieved by clustering of residual minerals or fractional crystallization.

5.3. Petrogenesis of the K-rich and Na-rich magmatic series

K-rich plutonic rocks

The monzogabbro, hornblende-biotite granodiorite and GG granitoids, which display a mineralogy and geochemical signature similar to those of the granodioritic gneiss, are interpreted to represent differentiated terms of the K-rich magmatic series. Their structural position in diffused but locally cross-cutting contact with the granodioritic gneiss further suggests that they correspond to magmas that segregated *in-situ* during deformation (Fig. 19 and Fig. 20).

The hornblende-biotite granodiorite is edged by shear zones that probably controlled melt migration (Archanjo et al., 1999; de Saint Blanquat et al., 2011, 1998; Gleizes et al., 1997; Weinberg et al., 2004), and permit melt accumulation in a lower part of the granodioritic gneiss (Fig. 19). Megacrystic plagioclase in this granodiorite are witnesses of an extended magmatic growth as in a magmatic chamber.

In the eastern part of the district, the contact of GG-granitoids with granodioritic gneiss is marked by rhythmic layering that might correspond to melt percolation within the fabric of the granodioritic gneiss (Barbey, 2009; Clemens and Stevens, 2016; Vanderhaeghe, 2009; Weinberg, 1999). In the neighboring Téhini District, the "Bavé type" biotite granodiorite (2137 +9/-7 Ma by U-Pb method on zircon) has been interpreted as the product of partial melting of the "Comoé type" granodioritic gneiss (Hirdes et al., 1996). From our point of view, this granodiorite might be the product of melt accumulation within the granodioritic diatexite, which crystallized at the end of the ME1.

The monzogabbro could result from accumulation of hornblende separated from a granodioritic assemblage. A similar scenario has been proposed for hornblendite in Xuanmenzi-Gualanyu region (Neoarchean, North China Craton), resulting in decreased Sr/Y and La/Yb ratios (Liou and Guo, 2019).

Na-rich plutonic rocks

The plagioclase-rich trondhjemite, which has geochemical features similar to the tonalitic-trondhjemitic gneiss (K-poor, low HFSE and REE), could have resulted from accumulation of plagioclase floating at the roof of the tonalitic-trondhjemitic gneiss. The peraluminous composition of the two-mica tonalite can be attained by fractionation of biotite and hornblende in the plagioclase-rich melt (Chappell et al., 2012). Moreover, the composition of the tonalitic-trondhjemitic gneiss, which is intermediate between the trondhjemite and the two-mica tonalite is consistent with this proposition (Fig. 18d and e). Its position occupying the roof of tonalitic-trondhjemitic gneiss in perfect concordance with its southern margin, corroborates an origin as a melt extracted from the tonalitic-trondhjemitic gneiss (Fig. 19). The lower proportion of plagioclase in this melt stands with a relative increase of K, stabilizing micas instead of amphibole, whereas the depleted REE and HFSE signatures are inherited from the tonalitic-trondhjemitic gneiss (Fig. 20).

5.4. Petrogenesis of the rare metal-bearing pegmatites

Textural continuity of titanite-allanite pegmatites with veins concordant to the foliation of the tonalitic-trondhjemitic gneiss, suggests that the pegmatite-forming magma segregated from the tonalitic-trondhjemitic mush itself. Sharp contacts of discordant pegmatite veins observed in other places indicate that the pegmatite-forming magma migrated when the tonalitic-trondhjemitic gneiss cooled below the ductile-to-fragile transition, which also fulfills the undercooling conditions needed for nucleation of pegmatitic crystals (London, 1989, 2009, 2014). Accordingly, titanite-allanite pegmatites are interpreted as the late residual melt enriched in volatile elements segregated during crystallization of the tonalitic magma (Fig. 19). Its higher K/Rb and Ca/Cs ratios, and lower contents in Nb, Ta and REE then other pegmatites show that the titanite-allanite is the least differentiated of the Mangodara pegmatite types.

Apatite-zircon pegmatites are lithologically discriminated from the titanite-allanite type only by their occurrence in granodioritic gneiss and absence of allanite and epidote. Therefore, the two types could be cogenetic and derived from a single source, or alternatively, the apatite-zircon type could represent the residual melt after crystallization of the titanite-allanite pegmatites. An origin by fractional crystallization is further suggested by the relative LILE and REE enrichment in apatite-zircon pegmatites compared to the titanite-allanite type, which reflects a differentiation trend. However, Eu was segregated preferentially to other REE in titanite-allanite pegmatite, as indicated by its positive anomaly. This behavior is probably enhanced by the presence of Eu-bearing minerals in the titanite-allanite pegmatite (allanite, apatite), resulting subsequently in the relative depletion of Eu apatite-zircon pegmatite.

Textural continuity of garnet-columbite pegmatites (Li, Nb enriched) with concordant and discordant leucosome veins of the migmatitic paragneiss is consistent with segregation of the pegmatite-forming magma from the partially molten paragneiss. Their transposition into the foliation of the paragneiss indicates that this segregation is coeval with deformation. The high differentiation degree of garnet-columbite pegmatites compared to other plutonic rocks in the Mangodara district is proposed to correspond to the segregation of an anatectic melt seeping from partially molten paragneiss (Fig. 19).

The textural continuity of garnet-REE pegmatite (Ti, Y, HREE enriched) with concordant leucosome veins of the granodioritic gneiss points to an origin by melt segregation during crystallization of the partially molten granodioritic gneiss (Fig. 19). Its higher content in U, Th and REE compared to other pegmatites suggest a different degree of differentiation marked by HFSE enrichment, which is mostly achieved in peralkaline to metaluminous differentiated melt (Černý et al., 2005; Černý and Ercit, 2005; Linnen and Cuney, 2005).

Uranium-lead age of apatite record the closure of U-Pb isotopic system, which occurs at 450-600 °C for grain size < 1 mm but varies with the grain size and cooling rate (Cherniak et al., 1991; Dodson, 1973). Uncertainties on apatite ages of gneisses and apatite-zircon pegmatite span large period which cover the ME2 and ends at 2000 Ma. These data involve a regional cooling occurring after 2100 Ma. This reinforces the idea that a temperature was maintained above 500 °C during at least 50 Ma, which fits a long-lasting tectono-thermal event (Guergouz et al., 2018; Turlin et al., 2018; Vanderhaeghe et al., 2019; Vauchez et al., 2019) encompassing MP-HT metamorphism, diatexite formation, melt accumulation and late segregation of pegmatite-forming melt.

In short, the continuous network of granitic veins and pegmatites concordant to discordant relative to the foliation of their host gneisses and their magmatic texture plead for a pegmatite formation by syntectonic melt segregation (Brown, 2005, 1994; Burg and Vanderhaeghe, 1993; Sawyer, 2001, 1999; Vanderhaeghe et al., 1999; Vanderhaeghe, 2001; Weinberg, 2006; Wickham, 1987), (Fig. 19 and Fig. 20). The segregated pegmatite-forming low-viscosity melt is transposed into the flattening plane (Brown et al., 1995; Stevenson, 1989; Vanderhaeghe et al., 1999) but also in low-pressure sites induced by ductile deformation (Brown et al., 1995; Robin, 1979; Stevenson, 1989; Van der Molen, 1985; Van der Molen and Paterson, 1979; Vanderhaeghe et al., 1999). After crystallization, the pegmatites become more competent than the host gneisses and are folded and boudinaged with cuspate interfaces without losing their internal texture (Fig. 11e) (Alsop et al., 2021; Bons et al., 2004; Butler and Torvela, 2018; Druguet, 2019).

6. Conclusions

Field observations, combined with structural, petrological and geochemical data from rare metal-bearing pegmatites of the Mangodara district indicate that they derived from their gneiss-granitoid hosts, with an input from the rafts of amphibolite, schist and paragneiss enclosed in the latter. Titanite-allanite-bearing and apatite-zircon-bearing pegmatites are in textural continuity with leucosome veins, themselves concordant with the foliation of the granodioritic and tonalitic gneisses. These pegmatites are interpreted as originating from syntectonic melt segregation from a partially molten rock or crystalline mush. On the other hand, the garnet-columbite-bearing and garnet-REE-bearing pegmatites are inferred to derive, respectively, from partial melting of paragneiss and segregation of melt within the granodioritic gneiss.

PT conditions of partial melting are constrained by thermodynamic modelling of the migmatitic paragneiss, yielding 650-700 °C for 7 kbar, and of the migmatitic amphibolite with a temperature over 750 °C. In this context of MP-HT metamorphism, generation of the granodioritic gneiss by further partial melting of the Birimian series, required a temperature higher than 850 °C to reach the biotite-out isograd and a melt fraction of about 30 % associated with the metatexite/diatexite transition. The low degree of fractionation of HFSE and REE between paragneiss relative to granodioritic gneiss supports such a high degree of partial melting without migration of magma out of the zone of partial melting. A dominant proportion of paragneiss is required in the protolith of the granodioritic gneiss to account for its high-K content, but its weak depletion in LILE is best explained by a minor contribution from the amphibolite and micaschist.

The formation of the Na-rich and K-rich magmatic series of the Mangodara district is attributed to partial melting at different pressure (7 to 10 kbar) and in various proportions of amphibolite and paragneiss of the Birimian series followed by melt segregation and/or clustering/accumulation of residual/magmatic crystals. Depletion of REE and HFSE in members of the Na-rich series are explained by plagioclase and amphibole fractionation from a granodioritic/tonalitic parental magma or by clustering of residual plagioclase from an anatectic melt, with separation from a garnet-pyroxene-allanite-titanite-bearing residue.

Crystallization of titanite-allanite pegmatite is constrained at 2094.3 ± 8.8 Ma by U-Pb on zircon, whereas cooling below ca. 500 °C is documented by apatite cooling ages of 2094 ± 21 Ma for the granodioritic gneiss and 2055 ± 20 Ma for an apatite-zircon pegmatite.

These data favor a segregation model for rare metal-bearing pegmatites of the Mangodara district. This took place within the partially molten root of the Eburnean orogenic crust during formation, between transcurrent shear zones, of a crustal-scale dome cored by a plagioclase-dominated crystal mush and mantled by a heterogeneous diatexite of granodioritic composition.

Acknowledgements

This work is developed from a collaboration between the University of Toulouse 3 Paul Sabatier (France) and the University Joseph Ki-Zerbo (Ouagadougou, Burkina Faso). This study benefited from funds provided by the West African Exploration Initiative project (WAXI; AMIRA P934B) and was supported by the French Institut de Recherche pour le Développement (IRD) and the French Embassy in Burkina Faso. We are grateful to the Bureau des Mines et de la Géologie du Burkina (BUMIGEB) for logistic support, field work assistance, and providing data and other information on the study region. We also thank the GeOHeLiS analytical platform (University of Rennes 1) for the LA-ICP-MS analyses on zircon and apatite. Anonymous reviewers provided much appreciated insights that improved the final manuscript.

References

Abouchami, W., Boher, M., Michard, A., Albarede, F., 1990. A major 2.1 Ga event of mafic magmatism in west Africa: An Early stage of crustal accretion. J. Geophys. Res. Solid Earth 95, 17605–17629. https://doi.org/10.1029/JB095iB11p17605

Adams, S., 2013. Rare metals mineralization of Winneba-Mankoadze pegmatites, South Western Ghana.

Allou, A.B., 2005. Facteurs, paramètres, dynamique de distribution et genèse des dépôts de columbo-tantalite d'Issia, centre-ouest de la Côte d'Ivoire. Université du Québec à Chicoutimi.

Alsop, G.I., Strachan, R.A., Holdsworth, R.E., Burns, I.M., 2021. Geometry of folded and boudinaged pegmatite veins emplaced within a strike-slip shear zone: A case study from the Caledonian orogen, northern Scotland. J. Struct. Geol. 142, 104233. https://doi.org/10.1016/j.jsg.2020.104233

Annen, C., Burgisser, A., 2020. Modeling water exsolution from a growing and solidifying felsic magma body. Lithos 105799. https://doi.org/10.1016/j.lithos.2020.105799

Anum, S., Sakyi, P.A., Su, B.-X., Nude, P.M., Nyame, F., Asiedu, D., Kwayisi, D., 2015. Geochemistry and geochronology of granitoids in the Kibi-Asamankese area of the Kibi-Winneba volcanic belt, southern Ghana. J. Afr. Earth Sci. 102, 166–179. https://doi.org/10.1016/j.jafrearsci.2014.11.007

Archanjo, C.J., da Silva, E.R., Caby, R., 1999. Magnetic fabric and pluton emplacement in a transpressive shear zone system: the Itaporanga porphyritic granitic pluton (northeast Brazil). Tectonophysics 312, 331–345. https://doi.org/10.1016/S0040-1951(99)00176-6

Arnould, M., 1961. Étude géologique des migmatites et des granites précambriens du nord-est de la Côte d'Ivoire et de la Haute-Volta méridionale. Ht.-Volta Méridionale BRGM Mém. N 3.

Asiedu, D.K., Dampare, S.B., Sakyi, P.A., Banoeng-Yakubo, B., Osae, S., Nyarko, B.J.B., Manu, J., 2004. Geochemistry of Paleoproterozoic metasedimentary rocks from the Birim diamondiferous field, southern Ghana: Implications for provenance and crustal evolution at the Archean-Proterozoic boundary. Geochem. J. 38, 215–228. https://doi.org/10.2343/geochemj.38.215

Atherton, M.P., Petford, N., 1993. Generation of sodium-rich magmas from newly underplated basaltic crust. Nature 362, 144.

Baldwin, J., Powell, R., Brown, M., Moraes, R., Fuck, R., 2005. Modelling of mineral equilibria in ultrahigh-temperature metamorphic rocks from the Anápolis–Itauçu Complex, central Brazil. J. Metamorph. Geol. 23, 511–531.

Ballouard, C., Poujol, M., Boulvais, P., Branquet, Y., Tartèse, R., Vigneresse, J.-L., 2016. Nb-Ta fractionation in peraluminous granites: A marker of the magmatic-hydrothermal transition. Geology 44, 231–234.

Baratoux, L., Metelka, V., Naba, S., Jessell, M.W., Grégoire, M., Ganne, J., 2011. Juvenile Paleoproterozoic crust evolution during the Eburnean orogeny (∼ 2.2–2.0 Ga), western Burkina Faso. Precambrian Res. 191, 18–45.

Barbey, P., 2009. Layering and schlieren in granitoids: A record of interactions between magma emplacement, crystallization and deformation in growing plutons (The André Dumont medallist lecture). Geol. Belg.

Barker, F., 1979. Chapter 1 - Trondhjemite: Definition, Environment and Hypotheses of Origin, in: Barker, F. (Ed.), Developments in Petrology, Trondhjemites, Dacites, and Related Rocks. Elsevier, pp. 1–12. https://doi.org/10.1016/B978-0-444-41765-7.50006-X

Barker, F., Arth, J.G., 1976. Generation of trondhjemitic-tonalitic liquids and Archean bimodal trondhjemite-basalt suites. Geology 4, 596–600.

Bau, M., 1996. Controls on the fractionation of isovalent trace elements in magmatic and aqueous systems: evidence from Y/Ho, Zr/Hf, and lanthanide tetrad effect. Contrib. Mineral. Petrol. 123, 323–333. https://doi.org/10.1007/s004100050159

Berger, A., Burri, T., Alt-Epping, P., Engi, M., 2008. Tectonically controlled fluid flow and water-assisted melting in the middle crust: an example from the Central Alps. Lithos 102, 598–615.

Béziat, D., Bourges, F., Debat, P., Lompo, M., Martin, F., Tollon, F., 2000. A Paleoproterozoic ultramafic-mafic assemblage and associated volcanic rocks of the Boromo greenstone belt: fractionates originating from island-arc volcanic activity in the West African craton. Precambrian Res. 101, 25–47.

Block, S., Baratoux, L., Zeh, A., Laurent, O., Bruguier, O., Jessell, M.W., Ailleres, L., Sagna, R., Parra-Avila, L.A., Bosch, D., 2016a. Paleoproterozoic juvenile crust formation and stabilisation in the south-eastern West African Craton (Ghana); New insights from U-Pb-Hf zircon data and geochemistry. Precambrian Res. 287, 1–30.

Block, S., Ganne, J., Baratoux, L., Zeh, A., Parra-Avila, L., Jessell, M.W., Ailleres, L., Siebenaller, L., 2015. Petrological and geochronological constraints on lower crust exhumation during Paleoproterozoic (Eburnean) orogeny, NW Ghana, West African Craton. J. Metamorph. Geol. 33, 463–494.

Block, S., Jessell, M.W., Aillères, L., Baratoux, L., Bruguier, O., Zeh, A., Bosch, D., Caby, R., Mensah, E., 2016b. Lower crust exhumation during Paleoproterozoic (Eburnean) orogeny, NW Ghana, West African Craton: Interplay of coeval contractional deformation and extensional gravitational collapse. Precambrian Res. 274, 82–109.

Boher, M., Abouchami, W., Michard, A., Albarede, F., Arndt, N.T., 1992. Crustal growth in West Africa at 2.1 Ga. J. Geophys. Res. Solid Earth 97, 345–369. https://doi.org/10.1029/91JB01640

Bohlen, S.R., Wall, V.J., Boettcher, A.L., 1983. Experimental investigations and geological applications of equilibria in the system FeO-TiO2-Al2O3-SiO2-H2O. Am. Mineral. 68, 1049–1058.

Bons, P.D., Druguet, E., Hamann, I., Carreras, J., Passchier, C.W., 2004. Apparent boudinage in dykes. J. Struct. Geol. 26, 625–636. https://doi.org/10.1016/j.jsg.2003.11.009

Brooks, C., Henderson, P., Rønsbo, J., 1981. Rare-earth partition between allanite and glass in the obsidian of Sandy Braes, Northern Ireland. Mineral. Mag. 44, 157–160.

Brown, M., 2005. The mechanism of melt extraction from lower continental crust of orogens. Trans R. Soc Edinb. Earth Sci 95, 35–48.

Brown, M., 1994. The generation, segregation, ascent and emplacement of granite magma: the migmatite-to-crustally-derived granite connection in thickened orogens. Earth-Sci. Rev. 36, 83–130.

Brown, M., 1973. The definition of metatexis, diatexis and migmatite. Proc. Geol. Assoc. 84, 371-IN2. https://doi.org/10.1016/S0016-7878(73)80021-5

Brown, M., Averkin, Y.A., McLellan, E.L., Sawyer, E.W., 1995. Melt segregation in migmatites. J. Geophys. Res. Solid Earth 100, 15655–15679.

Burg, J.-P., Vanderhaeghe, O., 1993. Structures and way-up criteria in migmatites, with application to the Velay dome (French Massif Central). J. Struct. Geol. 15, 1293–1301. https://doi.org/10.1016/0191-8141(93)90103-H

Butler, R.W.H., Torvela, T., 2018. The competition between rates of deformation and solidification in syn-kinematic granitic intrusions: Resolving the pegmatite paradox. J. Struct. Geol. 117, 1–13. https://doi.org/10.1016/j.jsg.2018.08.013

Caen-Vachette, M., 1988. Le craton ouest-africain et le bouclier guyanais: un seul craton au Protérozoïque inférieur? J. Afr. Earth Sci. Middle East 7, 479–488.

Castaing, C., Billa, M., Milési, J., Thiéblemont, D., Le Metour, J., Egal, E., Donzeau, M., Guerrot, C., Cocherie, A., Chevremont, P., 2003. Notice explicative de la carte géologique et minière du Burkina Faso à 1/1 000 000. BRGM BUMIGEB 147.

Cavalcante, G.C.G., Viegas, G., Archanjo, C.J., da Silva, M.E., 2016. The influence of partial melting and melt migration on the rheology of the continental crust. J. Geodyn., Fluids in crustal deformation : fluid flow, fluid-rock interactions, rheology, melting and resources 101, 186–199. https://doi.org/10.1016/j.jog.2016.06.002

Černý, P., 1991a. Rare-element Granitic Pegmatites. Part I: Anatomy and Internal Evolution of Pegmatitic Deposits. Geosci. Can. 49–67.

Černý, P., 1991b. Rare-element Granitic Pegmatites. Part II: Regional to Global Environments and Petrogenesis. Geosci. Can.

Černý, P., Blevin, P.L., Cuney, M., London, D., 2005. Granite-related ore deposits.

Černý, P., Ercit, T.S., 2005. The classification of granitic pegmatites revisited. Can. Mineral. 43, 2005–2026.

Černý, P., Meintzer, R.E., Anderson, A.J., 1985. Extreme fractionation in rare-element granitic pegmatites; selected examples of data and mechanisms. Can. Mineral. 23, 381–421.

Chalokwu, C.I., Ghazi, M.A., Foord, E.E., 1997. Geochemical characteristics and K-Ar ages of rare-metal bearing pegmatites from the Birimian of southeastern Ghana. J. Afr. Earth Sci. 24, 1–9. https://doi.org/10.1016/S0899-5362(97)00022-5

Chappell, B.W., Bryant, C.J., Wyborn, D., 2012. Peraluminous I-type granites. Lithos, Seventh Hutton Symposium on Granites and Related Rocks 153, 142–153. https://doi.org/10.1016/j.lithos.2012.07.008

Chardon, D., Bamba, O., Traoré, K., 2020. Eburnean deformation pattern of Burkina Faso and the tectonic significance of shear zones in the West African craton. BSGF - Earth Sci. Bull. 191, 2. https://doi.org/10.1051/bsgf/2020001

Cherniak, D.J., Lanford, W.A., Ryerson, F., 1991. Lead diffusion in apatite and zircon using ion implantation and Rutherford backscattering techniques. Geochim. Cosmochim. Acta 55, 1663–1673.

Clemens, J.D., Stevens, G., 2016. Melt segregation and magma interactions during crustal melting: Breaking out of the matrix. Earth-Sci. Rev. 160, 333–349. https://doi.org/10.1016/j.earscirev.2016.07.012

Clemens, J.D., Stevens, G., 2015. Comment on ‘Water-fluxed melting of the continental crust: A review’ by R.F. Weinberg and P. Hasalová. Lithos 234–235, 100–101. https://doi.org/10.1016/j.lithos.2015.06.032

Clemens, J.D., Watkins, J.M., 2001. The fluid regime of high-temperature metamorphism during granitoid magma genesis. Contrib. Mineral. Petrol. 140, 600–606.

Coggon, R., Holland, T., 2002. Mixing properties of phengitic micas and revised garnet-phengite thermobarometers. J. Metamorph. Geol. 20, 683–696.

Cox, K.G., Bell, J.D., Pankhurst, R.J., 1979. The Interpretation of Igneous Rocks. Springer Netherlands, Dordrecht. https://doi.org/10.1007/978-94-017-3373-1

Cuney, M., Barbey, P., 2014. Uranium, rare metals, and granulite-facies metamorphism. Geosci. Front., SPECIAL ISSUE: The role of fluids in the lower crust and upper mantle: A tribute to Jacques Touret 5, 729–745. https://doi.org/10.1016/j.gsf.2014.03.011

de Capitani, C., Brown, T.H., 1987. The computation of chemical equilibrium in complex systems containing non-ideal solutions. Geochim. Cosmochim. Acta 51, 2639–2652.

de Capitani, C., Petrakakis, K., 2010. The computation of equilibrium assemblage diagrams with Theriak/Domino software. Am. Mineral. 95, 1006–1016.

De Kock, G., Armstrong, R., Siegfried, H., Thomas, E., 2011. Geochronology of the Birim Supergroup of the West African craton in the Wa-Bolé region of west-central Ghana: Implications for the stratigraphic framework. J. Afr. Earth Sci. 59, 1–40.

de Saint Blanquat, M., Horsman, E., Habert, G., Morgan, S., Vanderhaeghe, O., Law, R., Tikoff, B., 2011. Multiscale magmatic cyclicity, duration of pluton construction, and the paradoxical relationship between tectonism and plutonism in continental arcs. Tectonophysics 500, 20–33.

de Saint Blanquat, M., Tikoff, B., Teyssier, C., Vigneresse, J.L., 1998. Transpressional kinematics and magmatic arcs. Geol. Soc. Lond. Spec. Publ. 135, 327–340. https://doi.org/10.1144/GSL.SP.1998.135.01.21

Debat, P., Nikiéma, S., Mercier, A., Lompo, M., Béziat, D., Bourges, F., Roddaz, M., Salvi, S., Tollon, F., Wenmenga, U., 2003. A new metamorphic constraint for the Eburnean orogeny from Paleoproterozoic formations of the Man shield (Aribinda and Tampelga countries, Burkina Faso). Precambrian Res. 123, 47–65. https://doi.org/10.1016/S0301-9268(03)00046-9

Delor, C., Egal, E., Lafon, J.-M., Cocherie, A., Guerrot, C., Rossi, P., Truffert, C., Théveniaut, H., Phillips, D., Avelar, V.G., 2003. Transamazonian crustal growth and reworking as revealed by the 1:500,000-scale geological map of French Guiana (2nd edition). Géologie Fr. 5–57.

Diener, J.F.A., Powell, R., White, R.W., Holland, T.J.B., 2007. A new thermodynamic model for clino- and orthoamphiboles in the system Na2O–CaO–FeO–MgO–Al2O3–SiO2–H2O–O. J. Metamorph. Geol. 25, 631–656. https://doi.org/10.1111/j.1525-1314.2007.00720.x

Diener, J.F.A., White, R.W., Hudson, T.J.M., 2014. Melt production, redistribution and accumulation in mid-crustal source rocks, with implications for crustal-scale melt transfer. Lithos 200–201, 212–225. https://doi.org/10.1016/j.lithos.2014.04.021

Dodson, M.H., 1973. Closure temperature in cooling geochronological and petrological systems. Contrib. Mineral. Petrol. 40, 259–274.

Doumbia, S., Pouclet, A., Kouamelan, A., Peucat, J., Vidal, M., Delor, C., 1998. Petrogenesis of juvenile-type Birimian (Paleoproterozoic) granitoids in Central Côte-d'Ivoire, West Africa: geochemistry and geochronology. Precambrian Res. 87, 33–63.

Druguet, E., 2019. Deciphering the presence of axial-planar veins in tectonites. Geosci. Front. 10, 2101–2115. https://doi.org/10.1016/j.gsf.2019.02.005

Drummond, M.S., Defant, M.J., Kepezhinskas, P.K., 1996. Petrogenesis of slab-derived trondhjemite–tonalite–dacite/adakite magmas. Earth Environ. Sci. Trans. R. Soc. Edinb. 87, 205–215. https://doi.org/10.1017/S0263593300006611

Drury, M.R., Urai, J.L., 1990. Deformation-related recrystallization processes. Tectonophysics 172, 235–253. https://doi.org/10.1016/0040-1951(90)90033-5

Ducellier, J., 1963. Contribution à l'étude des formations cristallines et métamorphiques du Centre et du Nord de la Haute-Volta. Editions Technip.

Fabre, R., Ledru, P., Milési, J.-P., 1990. Le Protérozoïque inférieur (Birimien) du centre de la Côte-d'Ivoire: évolution tectonique et corrélations. Comptes Rendus Académie Sci. Sér. 2 Mécanique Phys. Chim. Sci. Univers Sci. Terre 311, 971–976.

Feybesse, J.-L., Billa, M., Guerrot, C., Duguey, E., Lescuyer, J.-L., Milési, J.-P., Bouchot, V., 2006. The paleoproterozoic Ghanaian province: Geodynamic model and ore controls, including regional stress modeling. Precambrian Res. 149, 149–196.

Foley, S., Tiepolo, M., Vannucci, R., 2002. Growth of early continental crust controlled by melting of amphibolite in subduction zones. Nature 417, 837–840. https://doi.org/10.1038/nature00799

Fontaine, A., Eglinger, A., Ada, K., André-Mayer, A.-S., Reisberg, L., Siebenaller, L., Le Mignot, E., Ganne, J., Poujol, M., 2017. Geology of the world-class Kiaka polyphase gold deposit, West African Craton, Burkina Faso. J. Afr. Earth Sci. 126, 96–122.

Ganne, J., Gerbault, M., Block, S., 2014. Thermo-mechanical modeling of lower crust exhumation—Constraints from the metamorphic record of the Palaeoproterozoic Eburnean orogeny, West African Craton. Precambrian Res. 243, 88–109. https://doi.org/10.1016/j.precamres.2013.12.016

Gapais, D., Barbarin, B., 1986. Quartz fabric transition in a cooling syntectonic granite (Hermitage Massif, France). Tectonophysics 125, 357–370. https://doi.org/10.1016/0040-1951(86)90171-X

García-Casco, A., Haissen, F., Castro, A., El-Hmidi, H., TORRES-ROLDÁN, R.L., Millán, G., 2003. Synthesis of staurolite in melting experiments of a natural metapelite: consequences for the phase relations in low-temperature pelitic migmatites. J. Petrol. 44, 1727–1757.

Gardien, V., Thompson, A.B., Grujic, D., Ulmer, P., 1995. Experimental melting of biotite + plagioclase + quartz ± muscovite assemblages and implications for crustal melting. J. Geophys. Res. Solid Earth 100, 15581–15591. https://doi.org/10.1029/95JB00916

Gasquet, D., Barbey, P., Adou, M., Paquette, J.L., 2003. Structure, Sr–Nd isotope geochemistry and zircon U–Pb geochronology of the granitoids of the Dabakala area (Côte d'Ivoire): evidence for a 2.3 Ga crustal growth event in the Palaeoproterozoic of West Africa? Precambrian Res. 127, 329–354. https://doi.org/10.1016/S0301-9268(03)00209-2

Giovenazzo, D., Ouedraogo, C., Séjourné, S., Hein, K.A.A., Jébrak, M., Malo, M., Harnois, L., Ouedraogo, A., Ouedraogo, P.I., Sountra, Y., Kambou, A., Coulibaly, G.K., Nassa, O., Nassa, N., Djiguemde, S., Hema, K.A.A., Bagoro, F., 2018. Notice explicative de la carte géologique 1/200 000, Feuille NC-30-XIV, Banfora-Kong, Effigis Géo-Solutions. ed.

Gleizes, G., Leblanc, D., Bouchez, J.L., 1997. Variscan granites of the Pyrenees revisited: their role as syntectonic markers of the orogen. Terra Nova 9, 38–41. https://doi.org/10.1046/j.1365-3121.1997.d01-9.x

Goujou, J., Buscail, F., Théveniaut, H., Dioh, E., Delor, C., Blein, O., Diallo, D., Ndiaye, P., Le Métour, J., Fullgraf, T., 2010. Notice explicative de la carte géologique à 1/200 000 du Sénégal, feuille Kossanto-Dalafi Est, 2010, Ministère des Mines, de l'Industrie, de l'Agro-Industrie et des PME. Dir. Mines Géologie Dakar.

Green, E., Holland, T., Powell, R., 2007. An order-disorder model for omphacitic pyroxenes in the system jadeite-diopside-hedenbergite-acmite, with applications to eclogitic rocks. Am. Mineral. 92, 1181–1189. https://doi.org/10.2138/am.2007.2401

Green, E.C.R., White, R.W., Diener, J.F.A., Powell, R., Holland, T.J.B., Palin, R.M., 2016. Activity–composition relations for the calculation of partial melting equilibria in metabasic rocks. J. Metamorph. Geol. 34, 845–869. https://doi.org/10.1111/jmg.12211

Green, T., Pearson, N., 1987. An experimental study of Nb and Ta partitioning between Ti-rich minerals and silicate liquids at high pressure and temperature. Geochim. Cosmochim. Acta 51, 55–62.

Green, T., Pearson, N., 1986. Rare-earth element partitioning between sphene and coexisting silicate liquid at high pressure and temperature. Chem. Geol. 55, 105–119.

Grenholm, M., 2019. The global tectonic context of the ca. 2.27-1.96 Ga Birimian Orogen–Insights from comparative studies, with implications for supercontinent cycles. Earth-Sci. Rev.

Grenholm, M., Jessell, M.W., Thébaud, N., 2019a. A geodynamic model for the Paleoproterozoic (ca. 2.27–1.96 Ga) Birimian Orogen of the southern West African Craton–Insights into an evolving accretionary-collisional orogenic system. Earth-Sci. Rev.

Grenholm, M., Jessell, M.W., Thébaud, N., 2019b. Paleoproterozoic volcano-sedimentary series in the ca. 2.27-1.96 Ga Birimian Orogen of the southeastern West African Craton. Precambrian Res.

Guergouz, C., Martin, L., Vanderhaeghe, O., Thébaud, N., Fiorentini, M., 2018. Zircon and monazite petrochronologic record of prolonged amphibolite to granulite facies metamorphism in the Ivrea-Verbano and Strona-Ceneri Zones, NW Italy. Lithos 308–309, 1–18. https://doi.org/10.1016/j.lithos.2018.02.014

Gueye, M., Ngom, P.M., Diène, M., Thiam, Y., Siegesmund, S., Wemmer, K., Pawlig, S., 2008. Intrusive rocks and tectono-metamorphic evolution of the Mako Paleoproterozoic belt (Eastern Senegal, West Africa). J. Afr. Earth Sci., Investigations of ore deposits within the West African Craton and surrounding areas 50, 88–110. https://doi.org/10.1016/j.jafrearsci.2007.09.013

Hammarstrom, J.M., Zen, E.-A., 1986. Aluminum in hornblende: An empirical igneous geobarometer. Am. Mineral. 71, 1297–1313.

Hasalová, P., Schulmann, K., Tabaud, A.S., Oliot, E., 2015. Microstructural evidences for mineralogical inheritance in partially molten rocks: example from the Vosges Mts. Bull. Société Géologique Fr. 186, 131–143. https://doi.org/10.2113/gssgfbull.186.2-3.131

Hermann, J., 2002. Allanite: thorium and light rare earth element carrier in subducted crust. Chem. Geol. 192, 289–306. https://doi.org/10.1016/S0009-2541(02)00222-X

Hildreth, W., 2004. Volcanological perspectives on Long Valley, Mammoth Mountain, and Mono Craters: several contiguous but discrete systems. J. Volcanol. Geotherm. Res. 136, 169–198. https://doi.org/10.1016/j.jvolgeores.2004.05.019

Hirdes, W., Davis, D.W., 1998. First U-Pb zircon age of extrusive volcanism in the Birimian Supergroup of Ghana/West Africa. J. Afr. Earth Sci. 27, 291–294. https://doi.org/10.1016/S0899-5362(98)00062-1

Hirdes, W., Davis, D.W., Lüdtke, G., Konan, G., 1996. Two generations of Birimian (Paleoproterozoic) volcanic belts in northeastern Côte d'Ivoire (West Africa): consequences for the 'Birimian controversy.' Precambrian Res. 80, 173–191. https://doi.org/10.1016/S0301-9268(96)00011-3

Hirth, G., Tullis, J., 1992. Dislocation creep regimes in quartz aggregates. J. Struct. Geol. 14, 145–159.

Hoffmann, J.E., Münker, C., Næraa, T., Rosing, M.T., Herwartz, D., Garbe-Schönberg, D., Svahnberg, H., 2011. Mechanisms of Archean crust formation inferred from high-precision HFSE systematics in TTGs. Geochim. Cosmochim. Acta 75, 4157–4178.
Holdaway, M.J., Mukhopadhyay, B., 1993. A reevaluation of the stability relations of andalusite: Thermochemical data and phase diagram for the aluminum silicates. Am. Mineral. 78, 298–315.
Holland, T., Powell, R., 2003. Activity–composition relations for phases in petrological calculations: an asymmetric multicomponent formulation. Contrib. Mineral. Petrol. 145, 492–501.
Holland, T., Powell, R., 1998. An internally consistent thermodynamic data set for phases of petrological interest. J. Metamorph. Geol. 16, 309–343.
Hollister, L.S., Grissom, G.C., Peters, E.K., Stowell, H.H., Sisson, V.B., 1987. Confirmation of the empirical correlation of Al in hornblende with pressure of solidification of calc-alkaline plutons. Am. Mineral. 72, 231–239.
Holness, M.B., Stripp, G., Humphreys, M.C.S., Veksler, I.V., Nielsen, T.F.D., Tegner, C., 2011. Silicate Liquid Immiscibility within the Crystal Mush: Late-stage Magmatic Microstructures in the Skaergaard Intrusion, East Greenland. J. Petrol. 52, 175–222. https://doi.org/10.1093/petrology/egq077
Hottin, G., Ouedraogo, O., 1975. Notice explicative de la carte géologique à 1: 1 000 000 de la république de Haute-Volta. BRGM.
Ilboudo, H., Lompo, M., Wenmenga, U., Napon, S., Naba, S., Ngom, P.M., 2017a. Evidence of a Volcanogenic Massive Sulfide (ZnPbCuAg) district within the Tiébélé Birimian (Paleoproterozoic) Greenstone Belts, Southern Burkina Faso (West–Africa). J. Afr. Earth Sci. 129, 792–813.
Ilboudo, H., Sawadogo, S., Kagambega, N., Remmal, T., 2021. Petrology, geochemistry, and source of the emplacement model of the Paleoproterozoic Tiébélé Granite Pluton, Burkina Faso (West-Africa): contribution to mineral exploration. Int. J. Earth Sci. https://doi.org/10.1007/s00531-021-02039-3
Ilboudo, H., Sawadogo, S., Zongo, G.H., Naba, S., Wenmenga, U., Lompo, M., 2020. Geochemistry and geodynamic constraint of volcanic and plutonic magmatism within the Banfora Belt (Burkina-Faso, West-Africa): contribution to Mineral Exploration. Geol. Soc. Lond. Spec. Publ. 502.
Ilboudo, H., Wenmenga, U., Sawadogo, S., Remmal, T., 2017b. Mise en évidence d’un assemblage à disthène - staurotide - grenat dans le secteur de Mangodara, ceinture de Banfora, Burkina Faso, Afrique de l’Ouest : implication dans la genèse des gîtes minéraux polymétalliques. Afr. Sci. 13, 220–231.
Jackson, M.D., Blundy, J., Sparks, R.S.J., 2018. Chemical differentiation, cold storage and remobilization of magma in the Earth’s crust. Nature 564, 405–409. https://doi.org/10.1038/s41586-018-0746-2
Jackson, M.D., Cheadle, M.J., Atherton, M.P., 2003. Quantitative modeling of granitic melt generation and segregation in the continental crust. J. Geophys. Res. Solid Earth 108. https://doi.org/10.1029/2001JB001050
Johnson, M.C., Rutherford, M.J., 1989. Experimental calibration of the aluminum-in-hornblende geobarometer with application to Long Valley caldera (California) volcanic rocks. Geology 17, 837–841. https://doi.org/10.1130/0091-7613(1989)017<0837:ECOTAI>2.3.CO;2
Kelsey, D.E., Clark, C., Hand, M., 2008. Thermobarometric modelling of zircon and monazite growth in melt-bearing systems: examples using model metapelitic and metapsammitic granulites. J. Metamorph. Geol. 26, 199–212. https://doi.org/10.1111/j.1525-1314.2007.00757.x
Kelsey, D.E., Powell, R., 2011. Progress in linking accessory mineral growth and breakdown to major mineral evolution in metamorphic rocks: a thermodynamic approach in the Na2O-CaO-K2O-FeO-MgO-Al2O3-SiO2-H2O-TiO2-ZrO2 system. J. Metamorph. Geol. 29, 151–166. https://doi.org/10.1111/j.1525-1314.2010.00910.x
Kouamelan, A.N., 1996. Géochronologie et Géochimie des Formations Archéennes et Protérozoïques de la Dorsale de Man en Côte d’Ivoire. Implications pour la Transition Archéen-Protéozoïque.

Lambert-Smith, J.S., Lawrence, D.M., Müller, W., Treloar, P.J., 2016. Palaeotectonic setting of the south-eastern Kédougou-Kéniéba Inlier, West Africa: new insights from igneous trace element geochemistry and U-Pb zircon ages. Precambrian Res. 274, 110–135.

Laurent, O., Björnsen, J., Wotzlaw, J.-F., Bretscher, S., Pimenta Silva, M., Moyen, J.-F., Ulmer, P., Bachmann, O., 2020. Earth's earliest granitoids are crystal-rich magma reservoirs tapped by silicic eruptions. Nat. Geosci. 13, 163–169. https://doi.org/10.1038/s41561-019-0520-6

Laurent, O., Martin, H., Moyen, J.-F., Doucelance, R., 2014. The diversity and evolution of late-Archean granitoids: Evidence for the onset of "modern-style" plate tectonics between 3.0 and 2.5 Ga. Lithos 205, 208–235.

Law, R.D., 2014. Deformation thermometry based on quartz c-axis fabrics and recrystallization microstructures: A review. J. Struct. Geol. 66, 129–161.

Le Breton, N., Thompson, A.B., 1988. Fluid-absent (dehydration) melting of biotite in metapelites in the early stages of crustal anatexis. Contrib. Mineral. Petrol. 99, 226–237.

Ledru, P., Pons, J., Milési, J.-P., Feybesse, J.-L., Johan, V., 1991. Transcurrent tectonics and polycyclic evolution in the Lower Proterozoic of Senegal-Mali. Precambrian Res. 50, 337–354.

Lemoine, S., 1988. Evolution géologique de la région de Dabakala (NE de la Côte-d'Ivoire) au Protérozoïque. Possibilités d'extension au reste de la Côte-d'Ivoire et au Burkina Faso: similitudes et différences; les linéaments de Greenville-Ferkessédougou et Grand Cess-Niakaramandougou. Thèse ès Sciences, Univ. Cl.-Ferrand, France.

Lemoine, S., Tempier, P., Bassot, J., Caen-Vachette, M., Vialette, Y., Toure, S., Wenmenga, U., 1990. The Burkinian orogenic cycle, precursor of the Eburnian orogeny in West Africa. Geol. J. 25, 171–188.

Liégeois, J.P., Claessens, W., Camara, D., Klerkx, J., 1991. Short-lived Eburnian orogeny in southern Mali. Geology, tectonics, U-Pb and Rb-Sr geochronology. Precambrian Res. 50, 111–136. https://doi.org/10.1016/0301-9268(91)90050-K

Linnen, R., Cuney, M., 2005. Granite-related rare-element deposits and experimental constraints on Ta-Nb-W-Sn-Zr-Hf mineralization, in Linnen RL and Samson IM, eds., rare-element geochemistry and mineral deposits.

Liou, J., Kuniyoshi, S., Ito, K., 1974. Experimental studies of the phase relations between greenschist and amphibolite in a basaltic system. Am. J. Sci. 274, 613–632.

Liou, P., Guo, J., 2019. Generation of Archaean TTG Gneisses Through Amphibole-Dominated Fractionation. J. Geophys. Res. Solid Earth 124, 3605–3619. https://doi.org/10.1029/2018JB017024

Lompo, M., 2010. Paleoproterozoic structural evolution of the Man-Leo Shield (West Africa). Key structures for vertical to transcurrent tectonics. J. Afr. Earth Sci. 58, 19–36.

Lompo, M., 2009. Geodynamic evolution of the 2.25-2.0 Ga Palaeoproterozoic magmatic rocks in the Man-Leo Shield of the West African Craton. A model of subsidence of an oceanic plateau. Geol. Soc. Lond. Spec. Publ. 323, 231–254.

London, D., 2014. A petrologic assessment of internal zonation in granitic pegmatites. Lithos 184–187, 74–104. https://doi.org/10.1016/j.lithos.2013.10.025

London, D., 2009. The origin of primary textures in granitic pegmatites. Can. Mineral. 47, 697–724.

London, D., 2008. Pegmatites. Can Miner. 10, 347.

London, D., 1989. Lithophile rare element concentration in silicic rocks: The alkaline trend in granitic systems. Geol. Mineral. Assoc. Can. Program Abstr. 14, A21.

Lüdtke, G., Hirdes, W., Konan, G., Koné, Y., Yao, C., Diarra, S., Zamblé, Z., 1998. Géologie de la région Haute Comoé Nord—feuilles Kong (4b et 4d) et Téhini-Bouna (3a à 3d). Dir. Géologie Abidj. Bull. 178.

Ludwig, K., 2003. User's manual for Isoplot/EX, version 3.00. Geochronological Toolkit Microsoft Excel 4, 71.

Martin, H., Moyen, J.-F., 2002. Secular changes in tonalite-trondhjemite-granodiorite composition as markers of the progressive cooling of Earth. Geology 30, 319–322. https://doi.org/10.1130/0091-7613(2002)030<0319:SCITTG>2.0.CO;2

Martin, R.F., De Vito, C., 2005. The patterns of enrichment in felsic pegmatites ultimately depend on tectonic setting. Can. Mineral. 43, 2027–2048. https://doi.org/10.2113/gscanmin.43.6.2027

Martini, A., Bitencourt, M. de F., Weinberg, R.F., De Toni, G.B., Lauro, V.S.N., 2019. From migmatite to magma - crustal melting and generation of granite in the Camboriú Complex, south Brazil. Lithos 340–341, 270–286. https://doi.org/10.1016/j.lithos.2019.05.017

Maruyama, S., Suzuki, K., Liou, J.G., 1983. Greenschist–amphibolite transition equilibria at low pressures. J. Petrol. 24, 583–604.

Masurel, Q., Eglinger, A., Thébaud, N., Allibone, A., André-Mayer, A.-S., McFarlane, H., Miller, J., Jessell, M., Aillères, L., Vanderhaeghe, O., Salvi, S., Baratoux, L., Perrouty, S., Begg, G., Fougerouse, D., Hayman, P., Wane, O., Tshibubudze, A., Parra-Avila, L., Kouamélan, A., Amponsah, P.O., 2021. Paleoproterozoic gold events in the southern West African Craton: review and synopsis. Miner. Deposita. https://doi.org/10.1007/s00126-021-01052-5

McDonough, W.F., Sun, S.-S., 1995. The composition of the Earth. Chem. Geol. 120, 223–253.

McFarlane, C.R.M., Mavrogenes, J., Lentz, D., King, K., Allibone, A., Holcombe, R., 2011. Geology and Intrusion-Related Affinity of the Morila Gold Mine, Southeast Mali. Econ. Geol. 106, 727–750. https://doi.org/10.2113/econgeo.106.5.727

Mehnert, K.R., 1968. Migmatites and the origin of granitic rocks. Megascopic Struct. Migmatite 7–42.

Mériaud, N., Thébaud, N., Masurel, Q., Hayman, P., Jessell, M.W., Kemp, A., Evans, N.J., Fisher, C.M., Scott, P.M., 2020. Lithostratigraphic evolution of the Bandamian Volcanic Cycle in central Côte d'Ivoire: Insights into the late Eburnean magmatic resurgence and its geodynamic implications. Precambrian Res. 105847. https://doi.org/10.1016/j.precamres.2020.105847

Metelka, V., Baratoux, L., Naba, S., Jessell, M.W., 2011. A geophysically constrained litho-structural analysis of the Eburnean greenstone belts and associated granitoid domains, Burkina Faso, West Africa. Precambrian Res. 190, 48–69. https://doi.org/10.1016/j.precamres.2011.08.002

Milési, J., 1989. West African gold deposits in their Lower Proterozoic lithostructural setting. Chron. Rech. Minière 3–98.

Milési, J.-P., Feybesse, J.-L., Pinna, P., Deschamps, Y., Kampunzu, H., Muhongo, S., Lescuyer, J.-L., Le Goff, E., Delor, C., Billa, M., 2004. Geological map of Africa 1: 10,000,000, SIGAfrique project. Presented at the 20th Conference of African Geology, BRGM, Orléans, France, pp. 2–7.

Montel, J.-M., Vielzeuf, D., 1997. Partial melting of metagreywackes, Part II. Compositions of minerals and melts. Contrib. Mineral. Petrol. 128, 176–196.

Moody, J.B., Meyer, D., Jenkins, J.E., 1983. Experimental characterization of the greenschist/amphibolite boundary in mafic systems. Am. J. Sci. 283, 48–92. https://doi.org/10.2475/ajs.283.1.48

Moyen, J.-F., 2011. The composite Archaean grey gneisses: Petrological significance, and evidence for a non-unique tectonic setting for Archaean crustal growth. Lithos, Secular variations in magmatism and tectonic implications 123, 21–36. https://doi.org/10.1016/j.lithos.2010.09.015

Moyen, J.-F., Champion, D., Smithies, R., 2009. The geochemistry of Archaean plagioclase-rich granites as a marker of source enrichment and depth of melting. Earth Environ. Sci. Trans. R. Soc. Edinb. 100, 35–50.

Moyen, J.-F., Stevens, G., 2006. Experimental constraints on TTG petrogenesis: implications for Archean geodynamics. Geophys. Monogr.-Am. Geophys. Union 164, 149.

Müller, A., Romer, R.L., Pedersen, R.-B., 2017. The Sveconorwegian pegmatite province–thousands of pegmatites without parental granites. Can. Mineral. 55, 283–315.

Mutch, E.J.F., Blundy, J.D., Tattitch, B.C., Cooper, F.J., Brooker, R.A., 2016. An experimental study of amphibole stability in low-pressure granitic magmas and a revised Al-in-hornblende geobarometer. Contrib. Mineral. Petrol. 171. https://doi.org/10.1007/s00410-016-1298-9

Ndiaye, P.M., Dia, A., Vialette, Y., Diallo, D., Ngom, P., Sylla, M., Wade, S., Dioh, E., 1997. Données pétrographiques, geochimiques et géochronologiques nouvelles sur les granitoïdes du Paléoprotérozoïque du Supergroupe de Dialé-Daléma (Sen; égal Oriental): Implications pétrogénétiques et géodynamiques. J. Afr. Earth Sci. 25, 193–208.

Nesbitt, H.W., Young, G.M., 1984. Prediction of some weathering trends of plutonic and volcanic rocks based on thermodynamic and kinetic considerations. Geochim. Cosmochim. Acta 48, 1523–1534.

Nesbitt, H.W., Young, G.M., 1982. Early Proterozoic climates and plate motions inferred from major element chemistry of lutites. Nature 299, 715–717.

Nude, P., Hanson, J., Dampare, S., Akiti, T., OsAE, S., Nyarko, E., Zkaria, N., Enti-Brown, S., 2011. Geochemistry of Pegmatites associated with the cape coast granite complex in the Egyaa and Akim Oda areas of southern Ghana. Ghana J. Sci. 51, 89–100.

Palin, R.M., White, R.W., Green, E.C.R., 2016. Partial melting of metabasic rocks and the generation of tonalitic–trondhjemitic–granodioritic (TTG) crust in the Archaean: Constraints from phase equilibrium modelling. Precambrian Res. 287, 73–90. https://doi.org/10.1016/j.precamres.2016.11.001

Parra-Avila, L.A., Baratoux, L., Eglinger, A., Fiorentini, M.L., Block, S., 2019. The Eburnean magmatic evolution across the Baoulé-Mossi domain: Geodynamic implications for the West African Craton. Precambrian Res. 332, 105392. https://doi.org/10.1016/j.precamres.2019.105392

Parra-Avila, L.A., Kemp, A.I.S., Fiorentini, M.L., Belousova, E.A., Baratoux, L., Block, S., Jessell, M.W., Bruguier, O., Begg, G.C., Miller, J., Davis, J., McCuaig, T.C., 2017. The geochronological evolution of the Paleoproterozoic Baoulé-Mossi domain of the Southern West African Craton. Precambrian Res. 300, 1–27. https://doi.org/10.1016/j.precamres.2017.07.036

Passchier, C.W., Trouw, R., 2005. Deformation mechanisms. Microtectonics 25–66.

Patiño Douce, A.E., 1999. What do experiments tell us about the relative contributions of crust and mantle to the origin of granitic magmas? Geol. Soc. Lond. Spec. Publ. 168, 55–75. https://doi.org/10.1144/GSL.SP.1999.168.01.05

Patiño Douce, A.E., Beard, J.S., 1995. Dehydration-melting of Biotite Gneiss and Quartz Amphibolite from 3 to 15 kbar. J. Petrol. 36, 707–738. https://doi.org/10.1093/petrology/36.3.707

Pattison, D.R., Spear, F.S., 2018. Kinetic control of staurolite–Al2SiO5 mineral assemblages: Implications for Barrovian and Buchan metamorphism. J. Metamorph. Geol. 36, 667–690.

Pattison, D.R.M., 1992. Stability of Andalusite and Sillimanite and the Al2SiO5 Triple Point: Constraints from the Ballachulish Aureole, Scotland. J. Geol. 100, 423–446. https://doi.org/10.1086/629596

Pawlig, S., Gueye, M., Klischies, R., Schwarz, S., Wemmer, K., Siegesmund, S., 2006. Geochemical and Sr-Nd isotopic data on the Birimian of the Kedougou-Kenieba inlier (Eastern Senegal): Implications on the Palaeoproterozoic evolution of the West African craton. South Afr. J. Geol. 109, 411–427.

Peacock, S.M., Rushmer, T., Thompson, A.B., 1994. Partial melting of subducting oceanic crust. Earth Planet. Sci. Lett. 121, 227–244. https://doi.org/10.1016/0012-821X(94)90042-6

Peccerillo, A., Taylor, S., 1976. Geochemistry of Eocene calc-alkaline volcanic rocks from the Kastamonu area, northern Turkey. Contrib. Mineral. Petrol. 58, 63–81.

Perrouty, S., Aillères, L., Jessell, M.W., Baratoux, L., Bourassa, Y., Crawford, B., 2012. Revised Eburnean geodynamic evolution of the gold-rich southern Ashanti Belt, Ghana, with new field and geophysical evidence of pre-Tarkwaian deformations. Precambrian Res. 204, 12–39.

Petersson, A., Scherstén, A., Kemp, A., Bara, K., Per, K., Solomon, A., 2016. Zircon U-Pb-Hf evidence for subduction related crustal growth and reworking of Archaean crust within the Palaeoproterozoic Birimian terrane, West African Craton, SE Ghana. Precambrian Res. 275, 286–309. http://dx.doi.org/10.1016/j.precamres.2016.01.006

Petford, N., Atherton, M., 1996. Na-rich partial melts from newly underplated basaltic crust: the Cordillera Blanca Batholith, Peru. J. Petrol. 37, 1491–1521.

Pons, J., Barbey, P., Dupuis, D., Léger, J., 1995. Mechanisms of pluton emplacement and structural evolution of a 2.1 Ga juvenile continental crust: the Birimian of southwestern Niger. Precambrian Res. 70, 281–301.

Pouclet, A., Vidal, M., Delor, C., Simeon, Y., Alric, G., 1996. Le volcanisme birimien du nord-est de la Côte-d'Ivoire, mise en évidence de deux phases volcano-tectoniques distinctes dans l'évolution géodynamique du Paléoprotérozoique. Bull. Société Géologique Fr. 167, 529–541.

Rapp, R.P., Watson, E.B., 1995. Dehydration melting of metabasalt at 8–32 kbar: implications for continental growth and crust-mantle recycling. J. Petrol. 36, 891–931.

Rapp, R.P., Watson, E.B., Miller, C.F., 1991. Partial melting of amphibolite/eclogite and the origin of Archean trondhjemites and tonalites. Precambrian Res. 51, 1–25.

Reichardt, H., Weinberg, R.F., 2012. Hornblende Chemistry in Meta- and Diatexites and its Retention in the Source of Leucogranites: an Example from the Karakoram Shear Zone, NW India. J. Petrol. 53, 1287–1318. https://doi.org/10.1093/petrology/egs017

Robin, P.-Y.F., 1979. Theory of metamorphic segregation and related processes. Geochim. Cosmochim. Acta 43, 1587–1600. https://doi.org/10.1016/0016-7037(79)90179-0

Roda-Robles, E., Vieira, R., Lima, A., Pesquera, A., Noronha, F., Fontan, F., 2007. The Fregeneda–Almendra pegmatitic field (Spain & Portugal): mineral assemblages and regional zonation. Presented at the Granitic Pegmatites: The State of the Art–International Symposium, Porto, Portugal, submitted.

Roddaz, M., Debat, P., Nikiéma, S., 2007. Geochemistry of Upper Birimian sediments (major and trace elements and Nd–Sr isotopes) and implications for weathering and tectonic setting of the Late Paleoproterozoic crust. Precambrian Res. 159, 197–211. https://doi.org/10.1016/j.precamres.2007.06.008

Rudnick, R.L., Gao, S., 2003. Composition of the continental crust. Treatise Geochem. 3, 659.

Rushmer, T., 1991. Partial melting of two amphibolites: contrasting experimental results under fluid-absent conditions. Contrib. Mineral. Petrol. 107, 41–59.

Saha-Fouotsa, A.N., Vanderhaeghe, O., Barbey, P., Eglinger, A., Tchameni, R., Zeh, A., Tchunte, P.F., Nomo, E.N., 2019. The geologic record of the exhumed root of the Central African Orogenic Belt in the central Cameroon domain (Mbé – Sassa-Mbersi region). J. Afr. Earth Sci. 151, 286–314. https://doi.org/10.1016/j.jafrearsci.2018.12.008

Sakyi, P.A., Addae, R.A., Su, B.-X., Dampare, S.B., Abitty, E., Su, B.-C., Liu, B., Asiedu, D.K., 2020. Petrology and geochemistry of TTG and K-rich Paleoproterozoic Birimian granitoids of the West African Craton (Ghana): Petrogenesis and tectonic implications. Precambrian Res. 336, 105492. https://doi.org/10.1016/j.precamres.2019.105492

Sakyi, P.A., Su, B.-X., Anum, S., Kwayisi, D., Dampare, S.B., Anani, C.Y., Nude, P.M., 2014. New zircon U–Pb ages for erratic emplacement of 2213–2130Ma Paleoproterozoic calc-alkaline I-type granitoid rocks in the Lawra Volcanic Belt of Northwestern Ghana, West Africa. Precambrian Res. 254, 149–168. https://doi.org/10.1016/j.precamres.2014.08.009

Sawyer, E.W., 2010. Migmatites formed by water-fluxed partial melting of a leucogranodiorite protolith: microstructures in the residual rocks and source of the fluid. Lithos 116, 273–286.

Sawyer, E.W., 2001. Melt segregation in the continental crust: distribution and movement of melt in anatectic rocks. J. Metamorph. Geol. 19, 291–309. https://doi.org/10.1046/j.0263-4929.2000.00312.x

Sawyer, E.W., 1999. Criteria for the recognition of partial melting. Phys. Chem. Earth Part Solid Earth Geod. 24, 269–279.

Sawyer, E.W., 1991. Disequilibrium Melting and the Rate of Melt–Residuum Separation During Migmatization of Mafic Rocks from the Grenville Front, Quebec. J. Petrol. 32, 701–738. https://doi.org/10.1093/petrology/32.4.701

Schmidt, M.W., 1992. Amphibole composition in tonalite as a function of pressure: an experimental calibration of the Al-in-hornblende barometer. Contrib. Mineral. Petrol. 110, 304–310. https://doi.org/10.1007/BF00310745

Schmidt, M.W., Poli, S., 2004. Magmatic epidote. Rev. Mineral. Geochem. 56, 399–430.

Schmidt, M.W., Thompson, A.B., 1996. Epidote in calc-alkaline magmas; an experimental study of stability, phase relationships, and the role of epidote in magmatic evolution. Am. Mineral. 81, 462–474.

Schulmann, K., Edel, J.-B., Hasalová, P., Cosgrove, J., Ježek, J., Lexa, O., 2009. Influence of melt induced mechanical anisotropy on the magnetic fabrics and rheology of deforming migmatites, Central Vosges, France. J. Struct. Geol. 31, 1223–1237. https://doi.org/10.1016/j.jsg.2009.07.004

Schumacher, J., 1997. The estimation of the proportion of ferric iron in the electron-microprobe analysis of amphiboles. Can Miner. 35, 238–246.

Schwindinger, M., Weinberg, R.F., 2017. A felsic MASH zone of crustal magmas — Feedback between granite magma intrusion and in situ crustal anatexis. Lithos 284–285, 109–121. https://doi.org/10.1016/j.lithos.2017.03.030

Schwindinger, M., Weinberg, R.F., Clos, F., 2019. Wet or dry? The difficulty of identifying the presence of water during crustal melting. J. Metamorph. Geol. 37, 339–358.

Shand, S.J., 1943. Eruptive rocks: their genesis, composition, and classification, with a chapter on meteorites. J. Wiley & sons, Incorporated.

Shaw, D.M., 1968. A review of K-Rb fractionation trends by covariance analysis. Geochim. Cosmochim. Acta 32, 573–601. https://doi.org/10.1016/0016-7037(68)90050-1

Shaw, R.A., Goodenough, K.M., Roberts, N.M.W., Horstwood, M.S.A., Chenery, S.R., Gunn, A.G., 2016. Petrogenesis of rare-metal pegmatites in high-grade metamorphic terranes: A case study from the Lewisian Gneiss Complex of north-west Scotland. Precambrian Res. 281, 338–362. https://doi.org/10.1016/j.precamres.2016.06.008

Skjerlie, K.P., Patiño Douce, A.E., 2002. The Fluid-absent Partial Melting of a Zoisite-bearing Quartz Eclogite from 1·0 to 3·2 GPa; Implications for Melting in Thickened Continental Crust and for Subduction-zone Processes. J. Petrol. 43, 291–314. https://doi.org/10.1093/petrology/43.2.291

Solgadi, F., Moyen, J.-F., Vanderhaeghe, O., Sawyer, E.W., Reisberg, L., 2007. The role of crustal anatexis and mantle-derived magmas in the genesis of synorogenic Hercynian granites of the Livradois area, French Massif Central. Can. Mineral. 45, 581–606. https://doi.org/10.2113/gscanmin.45.3.581

Soumaila, A., Henry, P., Garba, Z., Rossi, M., 2008. REE patterns, Nd-Sm and U-Pb ages of the metamorphic rocks of the Diagorou-Darbani greenstone belt (Liptako, SW Niger): implication for Birimian (Palaeoproterozoic) crustal genesis. Geol. Soc. Lond. Spec. Publ. 297, 19–32. https://doi.org/10.1144/SP297.2

Spear, F.S., Kohn, M.J., Cheney, J.T., 1999. P-T paths from anatectic pelites. Contrib. Mineral. Petrol. 134, 17–32. https://doi.org/10.1007/s004100050466

Stevenson, D.J., 1989. Spontaneous small-scale melt segregation in partial melts undergoing deformation. Geophys. Res. Lett. 16, 1067–1070. https://doi.org/10.1029/GL016i009p01067

Streckeisen, A., Le Maitre, R., 1979. A chemical approximation to the modal QAPF classification of the igneous rocks.

Sun, S.-S., McDonough, W.F., 1989. Chemical and isotopic systematics of oceanic basalts: implications for mantle composition and processes. Geol. Soc. Lond. Spec. Publ. 42, 313–345.

Tafur, L.A., Diener, J.F.A., 2020. Mineral equilibrium constraints on the feasibility of diffusive H2O-fluxed melting in the continental crust. J. Metamorph. Geol. 38, 719–742. https://doi.org/10.1111/jmg.12536

Tagini, B., 1971. Esquisse structurale de la Côte d'Ivoire. Essai de géotectonique régionale. These Univ Lausanne Soc. Etat Pour Dev. Min. Cote Ivoire.

Tapsoba, B., Lo, C.-H., Jahn, B.-M., Chung, S.-L., Wenmenga, U., Iizuka, Y., 2013. Chemical and Sr–Nd isotopic compositions and zircon U–Pb ages of the Birimian granitoids from NE Burkina Faso, West African Craton: Implications on the geodynamic setting and crustal evolution. Precambrian Res. 224, 364–396. https://doi.org/10.1016/j.precamres.2012.09.013

Tassinari, C.C., Macambira, M.J., 1999. Geochronological provinces of the Amazonian Craton. Episodes-Newsmag. Int. Union Geol. Sci. 22, 174–182.

Taylor, S., 1965. The application of trace element data to problems in petrology. Phys. Chem. Earth 6, 133–213.

Tera, F., Wasserburg, G.J., 1972. U-Th-Pb systematics in lunar highland samples from the Luna 20 and Apollo 16 missions. Earth Planet. Sci. Lett. 17, 36–51. https://doi.org/10.1016/0012-821X(72)90257-9

Thomas, W., Ernst, W., 1990. The aluminium content of hornblende in calc-alkaline granitic rocks: A mineralogic barometer calibrated experimentally to 12 kbars. Fluid-Miner. Interact. Tribute HP Eugster 59–63.

Thompson, A.B., 1982. Dehydration melting of pelitic rocks and the generation of H 2 O-undersaturated granitic liquids. Am. J. Sci. 282, 1567–1595.

Tiepolo, M., Oberti, R., Vannucci, R., 2002. Trace-element incorporation in titanite: constraints from experimentally determined solid/liquid partition coefficients. Chem. Geol. 191, 105–119.

Tinkham, D.K., Zuluaga, C.A., Stowell, H.H., 2001. Metapelite phase equilibria modeling in MnNCKFMASH: the effect of variable Al2O3 and MgO/(MgO+ FeO) on mineral stability. Geol. Mater. Res. 3, 1–42.

Touret, J.L.R., Hartel, T.H.D., 1990. Synmetamorphic Fluid Inclusions in Granulites, in: Vielzeuf, D., Vidal, Ph. (Eds.), Granulites and Crustal Evolution, NATO ASI Series. Springer Netherlands, Dordrecht, pp. 397–417. https://doi.org/10.1007/978-94-009-2055-2_20

Touret, J.L.R., Huizenga, J.-M., 2011. Fluids in granulites. Geol. Soc. Am. Mem. 207, 25–37.

Touret, J.L.R., Nijland, T.G., 2013. Prograde, Peak and Retrograde Metamorphic Fluids and Associated Metasomatism in Upper Amphibolite to Granulite Facies Transition Zones. Metasomatism Chem. Transform. Rock 415–469. https://doi.org/10.1007/978-3-642-28394-9_11

Tshibubudze, A., Hein, K.A.A., 2013. Structural setting of gold deposits in the Oudalan-Gorouol volcano-sedimentary belt east of the Markoye Shear Zone, West African craton. J. Afr. Earth Sci. 80, 31–47.

Tshibubudze, A., Hein, K.A.A., McCuaig, T.C., 2015. The relative and absolute chronology of strato-tectonic events in the Gorom-Gorom granitoid terrane and Oudalan-Gorouol belt, northeast Burkina Faso. J. Afr. Earth Sci. 112, 382–418.

Tshibubudze, A., Hein, K.A.A., Peters, L., Woolfe, A., McCuaig, T., 2013. Oldest U-Pb crystallisation age for the West African Craton From the Oudalan-Gorouol Belt of Burkina Faso. South Afr. J. Geol. 116, 169–181.

Turlin, F., Deruy, C., Eglinger, A., Vanderhaeghe, O., André-Mayer, A.-S., Poujol, M., Moukhsil, A., Solgadi, F., 2018. A 70 Ma record of suprasolidus conditions in the large, hot, long-duration Grenville Orogen. Terra Nova 30, 233–243.

Van der Molen, I., 1985. Interlayer material transport during layer-normal shortening. Part II. Boudinage, pinch-and-swell and migmatite at Søndre Strømfjord Airport, West Greenland. Tectonophysics 115, 297–313. https://doi.org/10.1016/0040-1951(85)90143-X

Van der Molen, I., Paterson, M., 1979. Experimental deformation of partially-melted granite. Contrib. Mineral. Petrol. 70, 299–318.

Vanderhaeghe, O., 2009. Migmatites, granites and orogeny: Flow modes of partially-molten rocks and magmas associated with melt/solid segregation in orogenic belts. Tectonophysics, Hot orogens 477, 119–134. https://doi.org/10.1016/j.tecto.2009.06.021

Vanderhaeghe, O., 2001. Melt segregation, pervasive melt migration and magma mobility in the continental crust: the structural record from pores to orogens. Phys. Chem. Earth Part Solid Earth Geod. 26, 213–223.

Vanderhaeghe, O., Guergouz, C., Fabre, C., Duchêne, S., Baratoux, D., 2019. Secular cooling and crystallization of partially molten Archaean continental crust over 1 Ga. Comptes Rendus Geosci., New aspects of magma storage and transfer 351, 562–573. https://doi.org/10.1016/j.crte.2019.07.002

Vanderhaeghe, O., Ledru, P., Thiéblemont, D., Egal, E., Cocherie, A., Tegyey, M., Milési, J.-P., 1998. Contrasting mechanism of crustal growth: Geodynamic evolution of the Paleoproterozoic granite–greenstone belts of French Guiana. Precambrian Res. 92, 165–193. https://doi.org/10.1016/S0301-9268(98)00074-6

Vanderhaeghe, O., Teyssier, C., Wysoczanski, R., 1999. Structural and geochronological constraints on the role of partial melting during the formation of the Shuswap metamorphic core complex at the latitude of the Thor-Odin dome, British Columbia. Can. J. Earth Sci. 36, 917–943.

Vauchez, A., Hollanda, M.H.B.M., Monié, P., Mondou, M., Egydio-Silva, M., 2019. Slow cooling and crystallization of the roots of the Neoproterozoic Araçuaí hot orogen (SE Brazil): Implications for rheology, strain distribution, and deformation analysis. Tectonophysics 766, 500–518. https://doi.org/10.1016/j.tecto.2019.05.013

Vidal, M., Alric, G., 1994. The Palaeoproterozoic (Birimian) of Haute-Comoé in the West African craton, Ivory Coast: a transtensional back-arc basin. Precambrian Res. 65, 207–229.

Vidal, M., Delor, C., Pouclet, A., Simeon, Y., Alric, G., 1996. Evolution géodynamique de l’Afrique de l’Ouest entre 2, 2 Ga et 2 Ga; le style" archéen" des ceintures vertes et des ensembles sédimentaires birimiens du nord-est de la Côte-d’Ivoire. Bull. Société Géologique Fr. 167, 307–319.

Vidal, M., Gumiaux, C., Cagnard, F., Pouclet, A., Ouattara, G., Pichon, M., 2009. Evolution of a Paleoproterozoic “weak type” orogeny in the West African Craton (Ivory Coast). Tectonophysics 477, 145–159.

Vielzeuf, D., Holloway, J.R., 1988. Experimental determination of the fluid-absent melting relations in the pelitic system. Contrib. Mineral. Petrol. 98, 257–276.

Vielzeuf, D., Montel, J.-M., 1994. Partial melting of metagreywackes. Part I. Fluid-absent experiments and phase relationships. Contrib. Mineral. Petrol. 117, 375–393. https://doi.org/10.1007/BF00307272

Wane, O., Liégeois, J.-P., Thébaud, N., Miller, J., Metelka, V., Jessell, M.W., 2018. The onset of the Eburnean collision with the Kenema-Man craton evidenced by plutonic and volcanosedimentary rock record of the Masssigui region, southern Mali. Precambrian Res. 305, 444–478. https://doi.org/10.1016/j.precamres.2017.11.008

Weinberg, R.F., 2006. Melt segregation structures in granitic plutons. Geology 34, 305–308. https://doi.org/10.1130/G22406.1

Weinberg, R.F., 1999. Mesoscale pervasive felsic magma migration: alternatives to dyking. Lithos 46, 393–410.

Weinberg, R.F., Hasalová, P., 2015. Water-fluxed melting of the continental crust: A review. Lithos 212, 158–188.

Weinberg, R.F., Hasalová, P., Ward, L., Fanning, C.M., 2013. Interaction between deformation and magma extraction in migmatites: Examples from Kangaroo Island, South Australia. GSA Bull. 125, 1282–1300. https://doi.org/10.1130/B30781.1

Weinberg, R.F., Sial, A.N., Mariano, G., 2004. Close spatial relationship between plutons and shear zones. Geology 32, 377–380. https://doi.org/10.1130/G20290.1

Whalen, J.B., Currie, K.L., Chappell, B.W., 1987. A-type granites: geochemical characteristics, discrimination and petrogenesis. Contrib. Mineral. Petrol. 95, 407–419.

White, R., Powell, R., Clarke, G., 2003. Prograde Metamorphic Assemblage Evolution during Partial Melting of Metasedimentary Rocks at Low Pressures: Migmatites from Mt Stafford, Central Australia. J. Petrol. 44, 1937–1960.

White, R., Powell, R., Holland, T., 2007. Progress relating to calculation of partial melting equilibria for metapelites. J. Metamorph. Geol. 25, 511–527.

White, R.W., Powell, R., Clarke, G.L., 2002. The interpretation of reaction textures in Fe-rich metapelitic granulites of the Musgrave Block, central Australia: constraints from mineral equilibria calculations in the system K2O–FeO–MgO–Al2O3–SiO2–H2O–TiO2–Fe2O3. J. Metamorph. Geol. 20, 41–55. https://doi.org/10.1046/j.0263-4929.2001.00349.x

Whitney, D.L., 2002. Coexisting andalusite, kyanite, and sillimanite: Sequential formation of three Al2SiO5 polymorphs during progressive metamorphism near the triple point, Sivrihisar, Turkey. Am. Mineral. 87, 405–416. https://doi.org/10.2138/am-2002-0404

Wickham, S.M., 1987. The segregation and emplacement of granitic magmas. J. Geol. Soc. 144, 281–297. https://doi.org/10.1144/gsjgs.144.2.0281

Winther, K., Newton, R., 1991. Experimental melting of hydrous low-K tholeiite: evidence on the origin of Archaean cratons: Geological Society of Denmark Bulletin, v. 39.

Wolf, M.B., Wyllie, P.J., 1994. Dehydration-melting of amphibolite at 10 kbar: the effects of temperature and time. Contrib. Mineral. Petrol. 115, 369–383.

Wyllie, P.J., Wolf, M.B., 1993. Amphibolite dehydration-melting: sorting out the solidus. Geol. Soc. Lond. Spec. Publ. 76, 405–416.

Yakymchuk, C., Brown, M., 2014. Behaviour of zircon and monazite during crustal melting. J. Geol. Soc. 171, 465–479. https://doi.org/10.1144/jgs2013-115

Závada, P., Schulmann, K., Racek, M., Hasalová, P., Jeřábek, P., Weinberg, R.F., Štípská, P., Roberts, A., 2018. Role of strain localization and melt flow on exhumation of deeply subducted continental crust. Lithosphere 10, 217–238. https://doi.org/10.1130/L666.1

Figures captions

(2 columns)

Fig. 1. Geological map of the West African Craton, modified after Milési et al. (2004), and Block et al. (2015). Abbreviations: SGGC = Sidéradougou Gneiss-Granitoid Complex, Si = Sidéradougou gneiss-granitoid complex. Ba = Banfora greenstone belt, Di = Diebougou gneiss-granitoid complex, Ho= Hounde greenstone belt, KT= Koudougou-Tumu gneiss-granitoid complex, OFSZ = Ouango-Fitini shear zone. The red rectangle indicates the studied zone.

(2 columns)

Fig. 2. Lithostructural map of the Mangodara district; the south-east part of the map is reinterpreted from data of Hirdes et al. (1996). Lithofabrics are delineated from interpretation of fabrics measured on the field, aerial photographs (Google Earth) and remote sensing imagery (LANDSAT-8, Sentinel-2). Magnetic lineaments are extracted from aeromagnetic data (SYSMIN), and served for interpretation of shear zones, using the method proposed by (Chardon et al., 2020). Emplacement of named samples in this paper are indicated in the map. Markers used in chemical element diagrams are presented in the legend next to their related lithology. Supplementary U-Pb ages in the south-east part of the map are extracted from Hirdes et al. (1996).

(2 columns)

Fig. 3. Field photographs of granodioritic gneiss and associated migmatites. (a) Banded layer in a granodioritic gneiss. (b) Granodioritic gneiss showing augen texture. (c) Gabbroic and microgranular

enclaves in a granodioritic gneiss. (d) Layered granodioritic gneiss containing leucosomes connected to garnet-REE pegmatite dyke (station BB24, See also Fig. 11). (e) Ptygmatitic veins in a granodioritic gneiss (east of Gountiedougou). (f) Enclave of granodioritic gneiss in the tonalitic-trondhjemitic gneiss. Leucosomes and titanite-allanite pegmatite are visible (station BMN37).

(2 columns)

Fig. 4. (a) Granolepidoblastic texture in the granodioritic gneiss (station BMN24). The foliation is marked by alignment of biotite laths. Eye-shaped plagioclase and hornblende are surrounded by biotite and mark the granoblastic texture. (b) Mafic hornblende-biotite-epidote assemblage, stretched in an S-C fabric. Recrystallized quartz is located in the margin of the ferromagnesian minerals, and distributed with preferential orientation along the C direction. Clastic plagioclase and recrystallized quartz suggest solid-state deformation, under high temperature. Abbreviations: Ap = apatite, Aln = allanite, Bt = biotite, Ep = epidote, Hbl = hornblende, Pg = plagioclase, Ttn = titanite.

(2 columns)

Fig. 5. Field photographs and optical photomicrographs of amphibolite and schist. (a) Amphibolite (station BMN109). (b) Schists intercalated with hornblende-rich layers, intruded by a thin granitic sill (station 1688). (c) Optical photomicrograph of a hornblende-bearing leucocratic vein in amphibolite, with gradual accumulation of hornblende crystals in the margin. (d) Photomicrograph of a hornblende schist (station 1989, near 1984). The mineralogical assemblage consists of rods of hornblende porphyroblasts in a groundmass of quartz, plagioclase and biotite. Abbreviations: Bt = biotite, Hbl = hornblende.

(2 columns)

Fig. 6. Field photographs of paragneiss. (a) Garnet and staurolite bearing paragneiss showing schistosity and crenulation, hosting a pseudo-boudin of a garnet-columbite pegmatite dyke, parallel to S_n schistosity and pinched in the S_{n+1} crenulation plan. (b) Paragneiss showing thin crenulated leucosomes and small pockets filled with quartz and feldspars. (c) and (d) Photomicrographs of a paragneiss (station BMS49). The axial crenulation S_{n+1} is printed in the internal texture of staurolite porphyroblasts. The garnet porphyroblast shown exhibits synkinematic helicitic texture in the core and homogeneous rims. Fibrous sillimanite is associated with biotite sheets. Abbreviations: Bt = biotite, Gr = garnet, Mu = muscovite, Qtz = quartz, Sil = sillimanite, St = staurolite.

(2 columns)

Fig. 7. Field photographs of metatexitic paragneiss and granodioritic gneiss boarding the tonalitic-trondhjemitic gneiss. (a) Stromatic migmatitic paragneiss (near station BMS37). (b) Transition between a migmatitic paragneiss (melanocratic layers and leucosomes) and granodioritic gneiss, foliated granodiorite gneiss bearing garnet-columbite pegmatites pods (near BMS37). (c) Migmatitic paragneiss with melanocratic layers (richer in biotite, hosting leucosomes), grading to granodioritic gneiss, are deformed by a melt rich (quartz + feldspar) shear zone (station BMS140; compass for scale). (d) Garnet porphyroblasts in a migmatitic paragneiss, associated with patchy leucosomes (near BMS7B). (e) Synmigmatitic foliation in a migmatitic paragneiss. Quartz-feldspar-rich layers are leucosomes. Near-homogeneous garnet included or in contact in the leucosomes is interpreted as the peritectic product of a partial melting reaction. Staurolite crystals in mesosomes are wrapped by micas and quartz. (f) Migmatitic paragneiss, composed of quartz, feldspar, inclusion-rich porphyroblastic garnet surrounded by biotitic foliation, biotite and sillimanite. Abbreviations: Bt = biotite, Gr = garnet, Sil = sillimanite, St = staurolite.

(2 columns)

Fig. 8. Field photographs of the tonalitic-trondhjemitic gneiss. (a) Biotite and magnetite leucotonalitic facies, crossed by a leucocratic vein containing mafic clots (hornblende, biotite and magnetite) (station BMN11). (b) Mesocratic enclave, hosting deformed leucocratic veins in textural continuity with the tonalitic mesostase. (c) Schollen-like texture in gneissic facies of the tonalitic-trondhjemitic gneiss. Mesocratic rafts are traversed by a hornblende tonalite vein (station BMS124). (d) Hornblende tonalite veins parallel to foliation are affected by folding. Transverse veins circulate next to axial plan of folds (station BMN11; compass in foreground for scale). (e) Mafic clots of poikilitic assemblage of biotite and hornblende, exposed as pseudomorphs of minerals with hexagonal basal section (hornblende); head of rock hammer for scale.

(2 columns)

Fig. 9. Polarized photomicrographs of the tonalitic-trondhjemitic gneiss. a) The image is dominated by subhedral oligoclase showing diffuse contacts, suggestive of slow cooling, and connected by triple joints. Anhedral oligoclase shows well-developed polysynthetic twins. Recrystallized quartz corrodes plagioclase grain borders, which might correspond to liquid product from plagioclase consumption. (b) Batches of recrystallized quartz corrode the plagioclase grain in the center of the picture, whereas melt is trapped between plagioclase grains in the lower part. Abbreviations: Bt= biotite, Ep = epidote, Pg = plagioclase, Qtz = quartz.

(2 columns)

Fig. 10. Field photographs of plutonic rocks from Mangodara district. (a) Layered GG-granitoid, with mesocratic layers and K-feldspar-rich leucocratic layers. (b) Disrupted blocks of gabbro in an intrusive pink granite (GG-granitoid). (c) Porphyritic biotite granite, with megacrysts of K-feldspar (GG-granitoid). (d) Hornblende-biotite granodiorite, bearing elongated mica-rich enclaves (station BMS23). (e) Two-mica granite enclosing rounded enclaves of tonalitic-trondhjemitic gneiss (station BMS9).

(2 columns)

Fig. 11. Field photographs of pegmatite veins and their relationships with their host rocks. (a) Network of interconnected veins of titanite-allanite pegmatite in tonalitic-trondhjemitic gneiss. (b) Garnet-columbite pegmatite vein cross-cutting apatite-zircon pegmatite (station BMS99A). (c) Rotated and pinched pods of garnet-columbite pegmatite in a layered granodioritic gneiss (near station BMS37). (d) Folded and pinched garnet-columbite pegmatite vein, with well-developed quartz core. (e) Cuspate interfaces between the paragneiss and a garnet-columbite pegmatite dyke. (f) Garnet-REE pegmatite connected with leucosomes layers veins in a granodioritic gneiss (station BB24). (g) Garnet-REE pegmatite veins in porphyritic granodioritic gneiss, deformed by thin mylonites crossing dyke, or bordering the contact with the granodioritic gneiss (near station BB15).

(2 columns)

Fig. 12. (a) and (b) Contact between apatite-zircon pegmatite (section with biotite) and garnet-columbite pegmatite (section rich in muscovite and hosting garnet). Abbreviations: Bt = biotite, Gr = garnet, Mu = muscovite.

(1 columns)

Fig. 13. Metamorphic conditions prevailing in the Mangodara district. Volcanic belts greenschist facies paragenesis is taken from Ilboudo et al., (2017b). Legend as in Fig. 2. Abbreviations: Bt = biotite, Gr = garnet, Hbl = hornblende, Ky = kyanite, Mu = muscovite, Sil = sillimanite, St = staurolite.

(2 columns)

Fig. 14. (a) Calculated P-T pseudosection for sample BMS114B in the NCKFMASHTO system. The light blue field represents the subsolidus stability domain of aqueous fluid (H_2O). The dark blue field represents the suprasolidus field in presence of a silicate melt. Ilmenite was stable in all parts of the computed pseudosection. The dashed line indicates the representative mineral assemblages of paragneisses from Mangodara district, inferred from the mineralogy of sample BMS114B and mineralogical observations (e.g. Fig. 6). (b) Calculated P-T pseudosection for sample BMN109 in the NCFMASHTO system. Field are colored as indicated in (a). (c) and (d) Variation of mineral volume fractions between 500 °C and 700 °C at a pressure of 7 kbar, in paragneiss and amphibolite. Abbreviations: bt = biotite, chl = chlorite, cord = cordierite, cpx = clinopyroxene, ilm = ilmenite, gr = garnet, hbl = hornblende, kfs = K-feldspar, ky = kyanite, liq = silicate melt, mu = muscovite, opx = orthopyroxene, pg = plagioclase, qtz = quartz, sil = sillimanite, st, = staurolite.

(2 columns)

Fig. 15. U-Pb chronological data obtained on zircons from the titanite-allanite type pegmatite BMN28. (a) Cathodoluminescence images of two zircon grains analyzed. Circles locate the analyzed spots, the red color designating discordant data, whereas yellow indicates concordant data. (b-c) Discordia and Concordia diagrams, respectively. The size of the ellipses represents an uncertainty of 2 sigma. The ellipse color indicates the textural position of the analyses: blue for the core, orange for the rim.

(2 columns)

Fig. 16. U-Pb chronological data obtained on apatite. Cathodoluminescence images of apatite in (a) granodioritic gneiss (BMN20B), (b) tonalitic-trondhjemitic gneiss (BMN11) and (c) apatite-zircon type pegmatite (BMN20). Red circles indicate the emplacements of the analyzed spots. Tera-Wasserburg diagram plotting U-Pb isotopic data from apatite in (d) granodioritic gneiss (BMN20B), (e) tonalitic-trondhjemitic gneiss (BMN11) and (f) apatite-zircon-type pegmatite (BMN20).

(2 columns)

Fig. 17. REE spider diagram of (a) amphibolite, micaschist, and paragneiss, (c) gneisses and granitoids and (e) pegmatites normalized to chondrite (McDonough and Sun, 1995). Multi-elements spider diagram of (b) amphibolite, micaschist and paragneiss, (d) gneisses and granitoids, and (f) pegmatites normalized to primitive mantle (Sun and McDonough, 1989). Filled patterns correspond to granodioritic gneiss (blue), tonalitic-trondhjemitic gneiss (pink) and calc-alkaline basalt (green) from the Hounde greenstone belt, and Tiébélé greenstone belt (Baratoux et al., 2011; Ilboudo et al., 2017a).

(2 columns)

Fig. 18. Geochemical discriminant diagrams for gneisses and plutonic rocks. (a) Chemical index alteration (CIA = Al_2O_3 / (Al_2O_3 + CaO + Na_2O + K_2O)*100, CaO* corresponding to amount of Ca incorporated in silicates, considering the apatite component (Nesbitt and Young, 1982, 1984). (b) Shand index plot (Shand, 1943) showing most of the gneiss and granitoids in the metaluminous domain. (c) Diagram of SiO2 vs K_2O (Peccerillo and Taylor, 1976) including domains corresponding to plagioclase and amphibole accumulation (in shades of gray, Laurent et al., 2020). (d) Quartz-alkali felspar-plagioclase (QAP) diagram for felsic gneisses and granitoids (Streckeisen and Le Maitre, 1979). Modal compositions are calculated in CIPW norm and validated by comparison with mineral compositions of corresponding samples. (e) Total alkali-silica diagram (SiO2 vs Na_2O + K_2O, Cox et al., 1979). (f) Diagram plotting Sr/Y vs La/Yb also showing domains of high-, middle- and low-pressure TTG, according to Moyen, (2011). (g, h) Binary ratio plots depicting K/Rb versus Ca/Cs and Nb/Ta versus Zr/Hf for gneisses, granitoids and pegmatites, respectively.*

(2 columns)

Fig. 19. Cross-section representing the structural setting of the Mangodara dome, cored by tonalitic-trondhjemitic gneiss and flanked by two shear zones. Plutonic rocks, from the left to the right, represent respectively the hornblende-biotite granodiorite, the two-mica tonalite and the GG-granitoids intruded by porphyritic biotite granite. The mantling granodioritic gneiss represent a diatexite including rafts of partially molten Birimian volcano-sedimentary amphibolite-schist and paragneiss. Plutonic rocks are formed by melt collected within the gneiss, and pegmatites are formed by melt segregation in the gneisses and the rafts of migmatitic paragneiss-amphibolite.

(2 columns)

Fig. 20. Recapitulative interpretation of the petrogenetic relationships among amphibolites, schists, paragneiss, gneisses, plutonic rocks and pegmatites in the Mangodara district.

Figures

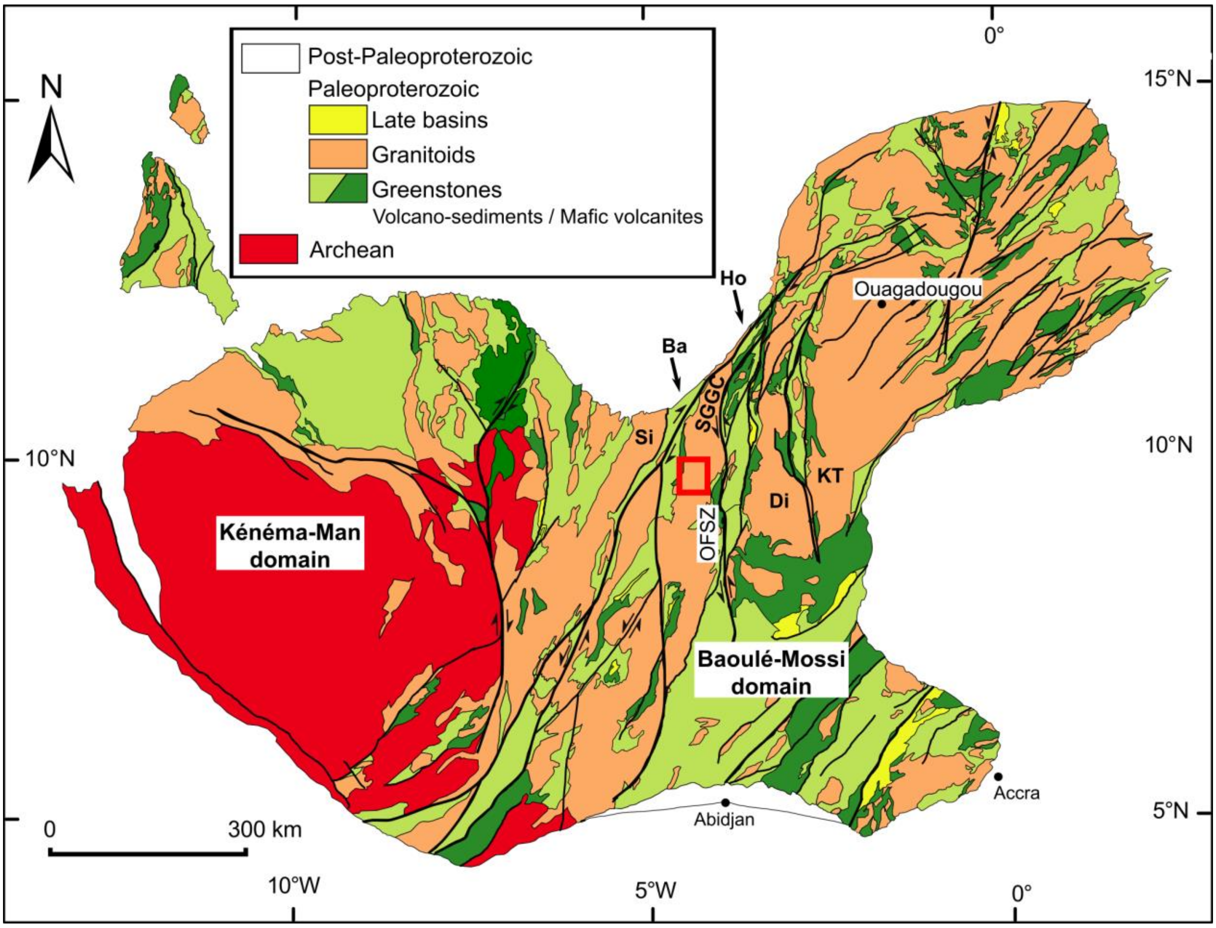

Post-Paleoproterozoic
Paleoproterozoic
Late basins
Granitoids
Greenstones
Volcano-sediments / Mafic volcanites
Archean
N
0°
15°N
10°N
5°N
10°W
5°W
0
300 km
Ho
Ba
Si
SGGC
OFSZ
Di
KT
Ouagadougou
Kénéma-Man domain
Baoulé-Mossi domain
Abidjan
Accra

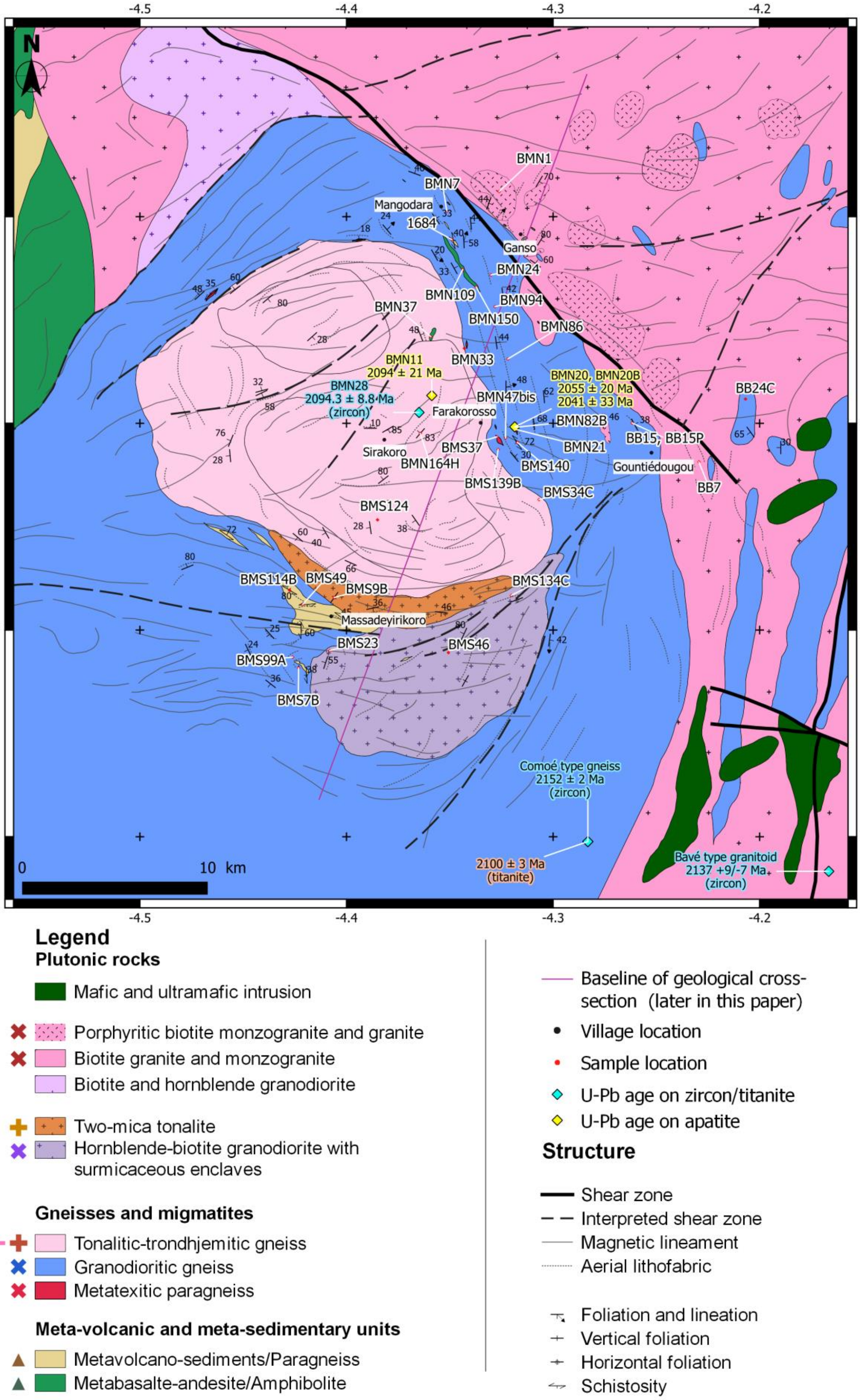

-4.5
-4.4
-4.3
-4.2
9.9
9.8
9.7
9.6
N
BMN1
BMN7
Mangodara
1684
Ganso
BMN24
BMN109
BMN94
BMN37
BMN150
BMN86
BMN33
BMN11
2094 ± 21 Ma
BMN28
2094.3 ± 8.8 Ma
(zircon)
BMN20, BMN20B
2055 ± 20 Ma
2041 ± 33 Ma
BMN47bis
Farakorosso
BMN82B
BB24C
BB15, BB15P
BMN21
Sirakoro
BMS37
BMN164H
BMS140
Gountiédougou
BMS139B
BB7
BMS34C
BMS124
BMS114B
BMS49
BMS9B
BMS134C
Massadeyirikoro
BMS23
BMS46
BMS99A
BMS7B
Comoé type gneiss
2152 ± 2 Ma
(zircon)
2100 ± 3 Ma
(titanite)
Bavé type granitoid
2137 +9/-7 Ma
(zircon)
0
10 km
Legend
Plutonic rocks
Mafic and ultramafic intrusion
Porphyritic biotite monzogranite and granite
Biotite granite and monzogranite
Biotite and hornblende granodiorite
Two-mica tonalite
Hornblende-biotite granodiorite with surmicaceous enclaves
Gneisses and migmatites
Tonalitic-trondhjemitic gneiss
Granodioritic gneiss
Metatexitic paragneiss
Meta-volcanic and meta-sedimentary units
Metavolcano-sediments/Paragneiss
Metabasalte-andesite/Amphibolite
Baseline of geological cross-section (later in this paper)
Village location
Sample location
U-Pb age on zircon/titanite
U-Pb age on apatite
Structure
Shear zone
Interpreted shear zone
Magnetic lineament
Aerial lithofabric
Foliation and lineation
Vertical foliation
Horizontal foliation
Schistosity

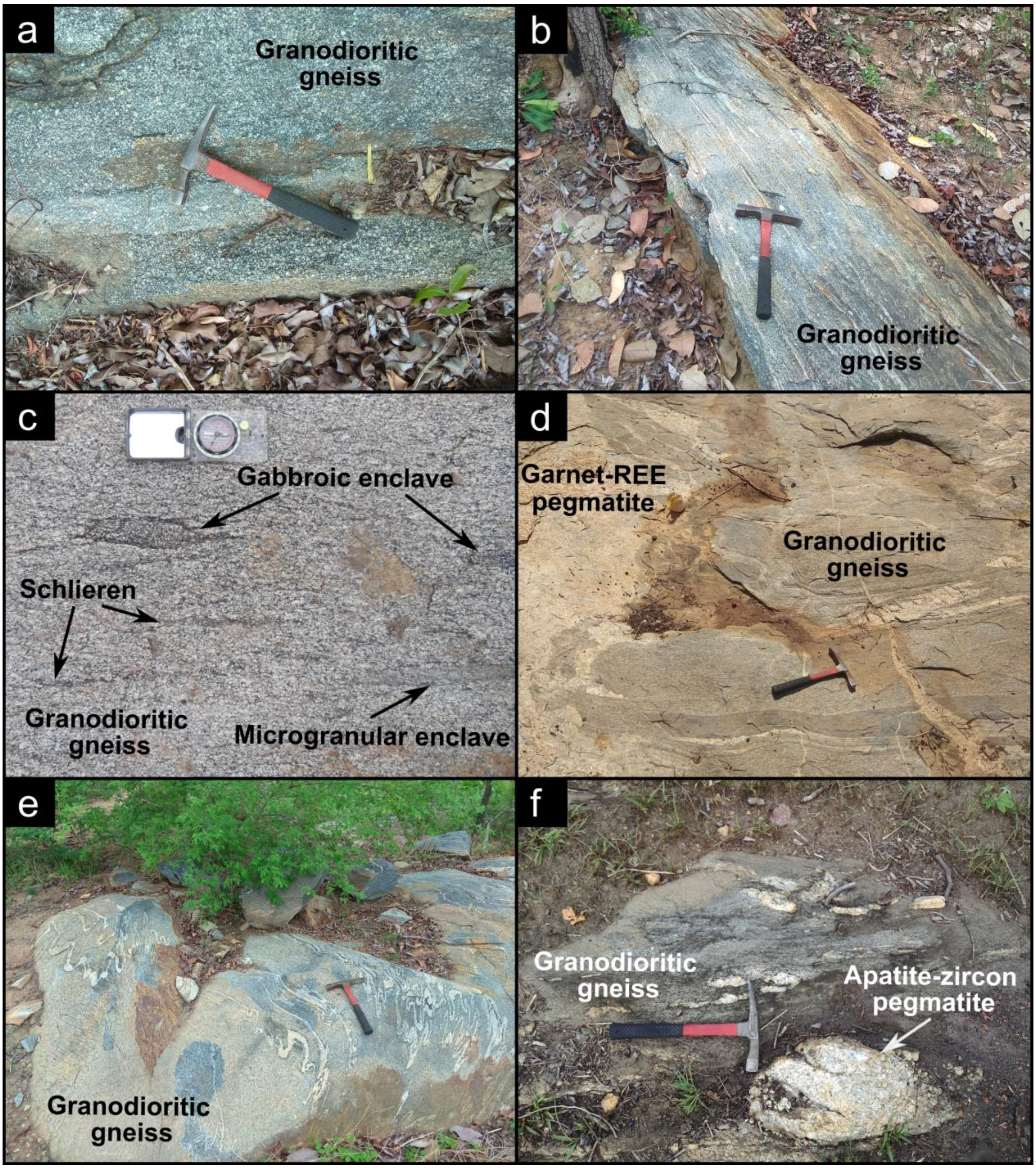
a
Granodioritic gneiss
b
Granodioritic gneiss
c
Gabbroic enclave
Schlieren
Granodioritic gneiss
Microgranular enclave
d
Garnet-REE pegmatite
Granodioritic gneiss
e
Granodioritic gneiss
f
Granodioritic gneiss
Apatite-zircon pegmatite

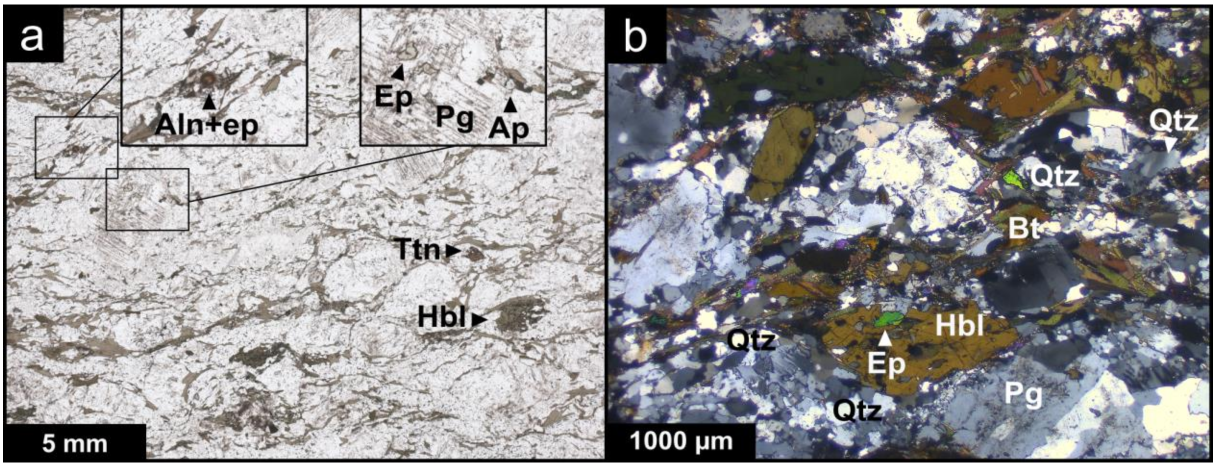
a
Aln+ep
Ep
Pg
Ap
Ttn
Hbl
5 mm
b
Qtz
Qtz
Bt
Qtz
Hbl
Ep
Qtz
Pg
1000 µm

1863 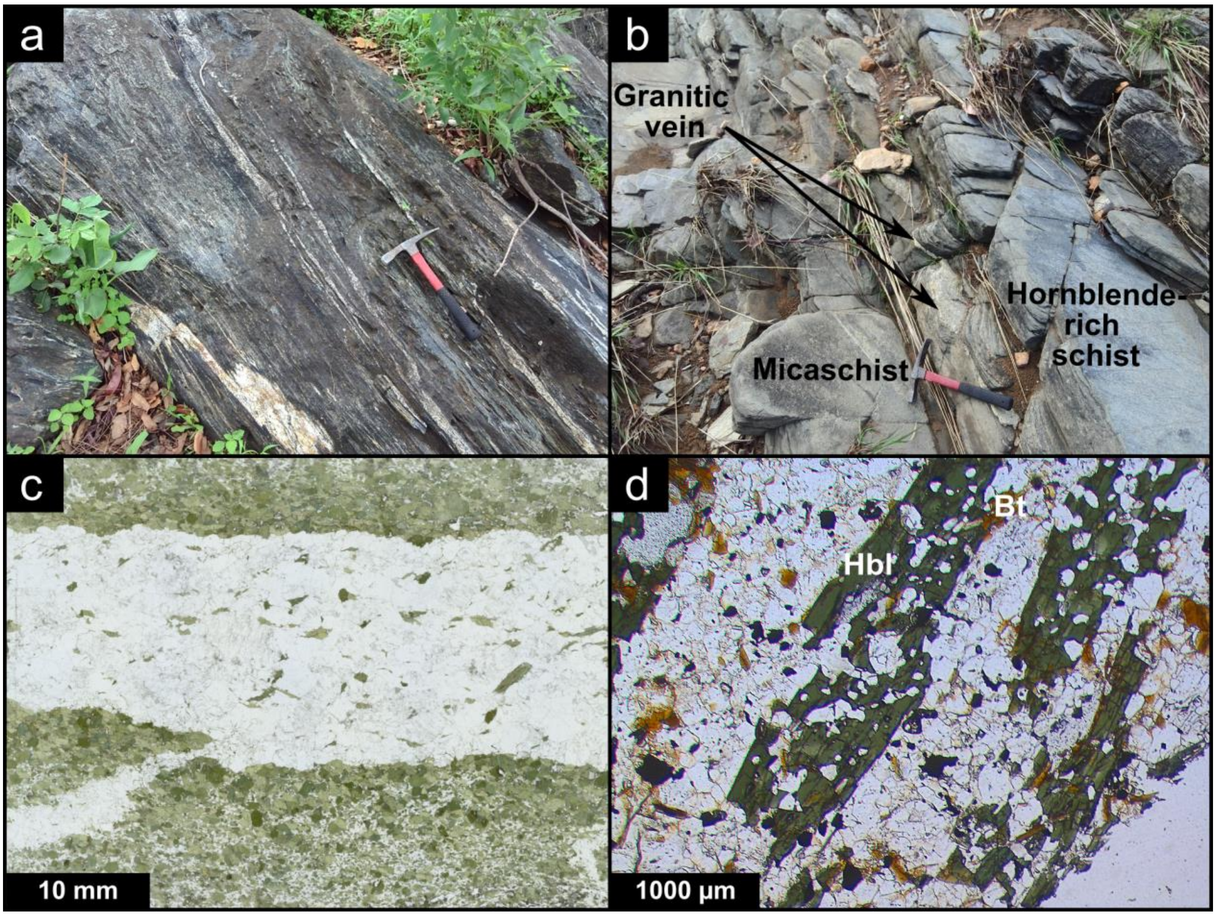
a
b
Granitic vein
Hornblende-rich schist
Micaschist
c
10 mm
d
Bt
Hbl
1000 µm

1864

1865 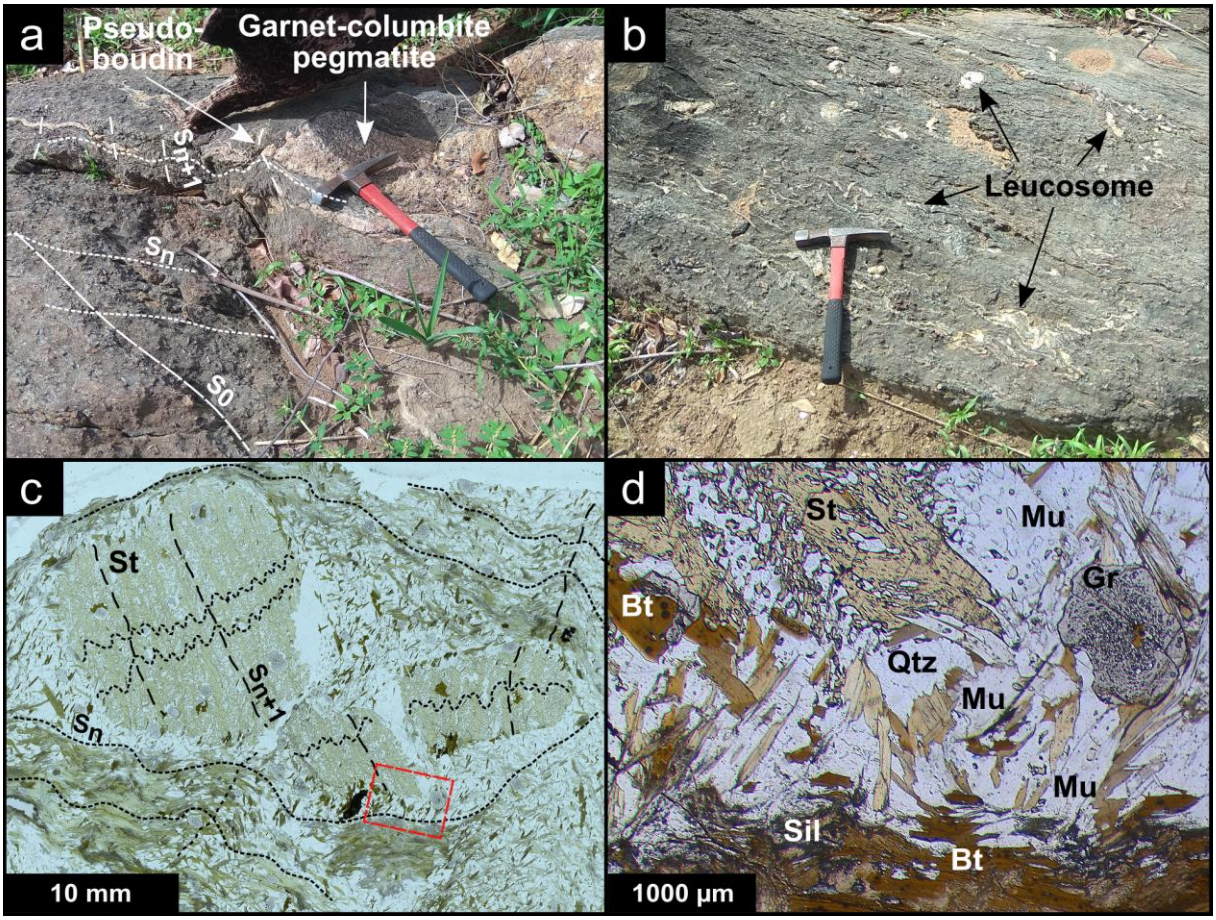
a
Pseudo-boudin
Garnet-columbite pegmatite
Sn+1
Sn
S0
b
Leucosome
c
St
Sn+1
Sn
10 mm
d
St
Mu
Gr
Bt
Qtz
Mu
Mu
Sil
Bt
1000 µm

1866

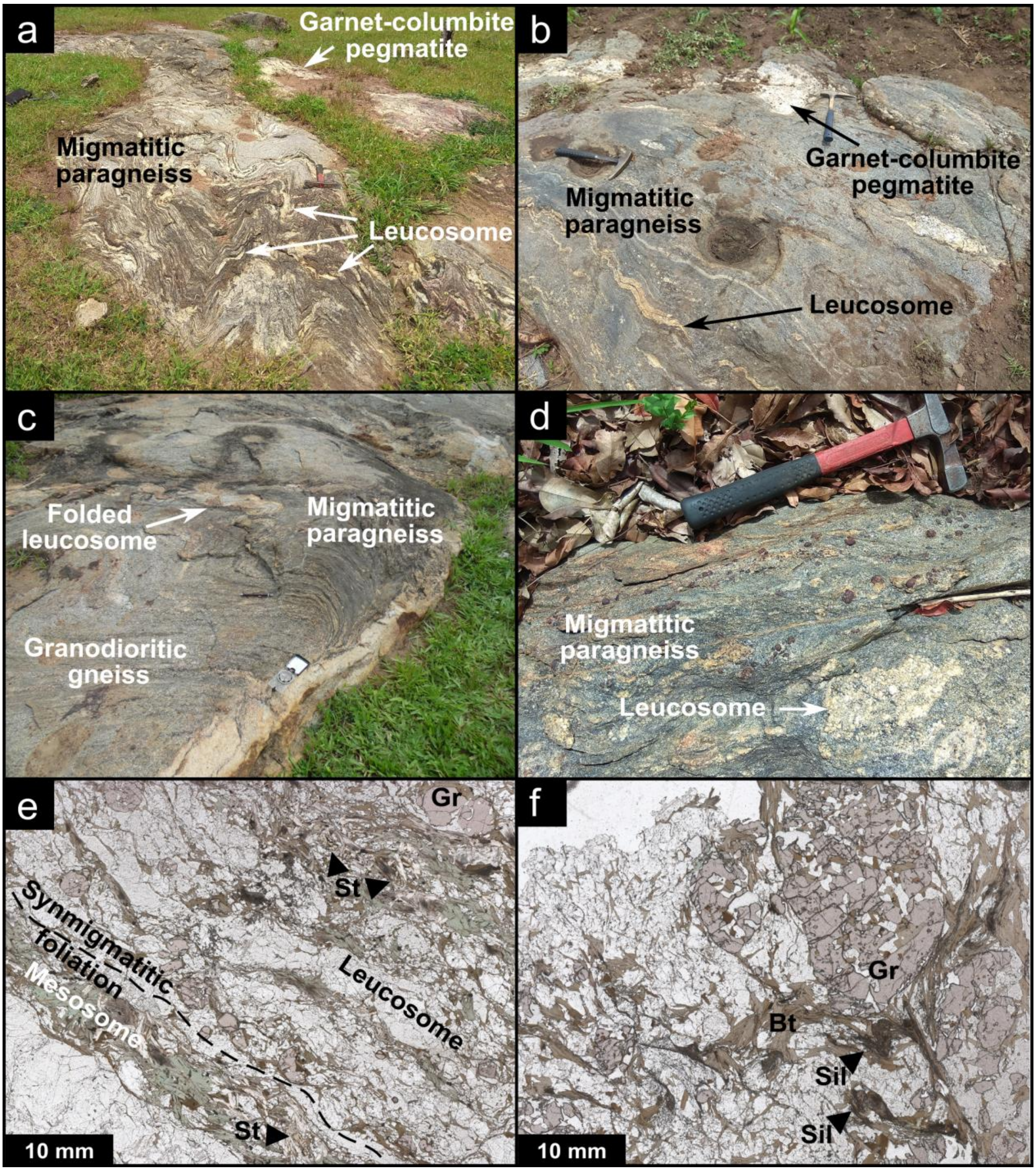
a
Garnet-columbite
pegmatite
Migmatitic
paragneiss
Leucosome
b
Garnet-columbite
pegmatite
Migmatitic
paragneiss
Leucosome
c
Folded
leucosome
Migmatitic
paragneiss
Granodioritic
gneiss
d
Migmatitic
paragneiss
Leucosome
e
Gr
St
Synmigmatitic
foliation
Mesosome
Leucosome
St
10 mm
f
Gr
Bt
Sil
Sil
10 mm

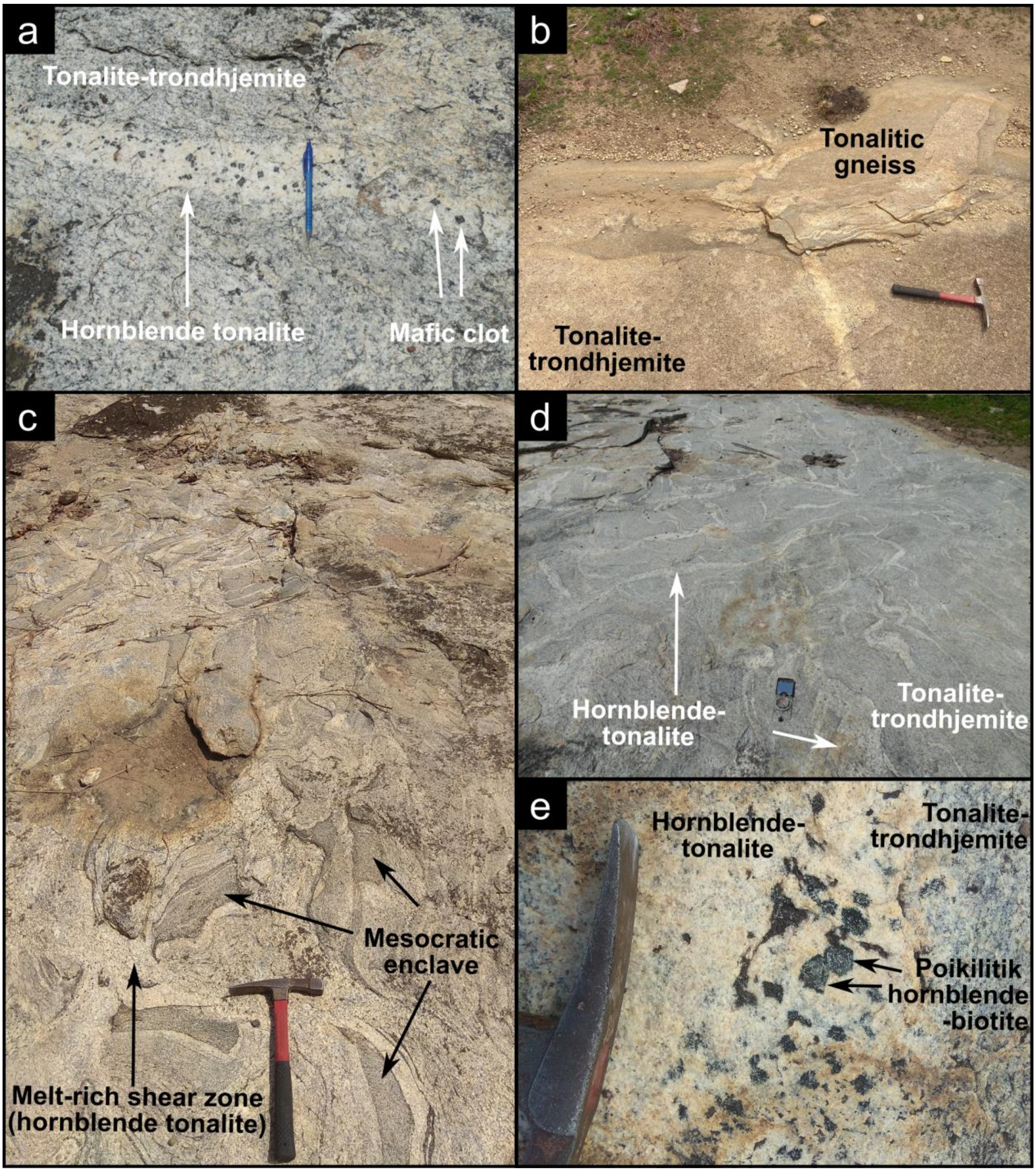
a
Tonalite-trondhjemite
Hornblende tonalite
Mafic clot
b
Tonalitic gneiss
Tonalite-trondhjemite
c
Mesocratic enclave
Melt-rich shear zone (hornblende tonalite)
d
Hornblende-tonalite
Tonalite-trondhjemite
e
Hornblende-tonalite
Tonalite-trondhjemite
Poikilitik hornblende-biotite

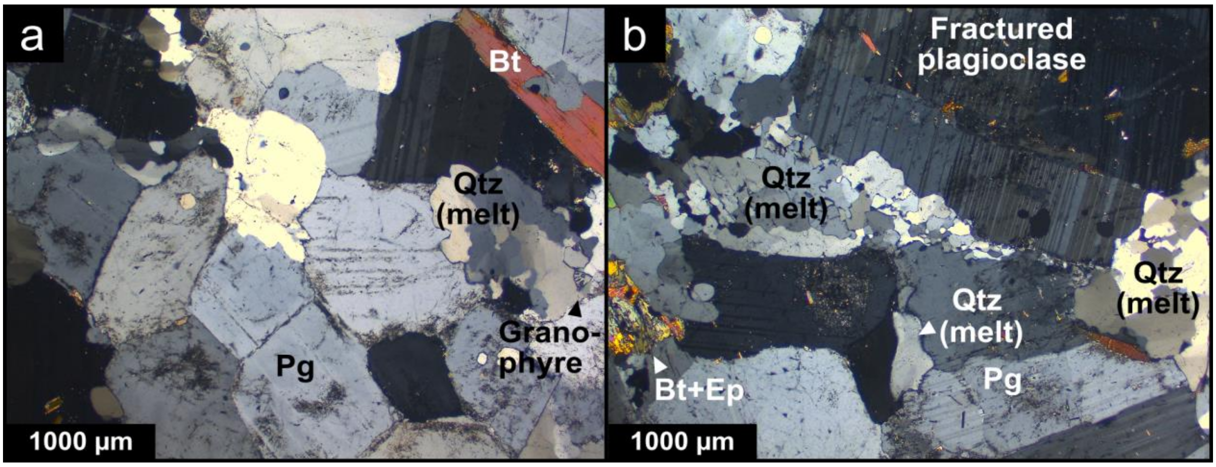
a
Bt
Qtz
(melt)
Grano-
phyre
Pg
1000 µm
b
Fractured
plagioclase
Qtz
(melt)
Qtz
(melt)
Qtz
(melt)
Pg
Bt+Ep
1000 µm

1873 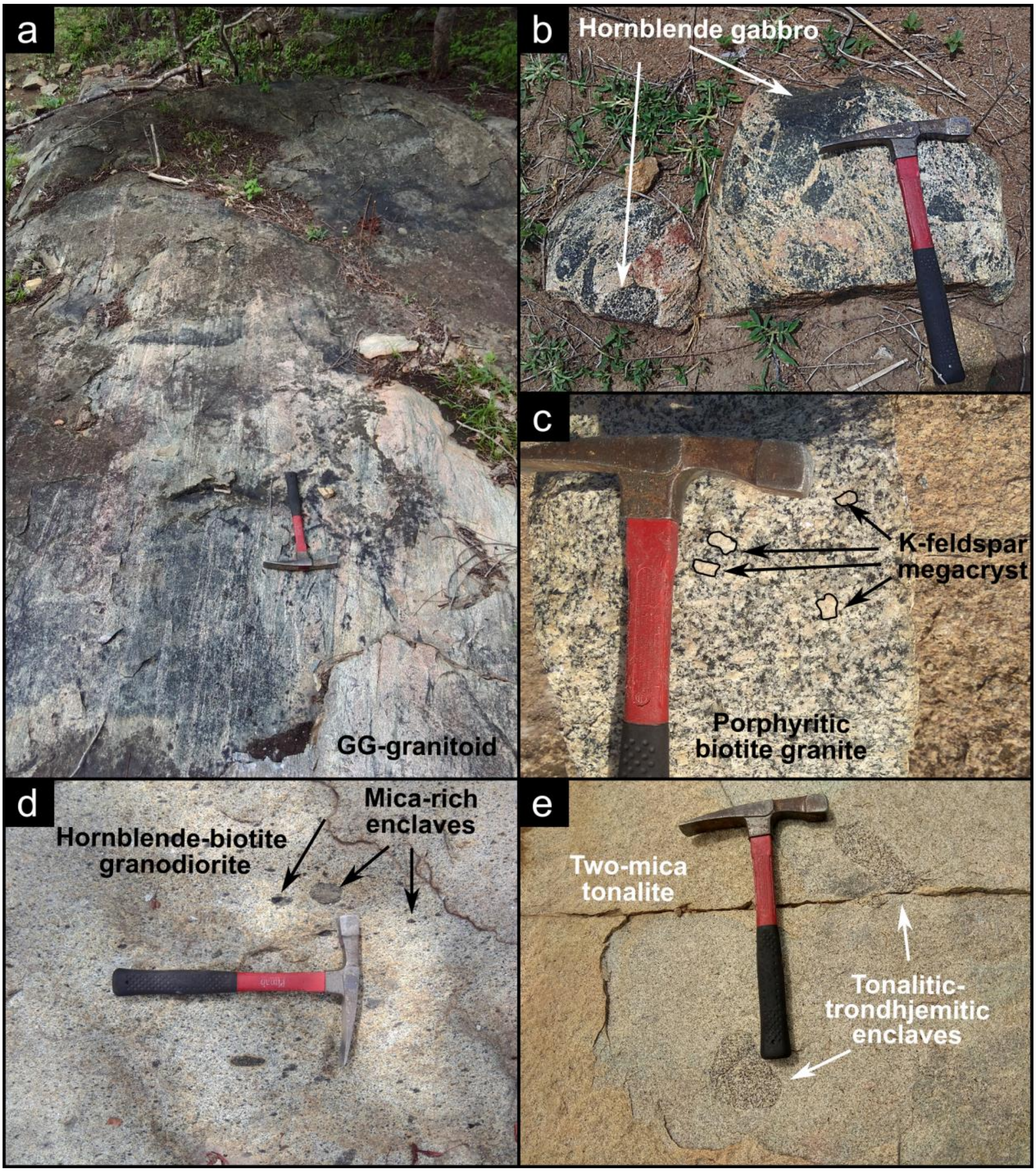
a
GG-granitoid
b
Hornblende gabbro
c
K-feldspar megacryst
Porphyritic biotite granite
d
Hornblende-biotite granodiorite
Mica-rich enclaves
e
Two-mica tonalite
Tonalitic-trondhjemitic enclaves

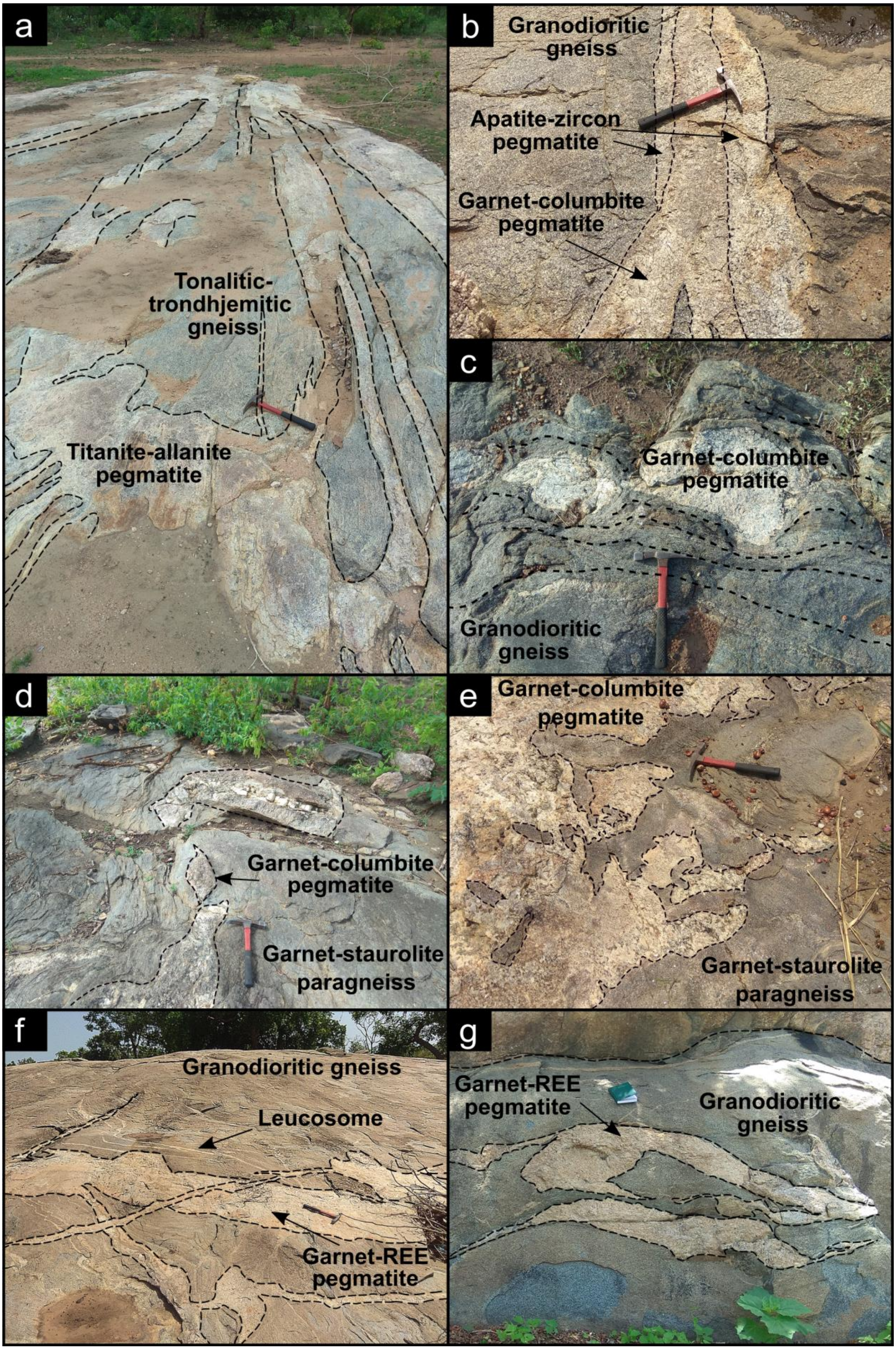
a
Tonalitic-
trondhjemitic
gneiss
Titanite-allanite
pegmatite
b
Granodioritic
gneiss
Apatite-zircon
pegmatite
Garnet-columbite
pegmatite
c
Garnet-columbite
pegmatite
Granodioritic
gneiss
d
Garnet-columbite
pegmatite
Garnet-staurolite
paragneiss
e
Garnet-columbite
pegmatite
Garnet-staurolite
paragneiss
f
Granodioritic gneiss
Leucosome
Garnet-REE
pegmatite
g
Garnet-REE
pegmatite
Granodioritic
gneiss

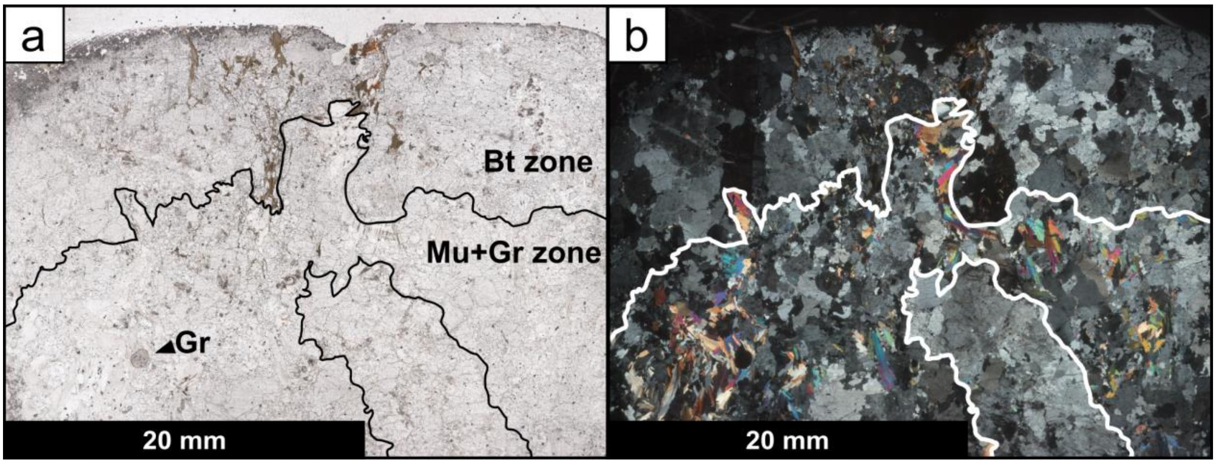
a
Bt zone
Mu+Gr zone
Gr
20 mm
b
20 mm

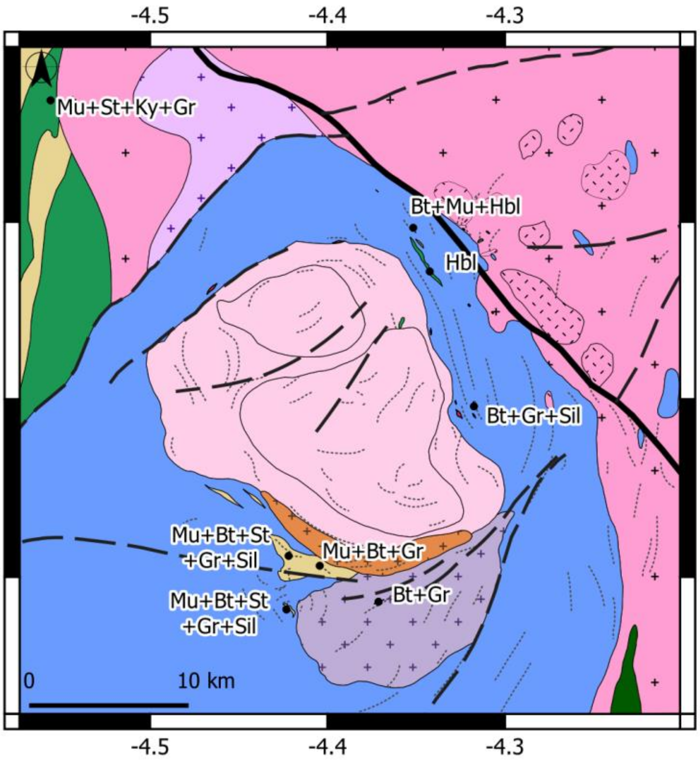
-4.5
-4.4
-4.3
9.9
9.8
9.7
Mu+St+Ky+Gr
Bt+Mu+Hbl
Hbl
Bt+Gr+Sil
Mu+Bt+St
+Gr+Sil
Mu+Bt+Gr
Mu+Bt+St
+Gr+Sil
Bt+Gr
0
10 km

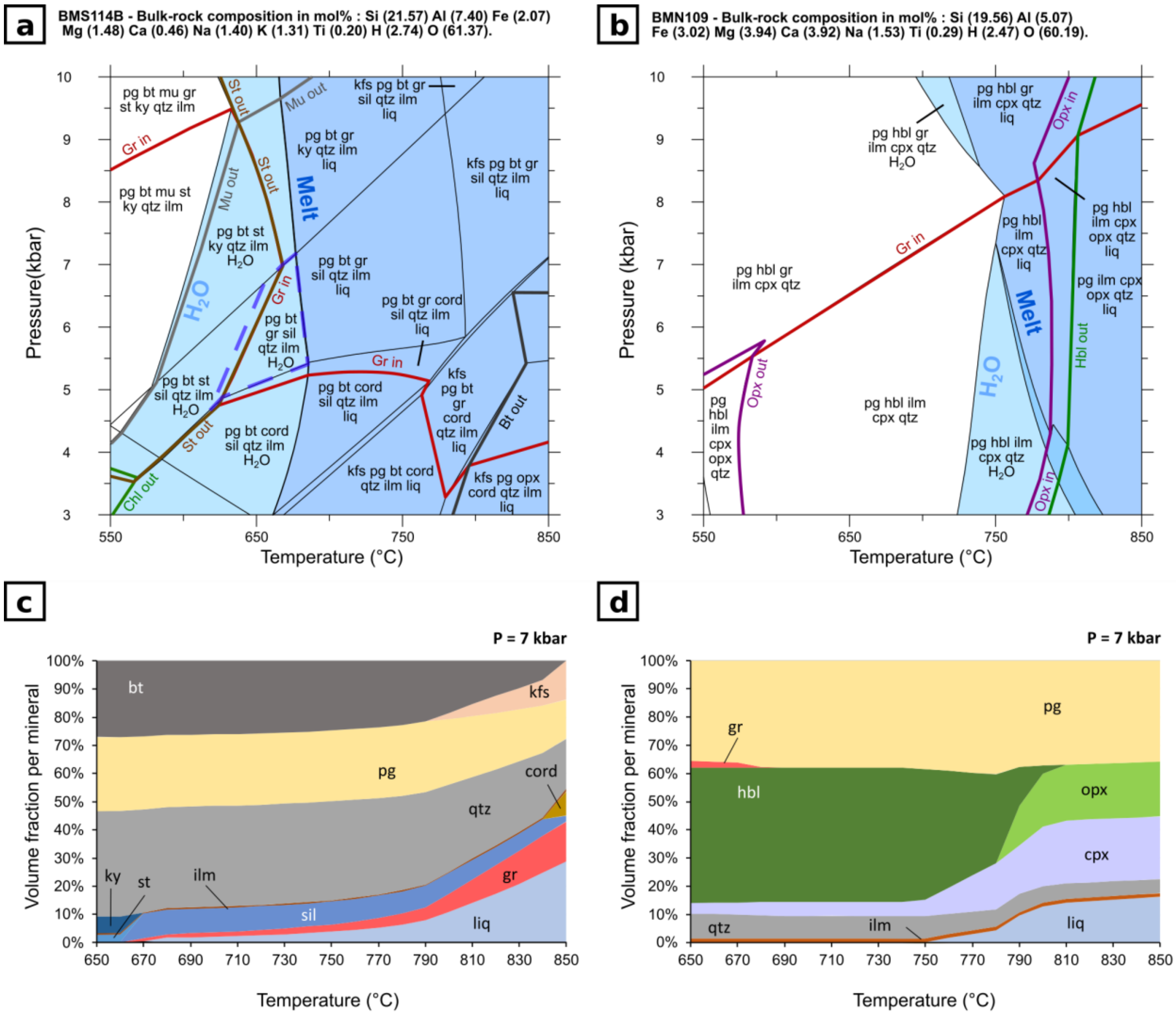
a
BMS114B - Bulk-rock composition in mol% : Si (21.57) Al (7.40) Fe (2.07) Mg (1.48) Ca (0.46) Na (1.40) K (1.31) Ti (0.20) H (2.74) O (61.37).
b
BMN109 - Bulk-rock composition in mol% : Si (19.56) Al (5.07) Fe (3.02) Mg (3.94) Ca (3.92) Na (1.53) Ti (0.29) H (2.47) O (60.19).
Pressure(kbar)
Temperature (°C)
Melt
H2O
Gr in
St out
Mu out
Chl out
Bt out
Opx in
Opx out
Hbl out
c
d
P = 7 kbar
Volume fraction per mineral
Temperature (°C)
bt
kfs
pg
qtz
cord
ky
st
ilm
sil
gr
liq
hbl
opx
cpx

1879

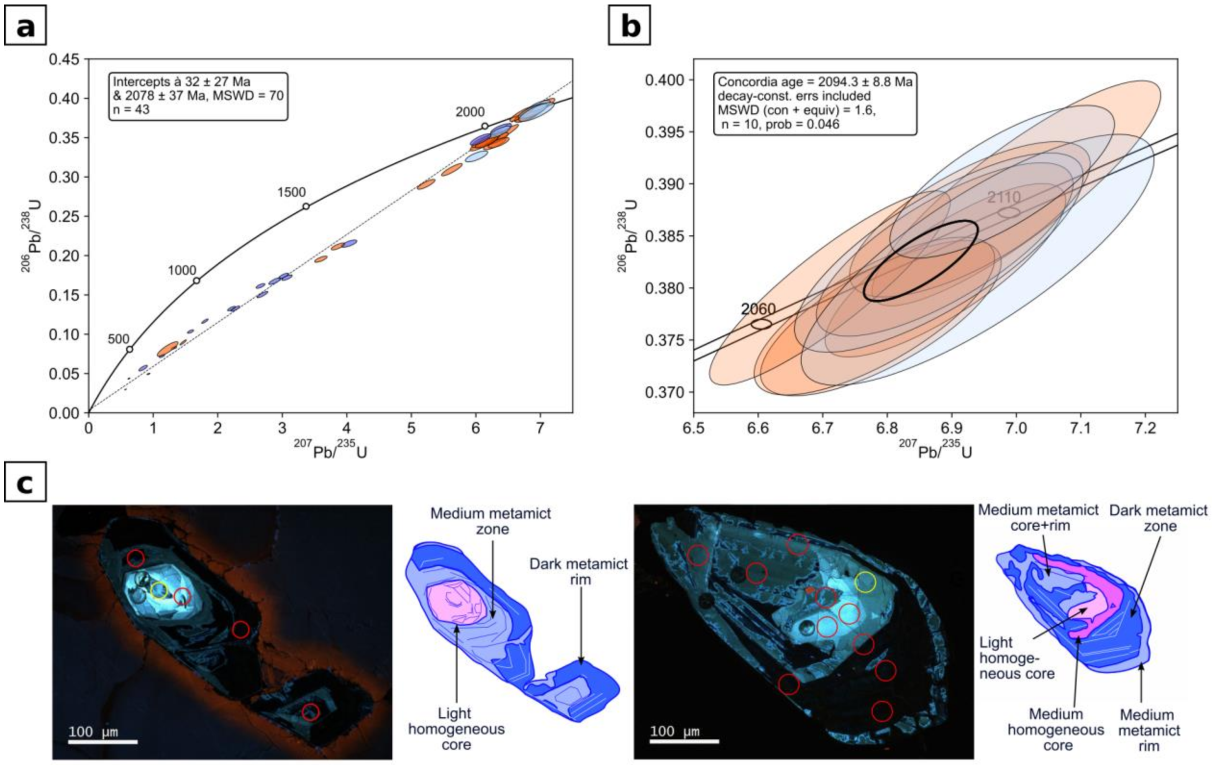
a
Intercepts à 32 ± 27 Ma
& 2078 ± 37 Ma, MSWD = 70
n = 43
500
1000
1500
2000
$^{206}Pb/^{238}U$
$^{207}Pb/^{235}U$
b
Concordia age = 2094.3 ± 8.8 Ma
decay-const. errs included
MSWD (con + equiv) = 1.6,
n = 10, prob = 0.046
2060
2110
$^{206}Pb/^{238}U$
$^{207}Pb/^{235}U$
c
100 µm
Medium metamict zone
Dark metamict rim
Light homogeneous core
100 µm
Medium metamict core+rim
Dark metamict zone
Light homoge-neous core
Medium homogeneous core
Medium metamict rim

1881

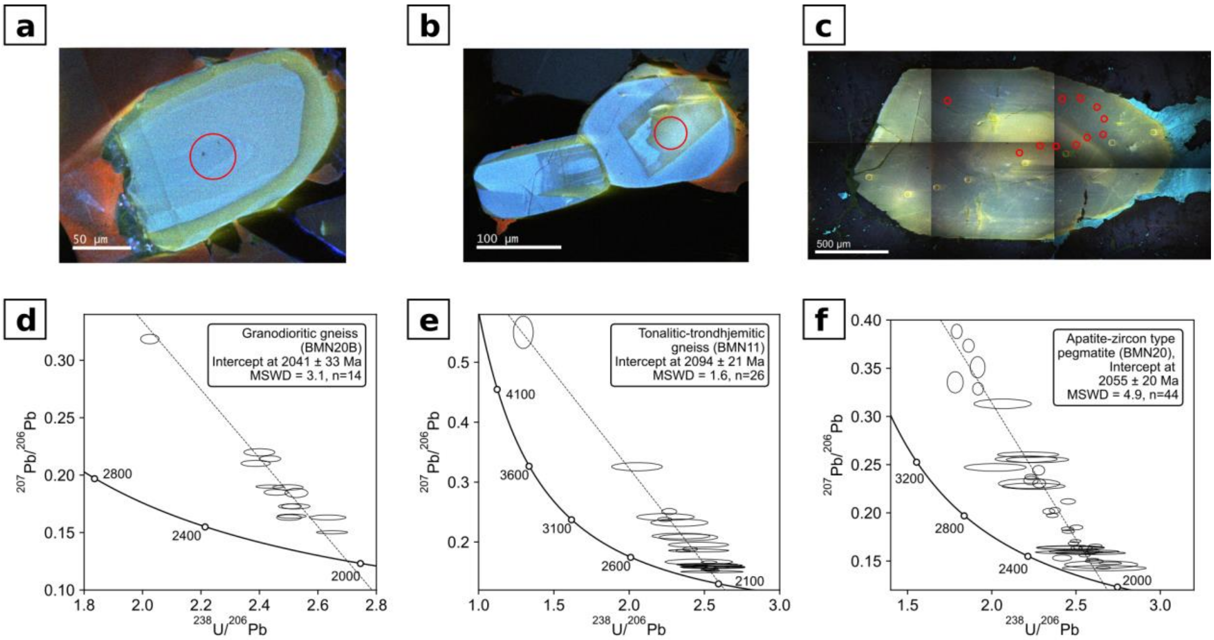

a
50 µm
b
100 µm
c
500 µm
d
Granodioritic gneiss
(BMN20B)
Intercept at 2041 ± 33 Ma
MSWD = 3.1, n=14
2800
2400
2000
e
Tonalitic-trondhjemitic
gneiss (BMN11)
Intercept at 2094 ± 21 Ma
MSWD = 1.6, n=26
4100
3600
3100
2600
2100
f
Apatite-zircon type
pegmatite (BMN20),
Intercept at
2055 ± 20 Ma
MSWD = 4.9, n=44
3200
2800
2400
2000
207Pb/206Pb
238U/206Pb

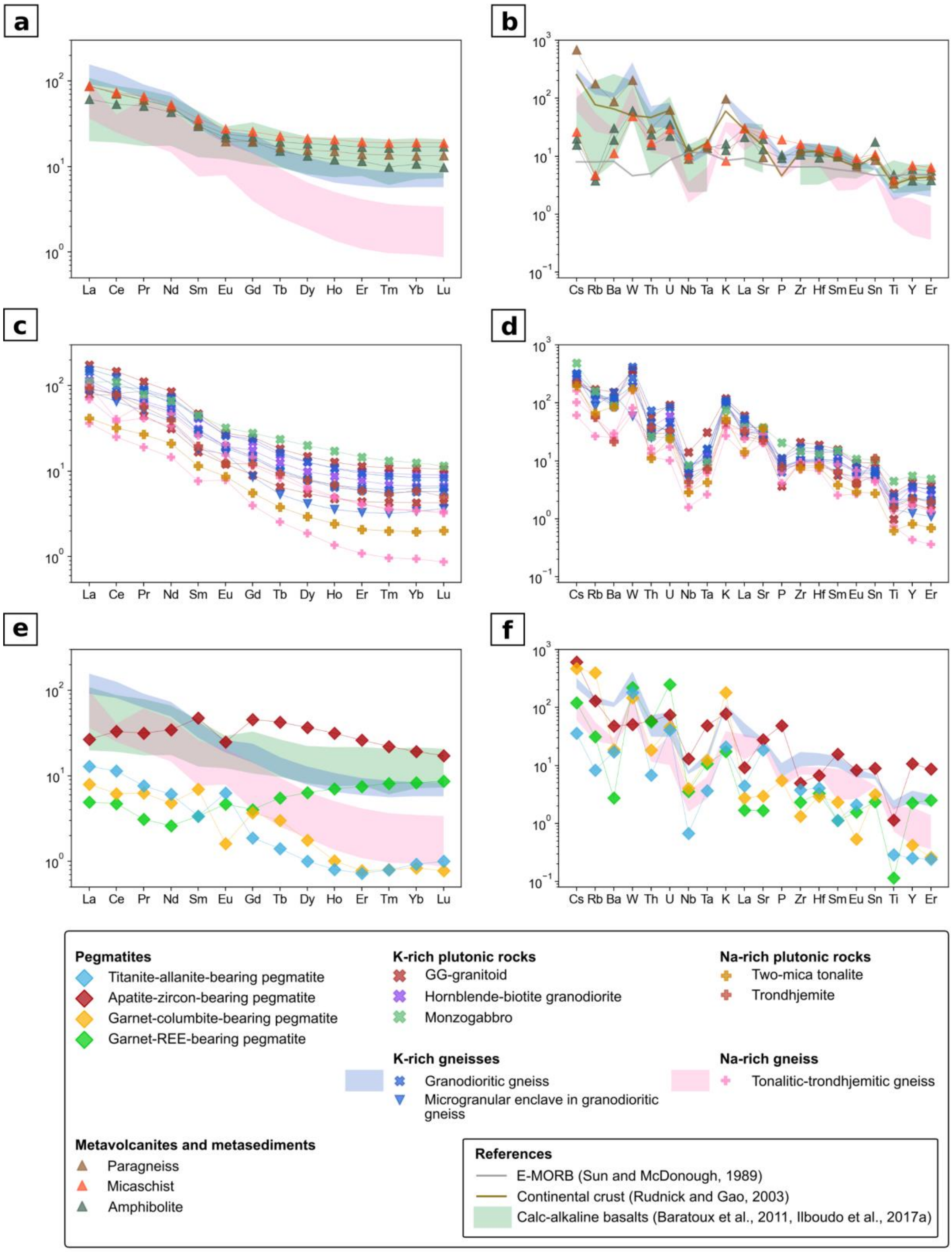

a
b
c
d
e
f
La Ce Pr Nd Sm Eu Gd Tb Dy Ho Er Tm Yb Lu
Cs Rb Ba W Th U Nb Ta K La Sr P Zr Hf Sm Eu Sn Ti Y Er
Pegmatites
Titanite-allanite-bearing pegmatite
Apatite-zircon-bearing pegmatite
Garnet-columbite-bearing pegmatite
Garnet-REE-bearing pegmatite
K-rich plutonic rocks
GG-granitoid
Hornblende-biotite granodiorite
Monzogabbro
Na-rich plutonic rocks
Two-mica tonalite
Trondhjemite
K-rich gneisses
Granodioritic gneiss
Microgranular enclave in granodioritic gneiss
Na-rich gneiss
Tonalitic-trondhjemitic gneiss
Metavolcanites and metasediments
Paragneiss
Micaschist
Amphibolite
References
E-MORB (Sun and McDonough, 1989)
Continental crust (Rudnick and Gao, 2003)
Calc-alkaline basalts (Baratoux et al., 2011, Ilboudo et al., 2017a)

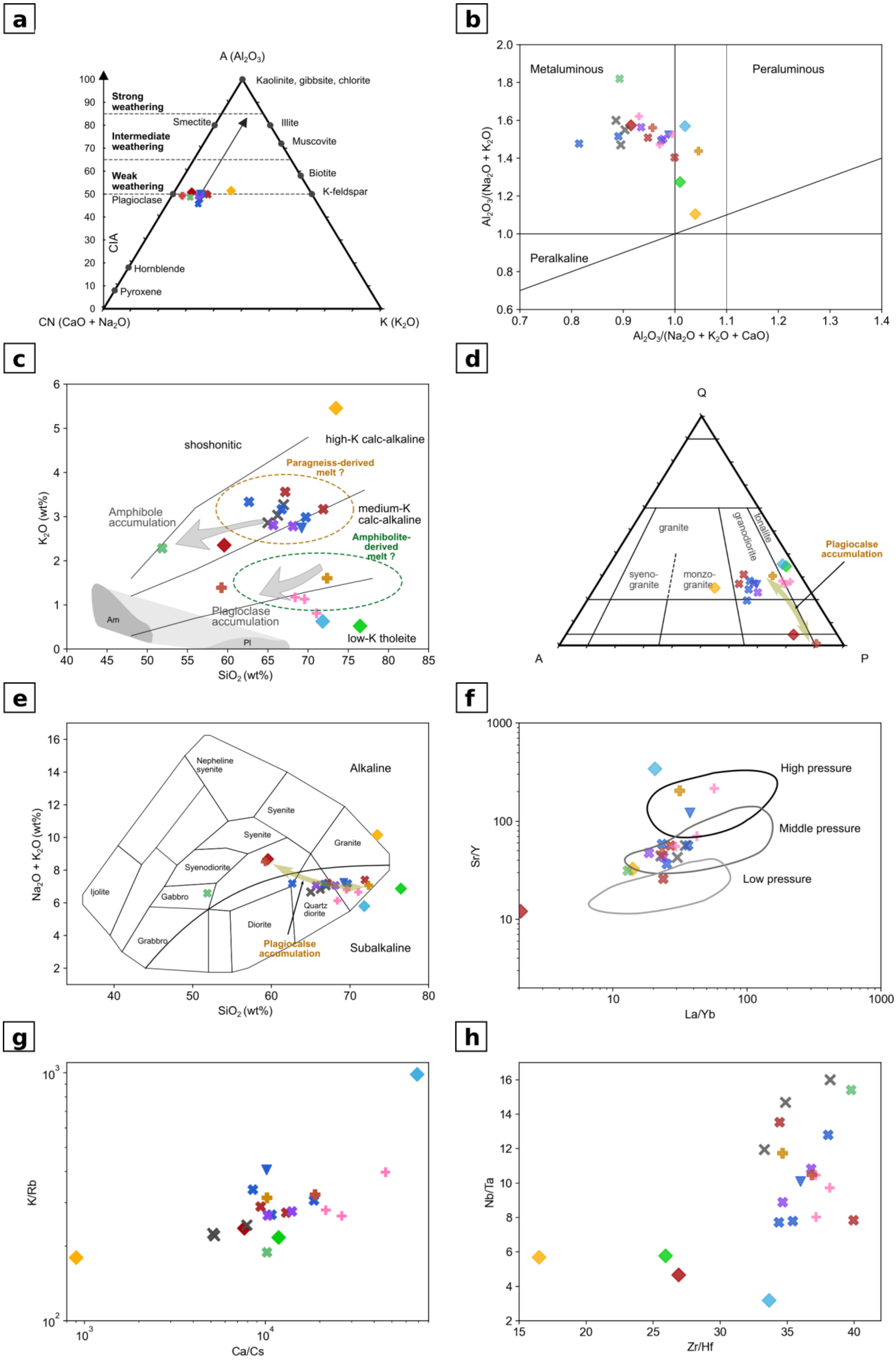
a
A (Al$_2$O$_3$)
Kaolinite, gibbsite, chlorite
Strong weathering
Smectite
Illite
Muscovite
Intermediate weathering
Weak weathering
Biotite
K-feldspar
Plagioclase
CIA
Hornblende
Pyroxene
CN (CaO + Na$_2$O)
K (K$_2$O)
b
Metaluminous
Peraluminous
Peralkaline
Al$_2$O$_3$/(Na$_2$O + K$_2$O)
Al$_2$O$_3$/(Na$_2$O + K$_2$O + CaO)
c
shoshonitic
high-K calc-alkaline
Paragneiss-derived melt ?
medium-K calc-alkaline
Amphibole accumulation
Amphibolite-derived melt ?
Plagioclase accumulation
low-K tholeite
Am
Pl
K$_2$O (wt%)
SiO$_2$ (wt%)
d
Q
granite
granodiorite
tonalite
syeno-granite
monzo-granite
Plagiocalse accumulation
A
P
e
Nepheline syenite
Alkaline
Syenite
Syenite
Granite
Syenodiorite
Ijolite
Gabbro
Quartz diorite
Diorite
Grabbro
Plagiocalse accumulation
Subalkaline
Na$_2$O + K$_2$O (wt%)
SiO$_2$ (wt%)
f
High pressure
Middle pressure
Low pressure
Sr/Y
La/Yb
g
K/Rb
Ca/Cs
h
Nb/Ta
Zr/Hf

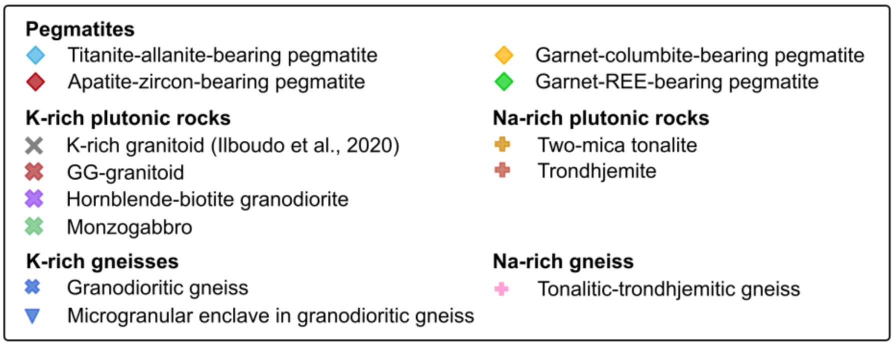
Pegmatites
Titanite-allanite-bearing pegmatite
Apatite-zircon-bearing pegmatite
Garnet-columbite-bearing pegmatite
Garnet-REE-bearing pegmatite
K-rich plutonic rocks
K-rich granitoid (Ilboudo et al., 2020)
GG-granitoid
Hornblende-biotite granodiorite
Monzogabbro
Na-rich plutonic rocks
Two-mica tonalite
Trondhjemite
K-rich gneisses
Granodioritic gneiss
Microgranular enclave in granodioritic gneiss
Na-rich gneiss
Tonalitic-trondhjemitic gneiss

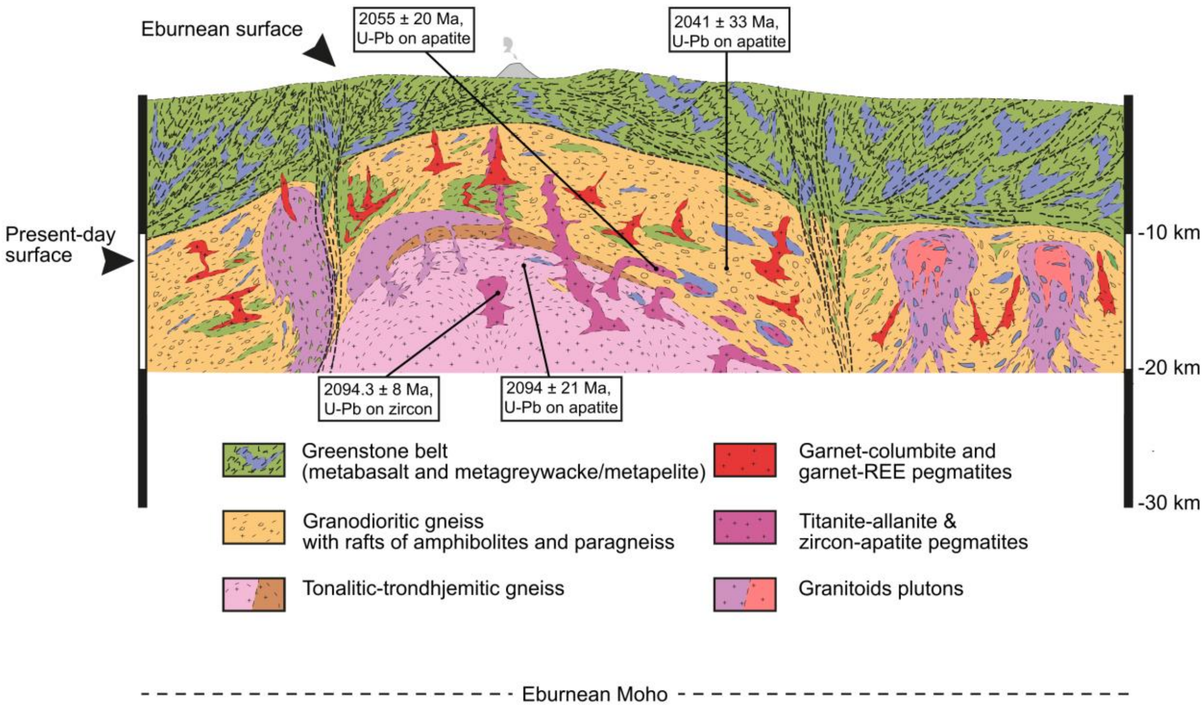
Eburnean surface
2055 ± 20 Ma, U-Pb on apatite
2041 ± 33 Ma, U-Pb on apatite
Present-day surface
-10 km
-20 km
-30 km
2094.3 ± 8 Ma, U-Pb on zircon
2094 ± 21 Ma, U-Pb on apatite
Greenstone belt (metabasalt and metagreywacke/metapelite)
Garnet-columbite and garnet-REE pegmatites
Granodioritic gneiss with rafts of amphibolites and paragneiss
Titanite-allanite & zircon-apatite pegmatites
Tonalitic-trondhjemitic gneiss
Granitoids plutons
Eburnean Moho

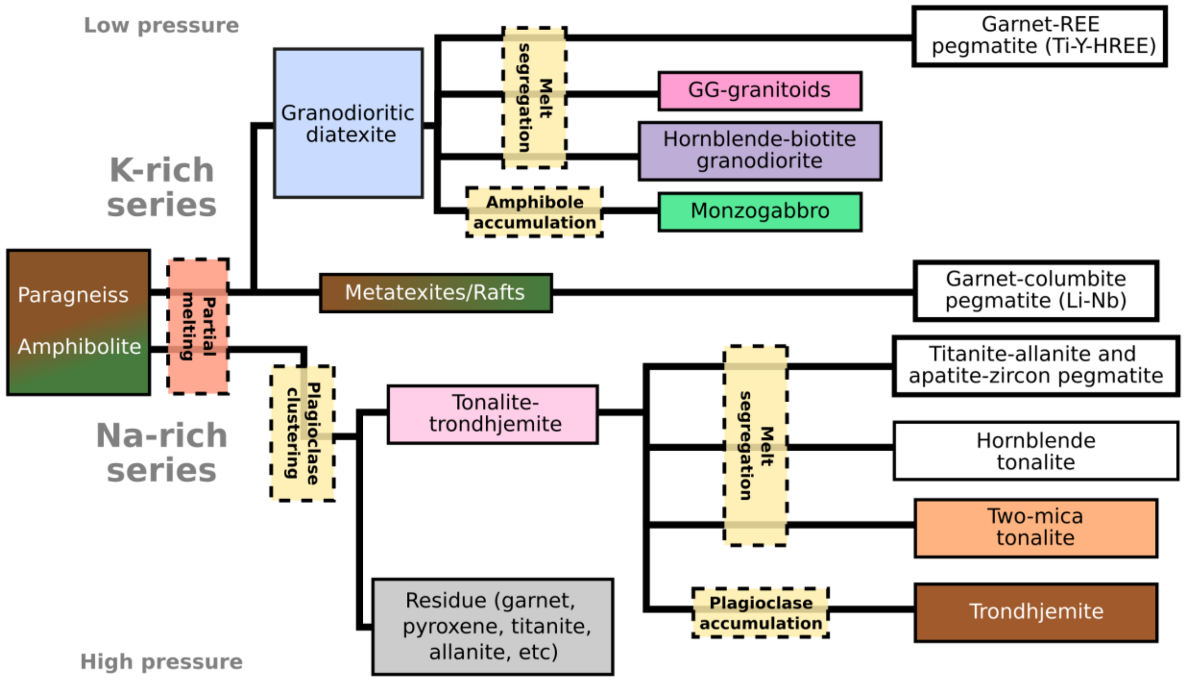
Low pressure
K-rich series
Na-rich series
High pressure
Paragneiss
Amphibolite
Partial melting
Granodioritic diatexite
Melt segregation
Amphibole accumulation
Garnet-REE pegmatite (Ti-Y-HREE)
GG-granitoids
Hornblende-biotite granodiorite
Monzogabbro
Metatexites/Rafts
Garnet-columbite pegmatite (Li-Nb)
Plagioclase clustering
Tonalite-trondhjemite
Residue (garnet, pyroxene, titanite, allanite, etc)
Melt segregation
Plagioclase accumulation
Titanite-allanite and apatite-zircon pegmatite
Hornblende tonalite
Two-mica tonalite
Trondhjemite

1886

Tables

Table 1. Isotopic data for in-situ LA-ICP-MS zircon dating of the titanite-allanite-type pegmatite

N°	U (ppm)	Th (ppm)	Pb (ppm)	Position	Texture	Th/U	$^{207}Pb/^{235}U$	2σ	$^{206}Pb/^{238}U$	2σ	Rho	$^{207}Pb/^{206}Pb$	2σ	Age $^{207}Pb/^{235}U$	2σ	Age $^{206}Pb/^{238}U$	2σ	Age $^{207}Pb/^{206}Pb$	2σ
1	313	35	243	Core	Oscillatory	0.11	3.598	0.078	0.1954	0.003	0.7554	0.1328	0.002	1546.5	18	1150	17	2128	21
2	722	1	382	Metamict rim	Oscillatory-patchy	0.00	4.035	0.097	0.2152	0.004	0.7152	0.13381	0.002	1633	20	1255	20	2144	20
3	27	5	28	Core	Oscillatory	0.17	6.4	0.21	0.353	0.011	0.9497	0.1342	0.003	2001	29	1915	49	2110	42
4	**15**	**0**	**1**	**Medium zone**	**Oscillatory**	**0.00**	**6.88**	**0.18**	**0.3834**	**0.008**	**0.7676**	**0.1282**	**0.002**	**2078**	**24**	**2083**	**36**	**2047**	**33**
5	**16**	**0**	**2**	**Medium zone**	**Oscillatory**	**0.00**	**6.94**	**0.22**	**0.3827**	**0.01**	**0.7996**	**0.129**	**0.003**	**2091**	**27**	**2080**	**45**	**2064**	**38**
6	**168**	**0**	**26**	**Core**	**Oscillatory**	**0.00**	**7**	**0.18**	**0.3891**	**0.009**	**0.8695**	**0.1298**	**0.002**	**2108**	**27**	**2112**	**42**	**2091**	**21**
7	1528	0	288	Metamict rim	Oscillatory-patchy	0.00	1.801	0.041	0.1166	0.002	0.8665	0.1155	0.001	1046	18	710	13	1881	23
8	**109**	**32**	**196**	**Core**	**Oscillatory**	**0.29**	**6.89**	**0.15**	**0.3817**	**0.007**	**0.8063**	**0.1305**	**0.002**	**2090**	**20**	**2081**	**31**	**2094**	**23**
9	680	6	160	Metamict rim	Patchy	0.01	3.02	0.062	0.1742	0.003	0.7829	0.1217	0.001	1411.9	16	1034	15	1977	21
10	83	25	168	Core	Oscillatory	0.30	6.29	0.14	0.3422	0.006	0.8009	0.1355	0.002	2009	19	1894	29	2166	24
11	52	10	59	Medium zone	Oscillatory	0.19	6.36	0.14	0.3569	0.006	0.8019	0.1315	0.002	2020	20	1961	30	2103	26
12	143	43	261	Core	Oscillatory	0.30	5.628	0.13	0.3092	0.006	0.8821	0.1323	0.002	1918	21	1733	31	2117	27
13	**107**	**45**	**283**	**Core**	**Oscillatory**	**0.42**	**6.79**	**0.15**	**0.3771**	**0.006**	**0.7202**	**0.1328**	**0.002**	**2080**	**19**	**2059**	**28**	**2131**	**22**
14	1567	1	410	Metamict rim	Oscillatory	0.00	1.323	0.033	0.0827	0.001	0.6785	0.11304	0.001	853.7	16	512.1	8.6	1843	24
15	1815	6	455	Metamict rim	Oscillatory	0.00	1.135	0.035	0.0723	0.002	0.7176	0.1168	0.001	768.9	15	450	9.5	1903	21
16	843	1	262	Metamict rim	Oscillatory	0.00	3.073	0.066	0.172	0.003	0.7580	0.1279	0.002	1423	17	1022	16	2063	23
17	127	53	287	Core	Oscillatory	0.42	6.329	0.14	0.3491	0.006	0.7640	0.1316	0.002	2017.6	19	1927	28	2114	22

18	**81**	**40**	**212**	**Core**	**Oscillatory**	**0.49**	**6.928**	**0.15**	**0.3866**	**0.006**	**0.7168**	**0.1308**	**0.002**	**2098.4**	**19**	**2106**	**28**	**2100**	**22**
19	1621	2	332	Metamict rim	Oscillatory-patchy	0.00	1.578	0.039	0.1034	0.002	0.7044	0.11127	0.001	958.2	15	633.7	10	1812	22
20	997	3	191	Metamict rim	Oscillatory-patchy	0.00	2.662	0.055	0.1614	0.002	0.7197	0.12063	0.001	1316.3	15	964.3	13	1960	20
21	129	26	168	Core	Oscillatory	0.20	3.862	0.084	0.2116	0.004	0.7605	0.1338	0.002	1602.8	18	1235	18	2142	23
22	1533	4	354	Core	Oscillatory-patchy	0.00	1.463	0.041	0.0896	0.003	0.9300	0.1259	0.002	916	18	555	16	2030	26
23	**79**	**38**	**206**	**Core**	**Oscillatory**	**0.48**	**6.78**	**0.15**	**0.3773**	**0.006**	**0.7308**	**0.1319**	**0.002**	**2082**	**19**	**2060**	**29**	**2115**	**23**
24	56	2	31	Medium zone	Oscillatory	0.04	6.01	0.14	0.3261	0.006	0.7504	0.1346	0.002	1972	20	1816	27	2144	25
25	2615	4	510	Metamict rim	Oscillatory-patchy	0.00	0.843	0.054	0.0569	0.003	0.7961	0.10376	0.001	618.9	23	356.5	17	1688	23
26	2029	0	374	Metamict rim	Oscillatory-patchy	0.00	2.883	0.074	0.1675	0.003	0.7908	0.11968	0.001	1375.9	25	998	19	1948	23
27	1096	1	351	Metamict rim	Oscillatory-patchy	0.00	2.271	0.056	0.1325	0.003	0.8264	0.1257	0.002	1200	21	801	16	2036	24
28	544	2	71	Metamict core	Oscillatory-patchy	0.00	6.166	0.14	0.3444	0.006	0.7801	0.1304	0.002	1997	20	1905	30	2097	21
29	112	0	39	Core	Homogeneous	0.00	6.353	0.13	0.3435	0.005	0.7540	0.132	0.002	2023	19	1903	25	2117	22
30	304	0	32	Core	Patchy	0.00	5.23	0.11	0.2906	0.005	0.8344	0.1322	0.002	1853	19	1642	26	2122	20
31	**219**	**0**	**9**	**Metamict core**	**Oscillatory-patchy**	**0.00**	**6.711**	**0.15**	**0.38**	**0.008**	**0.8830**	**0.12996**	**0.002**	**2069**	**23**	**2072**	**36**	**2091**	**20**
32	728	0	202	Transition core-rim	Oscillatory-patchy	0.00	2.212	0.049	0.1326	0.002	0.7830	0.12273	0.002	1181.9	16	802.3	13	1990	22
33	3558	9	1257	Metamict rim	Oscillatory-patchy	0.00	0.9263	0.02	0.0495	0.0008	0.7386	0.13913	0.002	665.3	10	311.6	4.8	2212	21
34	4931	3	1344	Metamict rim	Oscillatory-patchy	0.00	0.5711	0.012	0.0298	0.0005	0.8134	0.14287	0.002	458.1	7.9	189.5	3.2	2258	21

35	3527	3	635	Metamict rim	Oscillatory-patchy	0.00	0.6233	0.013	0.0436	0.0007	0.7473	0.10623	0.001	491.8	8	275.2	4.2	1727	25
36	699	1	26	Metamict core	Oscillatory-patchy	0.00	6.391	0.13	0.3611	0.005	0.7352	0.1296	0.001	2029.2	18	1985	26	2088	19
37	855	0	223	Metamict rim	Oscillatory-patchy	0.00	2.693	0.068	0.1504	0.003	0.8689	0.1323	0.002	1324	18	902	18	2123	21
38	509	0	51	Transition core-rim	Patchy	0.00	6.074	0.13	0.3476	0.006	0.7796	0.13033	0.002	1983.5	20	1920	28	2098	20
39	**73**	**29**	**164**	**Core**	**Oscillatory**	**0.40**	**6.889**	**0.16**	**0.3837**	**0.007**	**0.7518**	**0.1318**	**0.002**	**2093**	**20**	**2090**	**31**	**2115**	**23**
40	25	0	4	Core	Homogeneous	0.01	6.16	0.2	0.3456	0.01	0.8912	0.1333	0.002	1970	31	1896	51	2110	32
41	185	2	43	Core	Oscillatory	0.01	6.122	0.15	0.3455	0.007	0.7678	0.1337	0.002	1988	21	1915	31	2142	25
42	2002	9	405	Metamict core	Oscillatory-patchy	0.00	1.223	0.13	0.0813	0.007	0.8563	0.1075	0.002	810.6	36	503.9	40	1749	24
43	**5281**	**1**	**5027**	**Core**	**Oscillatory-patchy**	**0.00**	**6.978**	**0.14**	**0.3902**	**0.006**	**0.7536**	**0.13026**	**0.001**	**2106.3**	**18**	**2121**	**27**	**2099.5**	**19**

Table 2. Isotopic data for in-situ LA-ICP-MS apatite dating of granodioritic gneiss, tonalitic-trondhjemitic gneiss and apatite-zircon pegmatite

N°	**U (ppm)**	**Th (ppm)**	**Pb (ppm**	**Position**	**Texture**	**Equivalent diameter**	**238U/206Pb**	**2σ**	**207Pb/206Pb**	**2σ**
BMN20B – Granodioritic gneiss										
1	37.0	3.1	4.3	Core	Oscillatory	200	2.51	1.4	0.1728	1.2
2	79.7	4.8	4.5	Core	Oscillatory	200	2.65	2.0	0.1502	0.9
3	44.8	1.4	3.4	Core	Oscillatory	200	2.63	2.4	0.1631	1.3
4	28.4	0.8	3.8	Core	Homogeneous	200	2.50	2.1	0.1893	1.2
5	33.9	0.6	3.3	Core	Homogeneous	200	2.52	2.1	0.1728	1.3
6	16.1	0.1	3.2	Core	Homogeneous	100	2.40	2.2	0.2199	1.5

7	19.7	0.6	3.6	Transition core-rim	Oscillatory	150	2.39	2.1	0.2102	1.3
8	28.0	3.1	4.4	Core	Homogeneous	200	2.44	2.0	0.1900	0.7
9	49.8	9.5	5.7	Core	Oscillatory	250	2.51	2.0	0.1643	1.1
10	43.8	7.6	5.1	Core	Oscillatory	100	2.50	1.7	0.1631	1.5
11	11.5	0.4	1.3	Core	Homogeneous	100	2.53	1.5	0.1845	2.2
12	6.6	0.2	3.3	Core	Homogeneous	150	2.03	1.6	0.3185	1.3
13	19.3	0.4	3.7	Core	Homogeneous	200	2.44	1.5	0.2142	1.2
14	29.2	4.5	4.5	Core	Homogeneous	200	2.46	1.7	0.1850	1.4
BMN11 – Tonalitic-trondhjemitic gneiss										
1	2.2	1.2	4.3	Core	Homogeneous	200	1.30	5.1	0.5500	4.9
2	21.9	5.4	3.0	Zone 1	Homogeneous	800	2.53	2.1	0.1664	1.3
3	11.5	2.9	2.2	Core	Homogeneous	250	2.36	2.0	0.1854	1.1
4	19.8	3.4	2.2	Rim	Homogeneous	200	2.48	2.0	0.1606	0.9
5	20.5	2.5	1.9	Core	Oscillatory	200	2.47	2.0	0.1587	1.1
6	32.9	4.2	2.6	Zone 1	Homogeneous	200	2.53	2.0	0.1539	0.9
7	6.2	0.6	1.7	Core	Homogeneous	200	2.24	2.1	0.2378	1.4
8	25.6	4.3	2.3	Zone 1	Homogeneous	400	2.55	2.0	0.1522	1.1
9	8.5	1.2	1.6	Core	Homogeneous	400	2.41	2.1	0.1881	1.8
10	34.0	5.2	3.1	Zone 1	Homogeneous	100	2.54	2.0	0.1546	0.9
11	6.3	0.7	1.9	Zone 1	Homogeneous	100	2.27	2.2	0.2509	2.0
12	28.8	3.3	2.6	Transition core-zone 1	Oscillatory	100	2.61	2.0	0.1588	1.2
13	9.2	0.5	1.5	Zone 1	Homogeneous	100	2.46	8.1	0.1954	2.1
14	21.7	6.3	3.2	Core	Homogeneous	800	2.46	9.1	0.1668	2.8
15	8.5	1.4	2.3	Core	Complexe	800	2.33	8.2	0.2323	2.6

16	31.8	6.7	5.2	Transition core-zone 1	Complexe	800	2.52	8.1	0.1624	1.3
17	7.2	1.2	2.2	Zone 1	Complexe	200	2.24	8.5	0.2418	2.4
18	13.4	1.6	2.5	Transition core-zone 1	Complexe	200	2.39	8.1	0.2078	2.7
19	34.6	6.0	3.6	Zone 1	Homogeneous	200	2.55	8.1	0.1584	1.1
20	36.1	4.8	2.9	Zone 1	Homogeneous	300	2.55	8.2	0.1504	1.1
21	5.1	0.4	2.7	Transition core-zone 1	Complexe	200	2.05	8.2	0.3257	2.1
22	34.0	4.8	3.1	Core	Complexe	200	2.56	8.2	0.1575	1.0
23	10.1	0.8	2.0	Zone 1	Homogeneous	200	2.34	8.2	0.2099	2.3
24	31.5	3.8	2.9	Transition zones 1-2	Homogeneous	200	2.55	8.1	0.1612	1.2
25	33.6	5.0	3.2	Zone 2	Homogeneous	200	2.56	8.2	0.1585	1.2
26	16.3	2.5	2.5	Transition core-zone 1	Oscillatory	200	2.46	8.1	0.1858	1.3
BMN20 – Titanite-allanite type pegmatite										
1	54.3	5.1	3.7	Core	Homogeneous	600	2.60	1.4	0.1516	0.9
2	85.3	13.7	5.8	Core	Homogeneous	600	2.66	1.6	0.1431	1.0
3	55.7	3.6	3.2	Core	Mottled	500	2.61	2.1	0.1499	1.3
4	14.8	3.1	3.3	Core	Homogeneous	600	2.45	1.8	0.2118	1.3
5	24.1	3.6	3.6	Core	Homogeneous	600	2.50	1.6	0.1849	1.3
6	33.4	2.1	3.1	Core	Homogeneous	600	2.62	1.5	0.1659	1.0
7	55.8	3.2	3.1	Core	Homogeneous	600	2.70	2.5	0.1477	0.9
8	39.0	2.7	3.1	Core	Homogeneous	600	2.60	1.5	0.1603	1.2
9	34.3	2.4	3.0	Core	Homogeneous	600	2.53	1.8	0.1641	1.3
10	41.2	4.0	5.7	Core	Homogeneous	500	2.45	1.5	0.1807	1.0
11	58.1	4.6	5.4	Core	Homogeneous	500	2.56	1.6	0.1635	0.9

12	18.8	7.9	7.5	Core	Homogeneous	1500	2.22	8.2	0.2604	1.1
13	19.1	9.0	7.3	Core	Homogeneous	1500	2.27	8.2	0.2552	1.2
14	17.6	7.6	7.1	Core	Homogeneous	1500	2.20	8.4	0.2557	1.3
15	15.7	6.7	6.3	Core	Homogeneous	1500	2.02	9.1	0.2472	1.6
16	24.7	6.1	7.6	Transition core-zone 1	Oscillatory	1500	2.25	8.3	0.2276	1.4
17	82.0	7.4	7.8	Rim	Oscillatory	1500	2.46	8.1	0.1592	0.9
18	75.4	6.1	6.7	Rim	Oscillatory	1500	2.55	8.2	0.1599	1.0
19	63.2	5.2	6.5	Rim	Oscillatory	1500	2.46	8.1	0.1639	0.9
20	67.4	5.5	6.9	Rim	Oscillatory	1500	2.47	8.1	0.1639	1.2
21	70.0	5.6	5.7	Rim	Oscillatory	1500	2.59	8.0	0.1583	0.9
22	106.3	10.6	5.3	Core	Homogeneous	1000	2.65	8.2	0.1463	2.7
23	80.8	8.9	4.5	Core	Mottled	1000	2.67	9.3	0.1426	1.9
24	9.9	1.3	2.7	Core	Homogeneous	1000	2.22	8.2	0.2303	2.2
25	5.8	0.1	2.9	Core	Homogeneous	600	2.06	8.3	0.3131	1.6
26	3.0	0.1	2.3	Core	Homogeneous	1000	1.79	1.8	0.3882	1.9
27	5.3	0.1	3.3	Core	Mottled	1000	1.92	2.3	0.351	3.1
28	5.0	0.1	2.9	Core	Mottled	1000	1.92	1.7	0.3287	1.9
29	4.1	0.1	2.9	Core	Mottled	1000	1.86	1.8	0.3734	1.8
30	15.7	1.7	4.5	Core	Homogeneous	1000	2.23	1.5	0.2371	1.2
31	31.7	3.1	5.6	Core	Homogeneous	1000	2.36	1.5	0.1973	1.1
32	41.4	3.7	5.8	Core	Homogeneous	1000	2.45	1.5	0.1834	1.0
33	16.7	1.5	3.1	Core	Homogeneous	1000	2.34	1.5	0.2015	1.5
34	48.0	3.9	3.2	Core	Homogeneous	500	2.42	2.3	0.1532	2.1
35	79.0	9.8	7.2	Core	Homogeneous	600	2.59	1.3	0.1587	0.9
36	12.6	1.8	3.6	Rim	Homogeneous	350	2.23	1.9	0.2335	1.9

37	13.3	1.9	4.0	Core	Homogeneous	350	2.28	1.6	0.2441	2.1
38	18.0	2.4	3.6	Rim	Homogeneous	350	2.37	1.4	0.2026	1.5
39	6.5	0.5	4.4	Core	Homogeneous	600	1.78	2.7	0.3354	3.3
40	11.1	1.0	2.9	Core	Mottled	600	2.28	1.7	0.2305	2.0
41	89.9	8.1	7.0	Core	Homogeneous	600	2.55	1.3	0.1558	0.9
42	56.7	4.9	6.3	Core	Homogeneous	600	2.50	1.3	0.1708	0.9
43	58.9	5.4	6.4	Core	Homogeneous	600	2.48	1.3	0.1682	1.1
44	70.3	5.9	6.6	Rim	Oscillatory	1500	2.50	1.4	0.1637	1.1

Table 3. EMPA composition of amphibole in granodioritic gneiss. hornblende-biotite granodiorite with mica-rich enclaves. and hornblende tonalite veins; Calculated pressures of crystallization are given in the last rows with a reference to the corresponding calculation method.

Lithology	Granodioritic gneiss						Hornblende-biotite granodiorite with mica-rich enclaves								Hornblende tonalite			
Sample	BMN24						BMS46								BMN164H			
SiO_2	41.90	41.99	40.90	42.54	41.95	41.63	41.79	41.38	41.88	41.20	41.51	41.03	41.49	42.09	41.70	41.98	42.15	41.48
TiO_2	0.66	0.55	0.68	0.72	0.72	0.68	0.48	0.48	0.61	0.68	0.50	0.65	0.51	0.54	1.28	1.25	1.31	1.28
Al_2O_3	10.70	10.72	10.93	10.75	10.94	11.16	10.96	10.77	10.71	10.77	11.54	11.18	10.93	11.02	10.51	10.37	10.43	10.92
FeO	19.79	19.90	20.26	19.16	19.73	19.54	19.35	19.13	19.54	19.14	19.54	19.64	19.33	19.32	18.57	18.56	18.82	19.10
MnO	0.54	0.44	0.45	0.51	0.54	0.48	0.56	0.53	0.50	0.49	0.44	0.52	0.46	0.52	0.52	0.45	0.47	0.44
MgO	8.55	9.02	8.47	8.73	8.89	8.46	9.29	9.09	9.01	8.74	8.96	8.93	8.92	8.82	9.32	9.19	9.23	8.79
CaO	11.36	11.46	11.68	11.63	11.49	11.27	11.60	11.52	11.56	11.85	11.42	11.38	11.54	11.37	11.33	11.46	11.31	11.14
Na_2O	1.38	1.41	1.26	1.09	1.47	1.46	1.81	1.38	1.52	1.36	1.52	1.73	1.49	1.47	1.59	1.56	1.53	1.53
K_2O	1.25	1.38	1.36	1.16	1.34	1.39	1.37	1.38	1.29	1.32	1.38	1.48	1.38	1.37	1.20	1.17	1.20	1.28
F	bdl	bdl	bdl	bdl	bdl	bdl	bdl	bdl	bdl	bdl	bdl	bdl	bdl	bdl	bdl	bdl	bdl	0.55
Total	96.4	96.89	96.37	96.33	97.5	96.43	97.22	95.99	96.77	95.85	97.15	96.97	96.43	96.93	96.25	96.06	96.56	96.51
Si	6.427	6.386	6.311	6.49	6.373	6.393	6.351	6.38	6.395	6.388	6.308	6.285	6.375	6.421	6.385	6.441	6.423	6.363
Al IV	1.573	1.614	1.689	1.51	1.627	1.607	1.649	1.62	1.605	1.612	1.692	1.715	1.625	1.579	1.615	1.559	1.577	1.637

Sum T	8	8	8	8	8	8	8	8	8	8	8	8	8	8	8	8	8	8
Al VI	0.362	0.308	0.299	0.423	0.332	0.414	0.313	0.336	0.323	0.355	0.374	0.304	0.354	0.402	0.282	0.316	0.296	0.339
Ti	0.076	0.062	0.079	0.083	0.082	0.078	0.055	0.056	0.07	0.079	0.057	0.075	0.059	0.062	0.148	0.144	0.15	0.148
Fe3	0.67	0.759	0.728	0.571	0.693	0.62	0.646	0.65	0.652	0.492	0.769	0.718	0.637	0.633	0.607	0.489	0.595	0.628
Mg	1.954	2.046	1.948	1.984	2.012	1.936	2.105	2.088	2.05	2.02	2.029	2.039	2.043	2.006	2.127	2.102	2.097	2.01
Fe2	1.868	1.772	1.887	1.874	1.813	1.89	1.812	1.817	1.844	1.989	1.714	1.799	1.847	1.832	1.771	1.892	1.803	1.822
Mn	0.07	0.053	0.059	0.065	0.067	0.062	0.069	0.053	0.061	0.064	0.056	0.066	0.06	0.065	0.065	0.056	0.058	0.054
Sum C	5	5	5	5	5	5	5	5	5	5	5	5	5	5	5	5	5	5
Mn	0	0.003	0	0.001	0.003	0	0.003	0.016	0.003	0	0.001	0.002	0	0.001	0.002	0.003	0.003	0.003
Fe2	0	0	0	0	0	0	0	0	0	0	0	0	0	0	0	0	0	0
Ca	1.867	1.867	1.93	1.901	1.87	1.855	1.889	1.903	1.891	1.968	1.858	1.867	1.9	1.858	1.859	1.884	1.847	1.832
Na	0.133	0.13	0.07	0.098	0.127	0.145	0.109	0.081	0.106	0.032	0.141	0.13	0.1	0.141	0.139	0.113	0.151	0.165
Sum B	2	2	2	2	2	2	2	2	2	2	2	2	2	2	2	2	2	2
Ca	0	0	0	0	0	0	0	0	0	0	0	0	0	0	0	0	0	0
Na	0.278	0.285	0.306	0.223	0.306	0.289	0.423	0.333	0.344	0.378	0.308	0.384	0.345	0.294	0.334	0.35	0.302	0.29
K	0.245	0.267	0.268	0.225	0.259	0.273	0.266	0.271	0.251	0.261	0.268	0.289	0.271	0.267	0.234	0.229	0.234	0.25
Sum A	0.523	0.552	0.574	0.448	0.565	0.561	0.689	0.604	0.596	0.639	0.576	0.673	0.615	0.561	0.569	0.579	0.536	0.54
F																		0.27
Hollister et al.. (1987) +-1 kbar	6.3	6.3	6.6	6.3	6.5	6.8	6.5	6.4	6.3	6.5	7.1	6.8	6.6	6.6	6.1	5.9	5.9	6.4
Johnson and Rutherford (1989) +-0.5 kbar	4.8	4.8	5.1	4.8	5	5.2	5	4.9	4.8	5	5.4	5.2	5	5	4.7	4.6	4.6	4.9
Schmidt (1992) +-0.6 kbar	6.3	6.3	6.6	6.3	6.5	6.7	6.5	6.4	6.3	6.5	7	6.8	6.5	6.5	6.1	6	6	6.4
Thomas and Ernst (1990) +-1 kbar	4.3	4.2	4.6	4.2	4.4	4.7	4.4	4.4	4.2	4.4	5	4.7	4.5	4.5	4	3.9	3.9	4.3
Mutch et al.. (2016) +- 0.6 kbar	5	4.9	5.2	5	5.1	5.4	5.1	5.1	5	5.1	5.6	5.4	5.2	5.2	4.8	4.7	4.7	5.1

Table 4. Major and trace elements composition of amphibolites, micaschist, paragneiss, gneisses, plutonic rocks and pegmatites.

	Amphibolite	**Amphibolite**	**Micaschist**	**Paragneiss**	**Granodioritic gneiss**			**Microgranular enclave in granodioritic gneiss**	**Monzogabbro**	**Hornblende-biotite granodiorite**		**GG-granitoid**	**GG-granitoid**
Sample	BMN109	BMN150	1684-sd	BMS114B	BMN7	BMN24	BB15	BMN94	BMN47bis	BMS134C	BMS23	BB7	BMN1
SiO_2	54.05	52.3	61.68	61.66	66.72	69.71	62.65	69.2	51.86	65.67	68.13	71.89	67.16
Al_2O_3	11.89	16.87	14.39	17.95	15.14	15.14	14.68	15.81	17.38	15.73	15.11	14.59	14.89
Fe_2O_3	11.11	9.15	8.11	7.85	4.55	3.08	5.39	3.08	10.13	4.47	3.5	2.12	4.22
CaO	10.15	9.63	6.92	1.24	3.86	2.98	4.44	3.1	5.45	3.72	2.97	2.31	3.21
MgO	7.31	5.6	2.41	2.84	2.01	1.21	2.97	0.92	4.93	1.75	1.35	0.76	1.41
Na_2O	2.18	3.83	2.99	2.08	3.99	4.2	3.85	4.51	4.3	4.27	4.28	4.23	3.66
K_2O	0.49	0.38	0.25	2.94	3.17	2.98	3.33	2.74	2.28	2.81	2.79	3.17	3.56
TiO_2	1.04	0.87	0.83	0.73	0.43	0.38	0.54	0.32	0.97	0.49	0.37	0.21	0.6
MnO	0.11	0.15	0.19	0.09	0.07	0.05	0.08	0.04	0.13	0.07	0.06	0.04	0.06
P_2O_5	0.23	0.2	0.42	bdl	0.17	0.14	0.24	0.17	0.45	0.22	0.16	0.08	0.24
LOI	0.47	1.37	0.87	1.87	0.76	0.65	1.4	0.57	1.48	0.68	0.85	0.53	0.82
Total	99.19	100.33	99.06	99.25	100.86	100.5	99.57	100.45	99.36	99.87	99.56	99.93	99.82
100 *Mg#	56.58	54.78	37.09	41.75	46.71	43.67	52.19	37.28	49.1	43.76	43.31	41.49	39.84
Be	0.93	1.21	1	1.19	1.42	1.29	1.69	1.45	1.60	1.53	1.58	1.46	1.43
Sc	34.44	25.01	12.17	21.47	9.56	5.52	13.52	2.07	27.68	10.73	8.62	3.86	10.18
V	207	161	54	139	80	46	99	46	182.89	73	59	28	58
Cr	1129	87	26	217	227	134	156	51	86.73	32	106	183	177
Co	43.91	27.09	22.4	25.53	10.92	6.48	16.63	5.11	28	10.26	7.37	3.89	7.62
Ni	313.65	24.11	9.45	71.19	15.8	9.26	25.03	13.44	29	8.35	9.41	7.84	9.12
Cu	56.6	11.69	bdl	2.65	14.21	6.96	40.53	15.27	8.02	53.13	20.1	2.56	2.37
Zn	86	90	128	110	58	52	68	48	128	74	58	39	64
Ga	na	18.99	18.01	23.60	18.06	17.66	18.84	17.32	22.83	20.04	18.55	16.88	18.67
Ge	na	1.24	1.41	1.98	1.19	1.2	1.31	0.95	1.62	1.38	1.22	1.03	1.23
Cs	0.16	0.12	0.21	5.4	2.54	2.49	1.71	2.18	3.82	1.9	2.06	1.76	1.76
Rb	2.92	2.40	2.99	114.17	98.15	73.31	90.57	55.91	100.11	84.44	87.05	91.12	108.32
Sr	412	276	510	199	598	606	610	689	788	769	655	473	499
Ba	213	132	79	608	711	854	791	1018	618.94	753	606	653	1071
Y	17.30	26.97	31.58	21.40	10.54	10.36	16.70	5.68	25.15	16.22	15.16	8.39	19.31

Zr	119	151	182	139	117	107	191	111	162	164	111	103	233
Hf	2.9	3.69	4.33	3.87	3.3	3.11	5.02	3.08	4.06	4.47	3.21	2.99	5.84
Nb	9.74	8.38	7.43	6.42	5.05	5.1	5.77	3.36	6.00	5.47	4.65	4.34	9.99
Ta	0.56	0.63	0.68	0.57	0.65	0.66	0.45	0.33	0.39	0.51	0.52	0.32	1.27
Mo	9.08	1.6	1.59	3.95	10.88	7.01	5.41	3.41	0.57	1.22	5.11	9.9	9.41
Cd	na	0.17	0.16	0.05	0.07	0.05	0.07	0.04	0.1	0.07	0.06	0.04	0.07
In	na	0.05	0.05	0.06	bdl	bdl	0.03	bdl	0.07	0.04	bdl	bdl	bdl
Sn	2.99	1.72	1.83	1.44	1.07	1	1.17	0.84	1.76	1.08	1.18	0.95	1.54
Sb	na	0.13	bdl	bdl	0.09	bdl	bdl	bdl	bdl	bdl	bdl	bdl	bdl
W	na	1.22	0.98	4.08	8.27	5.35	3.92	1.19	bdl	bdl	3.85	7.55	7.13
Pb	3.5	4.6	6.4	7.5	11	10.3	11.4	11	5.2	10.2	10.4	10.8	11.8
Bi	na	0.29	0.13	0.07	0.11	0.15	0.08	0.12	0.07	0.08	0.14	bdl	0.06
Th	1.86	2.82	2.06	3.62	8.78	3.77	5.49	3	3.12	3.19	4.59	3.5	6.75
U	0.47	0.74	0.61	1.31	1.76	0.79	0.65	0.95	0.52	0.93	1.24	0.63	1.94
K/Rb	1393	1312	696	213	268	338	306	407	1.62	276	266	289	273
Ca/Cs	459131	561164	237708	1641	10835	8531	18566	10143	0.1	14031	10313	9415	13052
Nb/Ta	17.3	13.2	10.9	11.35	7.79	7.72	12.8	10.09	12.94	10.83	8.89	13.53	7.84
Zr/Hf	40.97	40.91	41.95	35.77	35.42	34.38	38.06	35.98	0.79	36.79	34.66	34.43	39.95
La	20.6	14.5	20.6	20.8	37.1	21.6	34.2	20.5	26.1	27.3	25.4	18.5	41.2
Ce	44.2	32.8	45.3	43.3	77.1	49.7	60	39.9	67.6	49.7	45.8	47.5	89.7
Pr	5.6	4.74	6.1	5.58	8.13	5.81	8.45	4.71	7.36	7.93	6.15	4.13	10.35
Nd	23	19.8	24.2	22.4	28.4	22.5	33.4	17.4	30.3	32.4	24.2	14.3	38.9
Sm	4.38	4.76	5.36	4.54	4.42	4.11	6.38	2.68	6.68	6.14	4.58	2.5	6.97
Eu	1.22	1.35	1.54	1.11	1.1	1.05	1.47	0.89	1.81	1.51	1.1	0.68	1.56
Gd	3.87	4.42	5.08	3.92	2.99	2.84	4.73	1.71	5.54	4.39	3.48	1.8	4.96
Tb	0.55	0.7	0.82	0.6	0.37	0.36	0.59	0.19	0.85	0.56	0.45	0.24	0.66
Dy	3.27	4.54	5.23	3.82	1.99	1.93	3.16	1.03	4.92	3.12	2.43	1.35	3.64
Ho	0.65	0.97	1.13	0.82	0.37	0.35	0.59	0.2	0.94	0.59	0.48	0.26	0.7
Er	1.85	2.7	3.09	2.23	1.02	0.95	1.5	0.53	2.33	1.57	1.24	0.7	1.82
Tm	0.24	0.41	0.47	0.34	0.15	0.14	0.22	0.08	0.33	0.23	0.17	0.11	0.27
Yb	1.72	2.73	3.07	2.15	1.02	0.93	1.35	0.55	2.02	1.47	1.07	0.69	1.74
Lu	0.24	0.42	0.47	0.33	0.16	0.14	0.21	0.09	0.28	0.22	0.16	0.11	0.26
SumREE	111.3	94.8	122.5	111.9	164.3	112.4	156.2	90.5	157.1	137.1	116.7	92.9	202.8
LaN/YbN*	8.1	3.6	4.6	6.6	24.7	15.8	17.2	25.5	8.8	12.6	16.2	18.3	16.1
La/Yb	12	5	7	10	36	23	25	38	13	19	24	27	24
Sr/Y	24	10	16	9	57	59	37	121	1.1	47	43	56	26
Ce/Sr	0.11	0.12	0.09	0.22	0.13	0.08	0.10	0.06	0.09	0.06	0.07	0.10	0.18

	Na-rich series					Pegmatites			
	Tonalitic-trondhjemitic gneiss			**Trondhjemite**	**Two-mica granite**	**Titanite-allanite-bearing pegmatite**	**Apatite-zircon-bearing pegmatite**	**Garnet-columbite-bearing pegmatite**	**Garnet-REE-bearing pegmatite**
Sample	BMS34C	BMN42	BMN11	BMN33	BMS9	BMN28	BMN82B	BMN86	BB15P
SiO_2	69.56	68.39	71.05	59.23	72.36	71.81	59.57	73.46	76.46
Al_2O_3	15.54	15.27	16.02	20.63	15.41	14.42	20.37	15.05	14.02
Fe_2O_3	2.52	3.6	1.53	3.87	1.33	4.03	2.725	0.21	0.59
CaO	3	3.85	3.09	4.59	2.21	2.73	5.124	0.47	1.58
MgO	0.89	1.56	0.49	1.72	0.33	0.00	1.01	0.00	0.00
Na_2O	5.67	4.96	5.85	7.12	5.46	5.17	6.32	4.69	6.35
K_2O	1.13	1.17	0.81	1.39	1.61	0.63	2.35	5.46	0.52
TiO_2	0.3	0.43	0.16	0.34	0.14	0.063	0.248	bdl	0.025
MnO	0.04	0.05	0.02	0.09	0.02	0.020	0.0546	0.020	0.021
P_2O_5	0.09	0.14	bdl	0.17	bdl	bdl	1.06	0.12	bdl
LOI	0.68	0.56	0.89	0.44	0.35	0.48	0.74	0.55	0.28
Total	99.41	99.95	99.89	99.59	99.22	99.35	99.58	100.02	99.84
100 *Mg#	41.09	46.16	38.7	46.82	32.75				
Be	1.05	0.87	0.97	3.54	1.5	1.28	3.27	1.11	2.56
Sc	6.93	7.16	2.44	24.16	2.04	0.78	6.39	0.96	1.53
V	32	56	18	48	11	62	36	1	3
Cr	40	86	76	47	74	83	43	61	96
Co	5.41	9.84	3.44	9.02	1.54	2.61	5.63	0.17	0.27
Ni	7.98	39.53	5.38	30	2.09	3.09	11.97	bdl	bdl
Cu	61.31	24.11	53.32	5.69	3.34	62.02	5.50	bdl	bdl
Zn	61	57	33	54	39	46	46	33	12
Ga	21.88	19.08	19.83	na	18.03	17.91	27.48	25.60	23.61
Ge	0.72	0.84	0.69	na	0.77	0.67	1.45	1.57	1.38
Cs	0.81	1.27	0.48	1.75	1.55	0.28	4.78	3.71	0.96
Rb	35.47	34.79	16.91	35.70	42.48	5.26	82.61	251.39	19.94
Sr	609	429	424	483	770	391	587	63	35
Ba	158	205	177	151	598	120	336	130	19
Y	8.64	7.75	1.97	10.18	3.75	1.14	48.59	1.92	10.35
Zr	107	105	78	92	83	43	56	15	26
Hf	2.88	2.75	2.1	2.51	2.4	1.26	2.08	0.91	1.01

Nb	2.05	2.55	1.13	3.1	2.07	0.48	9.36	2.87	2.54
Ta	0.26	0.26	0.11	0.3	0.18	0.15	2.01	0.50	0.44
Mo	1.79	4.52	4.23	1.39	4.3	4.77	1.58	3.63	5.79
Cd	0.04	0.06	0.04	na	0.03	0.04	0.07	0.03	0.03
In	bdl	bdl	bdl	na	bdl	bdl	bld	bdl	bdl
Sn	0.73	0.77	bdl	1.87	0.47	bdl	1.52	0.53	0.40
Sb	bdl	bdl	bdl	na	bdl	bdl	0.06	bdl	bdl
W	1.31	1.64	3.24	na	3.48	3.63	1.02	2.93	4.43
Pb	5.2	4.2	4.6	7.1	8.1	5.7	21.0	25.5	27.5
Bi	bdl	0.05	0.09	na	bdl	0.29	0.07	0.05	0.08
Th	1.93	1.6	1.39	4.56	1.33	0.82	6.95	2.21	6.74
U	0.69	0.36	0.21	0.7	0.51	0.87	1.56	0.96	5.22
K/Rb	265	279	398	323	314	989	236	180	217
Ca/Cs	26437	21579	46094	18799	10173	68843	7654	899	11810
Nb/Ta	8.02	9.72	10.46	10.49	11.74	3.19	4.67	5.69	5.78
Zr/Hf	37.15	38.17	37.12	36.83	34.63	33.63	26.89	16.48	25.91
La	23.4	16.4	8.6	22.1	9.9	3.06	6.34	1.89	1.17
Ce	24.9	23.2	15.3	47.9	19.6	6.96	20.24	3.79	2.90
Pr	5.65	3.86	1.77	5.25	2.49	0.71	2.93	0.58	0.29
Nd	21.2	15.4	6.7	18.1	9.6	2.77	15.74	2.19	1.19
Sm	3.88	2.89	1.13	2.9	1.7	0.50	6.98	1.03	0.50
Eu	1.15	0.86	0.45	0.7	0.49	0.35	1.40	0.09	0.26
Gd	2.89	2.3	0.79	2.41	1.11	0.37	9.04	0.73	0.80
Tb	0.34	0.3	0.09	0.34	0.14	0.05	1.53	0.11	0.20
Dy	1.6	1.51	0.46	1.93	0.72	0.25	9.01	0.44	1.56
Ho	0.28	0.27	0.07	0.38	0.13	0.04	1.72	0.06	0.38
Er	0.66	0.65	0.17	0.95	0.33	0.12	4.17	0.12	1.20
Tm	0.09	0.09	0.02	0.13	0.05	0.02	0.54	0.02	0.20
Yb	0.56	0.56	0.15	0.96	0.31	0.15	3.09	0.13	1.34
Lu	0.08	0.08	0.02	0.12	0.05	0.02	0.42	0.02	0.21
SumREE	86.7	68.4	35.8	104.1	46.7	15.4	83.2	11.2	12.2
LaN/YbN*	28.7	19.9	38.8	15.7	21.4	192.2	1.4	134.9	9.2
La/Yb	42	29	57	23	31	21	2	14	1
Sr/Y	70	55	215	47	205	343	12	33	3
Ce/Sr	0.04	0.05	0.04	0.10	0.03	0.02	0.03	0.06	0.08

na. not analyzed. bdl. below the detection limit. * : data normalized to chondrite. (McDonough and Sun. 1995).

Appendix

Appendix 1. Operating conditions for the LA-ICP-MS equipment for U-Pb dating on apatite

Laboratory & Sample Preparation	
Laboratory name	GeOHeLiS Analytical Platform. OSUR. Univ Rennes 1. France
Sample type/mineral	Apatite
Sample preparation	Thin-section
Imaging	Jeol JSM 6360LV. Géoscience Environnement Toulouse. Univ Toulouse 3 Paul Sabatier. France ; TESCAN Vega 3. GeoRessources. Univ de Lorraine. Nancy. France
Laser ablation system	
Make. Model & type	ESI NWR193UC. Excimer
Ablation cell	ESI NWR TwoVol2
Laser wavelength	193 nm
Pulse width	< 5 ns
Fluence	6 J/cm^2
Repetition rate	5Hz
Spot size	40 - 50 µm
Sampling mode / pattern	Single spot
Carrier gas	100% He. Ar make-up gas and N2 (3 ml/mn) combined using in-house smoothing device
Background collection	20 seconds
Ablation duration	60 seconds
Wash-out delay	15 seconds
Cell carrier gas flow (He)	0.75 l/min
ICP-MS Instrument	
Make. Model & type	Agilent 7700x. Q-ICP-MS
Sample introduction	Via conventional tubing
RF power	1350W
Sampler. skimmer cones	Ni
Extraction lenses	X type
Make-up gas flow (Ar)	0.85 l/min
Detection system	Single collector secondary electron multiplier
Data acquisition protocol	Time-resolved analysis
Scanning mode	Peak hopping. one point per peak
Detector mode	Pulse counting. dead time correction applied. and analog mode when signal intensity > ~ 10^6 cps
Masses measured	^{204}(Hg + Pb). ^{206}Pb. ^{207}Pb. ^{208}Pb. ^{232}Th. ^{238}U + ^{43}Ca (Ap)
Integration time per peak	10-30 ms
Sensitivity / Efficiency	23000 cps/ppm Pb (50µm. 10Hz)
Data Processing	
Gas blank	20 seconds on-peak
Calibration strategy	Madagascar apatite standard used as primary reference material. McClure and Durango standards used as secondary reference material (quality control)
Common-Pb correction. composition and uncertainty	No common-Pb correction.
Reference Material info	Madagascar (Cochrane et al. 2014) McClure (Schoene and Bowring 2006) Durango (McDowell et al. 2005)
Data processing package	Iolite (Paton et al.. 2010). VizualAge_UcomPbine (Chew et al.. 2014)

used	More information on the procedure in Pochon et al.. 2016
Quality control / Validation	McClure: Jan2019 - 516 ± 7.5 Ma (n=18. MSWD=8.2) Sept2019 – 529 ± 5.5 Ma (n=12. MSWD=1.4) Durango: Jan2019 - 31.75 ± 0.45 Ma (n=23. MSWD=2.7) Sep2019 – 33 ± 2 Ma (n=12. MSWD=1.9)

References :

Chew DM. Petrus JA. Kamber BS (2014) U–Pb LA–ICPMS dating using accessory mineral standards with variable common Pb. Chemical Geology 363:185-199 doi:https://doi.org/10.1016/j.chemgeo.2013.11.006

Cochrane R. Spikings RA. Chew D. Wotzlaw J-F. Chiaradia M. Tyrrell S. Schaltegger U. Van der Lelij R (2014) High temperature (>350°C) thermochronology and mechanisms of Pb loss in apatite. Geochimica et Cosmochimica Acta 127:39-56 doi:https://doi.org/10.1016/j.gca.2013.11.028

McDowell FW. McIntosh WC. Farley KA (2005) A precise 40Ar–39Ar reference age for the Durango apatite (U–Th)/He and fission-track dating standard. Chemical Geology 214(3):249-263 doi:https://doi.org/10.1016/j.chemgeo.2004.10.002

Paton C. Woodhead JD. Hellstrom JC. Hergt JM. Greig A. Maas R (2010) Improved laser ablation U-Pb zircon geochronology through robust downhole fractionation correction. Geochemistry. Geophysics. Geosystems 11(3) doi:10.1029/2009GC002618

Pochon A. Poujol M. Gloaguen E. Branquet Y. Cagnard F. Gumiaux C. Gapais D (2016) U-Pb LA-ICP-MS dating of apatite in mafic rocks: Evidence for a major magmatic event at the Devonian-Carboniferous boundary in the Armorican Massif (France). American Mineralogist 101(11):2430-2442 doi:http://dx.doi.org/10.2138/am-2016-5736

Schoene B. Bowring S (2006) U–Pb systematics of the McClure Mountain syenite: thermochronological constraints on the age of the 40Ar/39Ar standard MMhb. Contributions to Mineralogy and Petrology 151(5):615

Appendix 2 Operating conditions for the LA-ICP-MS equipment for U-Pb dating on zircon

Laboratory & Sample Preparation	
Laboratory name	GeOHeLiS Analytical Platform. OSUR. Univ Rennes 1. France
Sample type/mineral	Zircon
Sample preparation	Thin-section
Imaging	Jeol JSM 6360LV. Géoscience Environnement Toulouse. Univ Toulouse 3 Paul Sabatier. France ; TESCAN Vega 3. GeoRessources. Univ de Lorraine. Nancy. France
Laser ablation system	
Make. Model & type	ESI NWR193UC. Excimer
Ablation cell	ESI NWR TwoVol2
Laser wavelength	193 nm
Pulse width	< 5 ns
Fluence	8 J/cm^2

Repetition rate	3Hz
Spot size	30 µm
Sampling mode / pattern	Single spot
Carrier gas	100% He. Ar make-up gas and N2 (3 ml/mn) combined using in-house smoothing device
Background collection	20 seconds
Ablation duration	60 seconds
Wash-out delay	15 seconds
Cell carrier gas flow (He)	0.80 l/min
ICP-MS Instrument	
Make. Model & type	Agilent 7700x. Q-ICP-MS
Sample introduction	Via conventional tubing
RF power	1350W
Sampler. skimmer cones	Ni
Extraction lenses	X type
Make-up gas flow (Ar)	0.85 l/min
Detection system	Single collector secondary electron multiplier
Data acquisition protocol	Time-resolved analysis
Scanning mode	Peak hopping. one point per peak
Detector mode	Pulse counting. dead time correction applied. and analog mode when signal intensity > ~ 10^6 cps
Masses measured	^{204}(Hg + Pb). ^{206}Pb. ^{207}Pb. ^{208}Pb. ^{232}Th. ^{238}U
Integration time per peak	10-30 ms (^{207}Pb)
Sensitivity / Efficiency	23000 cps/ppm Pb (50µm. 10Hz)
Data Processing	
Gas blank	20 seconds on-peak
Calibration strategy	GJ1 zircon standard used as primary reference material. Plešovice used as secondary reference material (quality control)
Common-Pb correction. composition and uncertainty	No common-Pb correction.
Reference Material info	GJ1 (Jackson et al.. 2004). Plešovice (Slama et al.. 2008)
Data processing package	Iolite (Paton et al.. 2010)
Uncertainty level and propagation	Ages are quoted at 2 sigma absolute. propagation is by quadratic addition according to Horstwood et al. (2016). Reproducibility and age uncertainty of reference material are propagated.
Quality control / Validation	Plešovice: concordia age = 338.7± 3.3 Ma (n=6; MSWD=0.35)

References :

Horstwood MSA. Košler J. Gehrels G. Jackson SE. McLean NM. Paton C. Pearson NJ. Sircombe K. Sylvester P. Vermeesch P. Bowring JF. Condon DJ. Schoene B (2016) Community-Derived Standards for LA-ICP-MS U-(Th-)Pb Geochronology – Uncertainty Propagation. Age Interpretation and Data Reporting. Geostandards and Geoanalytical Research 40(3):311-332 doi:10.1111/j.1751-908X.2016.0379.x

Jackson SE. Pearson NJ. Griffin WL. Belousova EA (2004) The application of laser ablation-inductively coupled plasma-mass spectrometry to in situ U–Pb zircon geochronology. Chemical Geology 211:47-69

Paton C. Woodhead JD. Hellstrom JC. Hergt JM. Greig A. Maas R (2010) Improved laser ablation U-Pb zircon geochronology through robust downhole fractionation correction. Geochemistry. Geophysics. Geosystems 11(3) doi:10.1029/2009GC002618

Sláma J. Kosler J. Condon DJ. Crowley JL. Gerdes A. Hanchar JM. Horstwood MSA. Morris GA. Nasdala L. Norberg N. Schaltegger U. Schoene B. Tubrett MN. Whitehouse MJ (2008) Plesovice zircon -- A new natural reference material for U-Pb and Hf isotopic microanalysis. Chemical Geology 249(1-2):1-35